Applications of Macroporous Sponges Prepared Using Ice Templating

Thesis Submitted to AcSIR for the Award of
the Degree of
DOCTOR OF PHILOSOPHY
in
Chemical Sciences

By

Soumyajyoti Chatterjee
Reg. No.10CC11A26022

Under the Guidance of
Dr. Guruswamy Kumaraswamy

CSIR-National Chemical Laboratory,
Pune-411008, India, 2018

सीएसआयआर–राष्ट्रीय रासायनिक प्रयोगशाला
(वैज्ञानिक तथा औद्योगिक अनुसंधान परिषद)
डॉ. होमी भाभा मार्ग, पुणे – 411 008. भारत
CSIR-NATIONAL CHEMICAL LABORATORY
(Council of Scientific & Industrial Research)
Dr. Homi Bhabha Road, Pune - 411008. India

CERTIFICATE

This is to certify that the work incorporated in this Ph.D. thesis entitled, "**Applications of Macroporous Sponges Prepared Using Ice Templating**" submitted by **Soumyajyoti Chatterjee** to Academy of Scientific and Innovative Research (AcSIR) in fulfilment of the requirement for the award of the Degree of **Doctor of Philosophy,** embodies original research work carried out under my guidance. We further certify that this work has not been submitted to any other University or Institution in part or full for the award of any degree or diploma. Research materials obtained from other sources has been duly acknowledged in the thesis. Any text, illustration, table etc., used in the thesis from other sources, have been duly cited and acknowledged.

Soumyajyoti Chatterjee
(Student)

Dr. Guruswamy Kumaraswamy
(Research Supervisor)

Communications Channels
NCL Level DID : 2590
NCL Board No. : +91-20-25902000
Four PRI Lines : +91-20-25902000
FAX
Director's Office : +91-20-25902601
COA's Office : +91-20-25902660
SPO's Office : +91 20 25902664
WEBSITE
www.ncl-india.org

DECLARA TION BY RESEARCH SCHOLAR

I hereby declare that the thesis entitled **" Applications of Macroporous Sponges Prepared Using Ice Templating"** submitted by me for the Degree of Doctor of Philosophy to Academy of Scientific & Innovative Research (AcSIR) is the record of work carried out by me at Polymer Sciences & Engineering Division (PSE), CSIR-National Chemical Laboratory, Pune - 411008, India, under the supervision of Dr. Guruswamy Kumaraswamy (research supervisor). The work is original and has not formed the basis for the award of any degree, diploma, associateship, and fellowship titles in this or any other university or other institute of higher learning. I further declare that the material obtained from other resources has been duly acknowledged in the thesis.

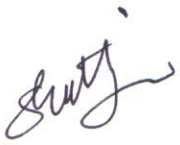

Soumyajyoti Chatterjee

Polymer Science & Engineering,

CSIR-National Chemical Laboratory

Dr. Horni Bhabha Road, Pashan

Pune-411008

Maharashtra, India

DEDICATED TO.....

MAA, BABA

Acknowledgement

In the journey of my thesis, several people have contributed significantly through their support, encouragement and criticism that enable me to reach at this level. The thesis is incomplete without acknowledging their efforts. First and foremost, I thank to my uncle who always stood and supported me to pursue my ambitions. I express my deepest appreciation to my research guide and mentor ***Dr. Guruswamy Kumaraswamy (CSIR-NCL****). He has been supportive and his constructive criticism has helped a lot during my thesis work. I am greatly inspired by his noble principles, ethics, and scientific temperament to perform high quality science. I enjoyed discussions (both scientific and general) with him, and his teaching during the course-work. He helped me to improve my writing & presentation skills, data analysis and scientific problem. He provided me all possible platforms to flourish scientifically and non-scientifically.*

I would like to thank my Doctoral Advisory Committee members ***Dr. Ashish V. Orpe (CSIR-NCL), Dr. Amol A. Kulkarni (CSIR-NCL),*** *and* ***Dr. T. Ajithkumar (CSIR-NCL)*** *for their critical comments and suggestions. I am also thankful to* ***Dr. Pankaj Doshi (my first advisor at NCL), Dr. Sayam Sen Gupta (CSIR-NCL, now at IISER, Kolkata), Dr. K. Krishnamoorthy (CSIR-NCL), Chayanika Das (CSIR-NCL), Dr. Kadhiravan Shanmuganathan, Dr. Simon Kuhn (KU Leuven), Aditi Poddar (KU Leuven)*** *whom I have collaborated for carrying out my thesis work.*

Some of my colleagues whom I would like to thanks for helping me during my research work are Shantigopal Mandal, Bhagyashri Gadgil, Sonal Channale, Amay Bhinde, Subhadarshinee Sahoo, Sandip Wadhi, Prashant Yadav, Bhawana Pandey. I would specially like to acknowledge ***Sudip Sasmal*** *for helping in multiple projects. I also take an opportunity to thank seniors E. Venugopal, Samruddh Kamble, Amruta Kulkarni, Prashant Patil, Sameer Huprikar, Mohan and Anal Kr. Ganai.*

My special thanks to friends Atanu, Atryee, Monaslisa, Sumanda, Manoj, Santanu, Manik, Bittu, Ujjal, Sutanu, Sujit, Bikas with whom I enjoyed a lot. Thanks are due to my beloved friend ***Malay Ghosh*** *and his family for their well-wishes and care.*

Finally, I am also grateful to my labmates Manoj Kumar Sharma (for being my best critics), Sudhakar, Karthika, Dr. Anees khan, Professor, Aniket, Bipul, Aakash, Saurab. I sincerely acknowledge the financial support from UGC (New Delhi), and CSIR-NCL (Pune).

Soumyajyoti Chatterjee

CONTENTS

List of Figures

List of Tables

Introduction

1.1 Introduction

Porous materials are classified into three categories based on pore size. Microporous materials are characterized by pore sizes less than 2 nm, while mesoporous materials have pores that range from 2 to 50 nm and macroporous materials have pores larger than 50 nm. Materials can also exhibit hierarchical porosity, with interconnected pores that span micro, meso and macropore size ranges. The properties of a porous material are a function of its pore geometry and pore size distribution and have implications for its use in various applications. For example, porous structures are often characterized by low densities and therefore have improved mechanical strength to weight ratio relative to bulk materials. Further, the pore structure can be controlled to manipulate the transport of heat, sound waves and light through porous materials. Therefore, Nature and humans have both sought to exploit materials characterized by porous architectures in a variety of applications. In this work, we largely focus on macroporous materials.

1.2 Applications of porous materials

The largest usage of macroporous materials can be found in thermal insulation.[1–7] Typically, macroporous materials with closed cell architecture have the lowest thermal conductivity. In contrast to closed cell foams, foams with completely or partially open cell architecture exhibit higher heat transfer. Thermal transport in porous insulation materials takes place via conduction through the solid walls and through the gas, through convection within the pores and radiative transfer between pore walls.[8] The inherently low thermal conductivity of porous materials, coupled with their ease of preparation has resulted in their wide spread use in products as simple as disposable Styrofoam coffee cups[9] and as technically challenging as the insulation of booster rockets for the space shuttle. Modern day buildings, refrigerated railway wagons and trucks and ships carrying liquefied natural gas rely on expandable polymer or composite foam insulation. One of the advantages of macroporous foams in low and high temperature applications lies in their low effective thermal mass.[8] Low thermal mass reduces the amount of coolant require to cool the insulation in ultra-low temperature applications. Similarly for high temperature, a large part of the heat dissipated in the furnace is used to raise the temperature of the system to its operating level. The thermal mass of a porous material is directly related to its density. Lower the thermal

mass, shorter is the time scale for temperature equilibration. Therefore an optimum material density is required for desired thermal transport characteristics.

Man made macroporous sponge like materials are largely used in packaging industries as impact resistance to offer omni-directional protection to fragile goods.[10–20] Sponges can undergo large compressive strains at almost constant stress. During compression, cell walls deform, buckle or fracture thereby allowing sponges to dissipate large amounts of energy without generating high stress. Mechanical properties of a sponge can be tuned over a wide range by adjusting its porosity and wall thickness. The low mass to volume ratio renders these materials extremely light weight, with advantages for handling. Additionally these must be cheap, since packaging is mostly discarded. Typically, polymeric sponges of polyethylene, polystyrene and polyurethane are widely used in packaging applications.

Closed cell, cellular sponges are extensively used as damage resistant supports for floating objects.[21–23] Sponges are highly damage tolerant and can retain their buoyancy even after extensive damaged. They are generally made from polyethylene, polystyrene or polyvinyl chloride and have a bulk density between 20 to 40 kg/m^3. These closed cell sponges have excellent water resistance and are unaffected by extended immersion in water. They are extensively used as the core of sandwich panels that form the deck and hull of modern day sailboats. These porous structures provide outstanding toughness as well as buoyancy.

Anisotropic, elastomeric macroporous materials partially or fully filled in wall or floor cavities, provide benefits by absorbing sound energy.[24–30] It is reported in the literature that the speed of sound propagation in a material decreases dramatically with increase in porosity.[31] The speed of the sound may decrease to as low as 80 m/s for porosity close to 90-95%. Cork, rubber or composites of rubber filled with cork are promising candidates for acoustic shielding. Sponges with a macroporous matrix comprising of soft silicone rubber (such as polydimethylsiloxane) are used to isolate buildings from shear waves because of their low shear modulus. Cork adds a high impedance to compressive waves due to its large plastic compressibility.

Oil spills and industrial effluents have resulted in severe water pollution and constitute a large threat to marine life, marine food cycles (and thereby to human beings).[32–34] Solvent

spillage from laboratories, car wash centres, etc. also pollute the local environment and degrade the surrounding air and soil. Therefore, there is a pressing need for immediate action to control effluent spillage. The most commonly used material at this time to tackle such problems is activated carbon.[32–34] Activated carbon is used as a versatile absorbent since it absorbs solvents independent of their polarity. Typically, activated carbon materials are porous and have very large specific surface area. Despite their large surface area, their absorption capacity is not very high. Moreover they are suitable only for one time usage and recovery of the absorbed solvent is cumbersome. Therefore, researchers have focused on developing macroporous materials as absorbents.[35–40] Macroporous materials are particularly interesting since they are lightweight, have high absorption and separation capacity, and are reusable after several cycles of performance.[41–50] A wide variety of macroporous sponges have been fabricated both at commercial scales and in the laboratory to address this problem. Precise control of wettability mostly renders these materials in the following five broad classes: (1) superhydrophobic and superoleophilic, (2) superhydrophilic and under water superolephobic, (3) superhydrophilic and superolephobic, (4) super omniphobic and (5) superomniphilic. Superomniphobic surfaces[51–54] are highly corrosion resistant. Currently, technologies used to render surfaces omniphobic necessarily rely on incorporation of fluorine moieties. In contrast, superomniphilic materials are capable of absorbing large volume of solvent independent of their polarity. These materials can mitigate general solvent spills. Macroporous sponges with tailored wettability are ideal candidates for oil/water separation. Typically, these materials are either highly oleophilic or highly hydrophilic to effect selective separation of oils from water surfaces. Kapok,[55–60] polymeric sponges,[61–63] ultralow weight carbon nanotube or graphene sponges,[64–67] hydrophobic aerogels[68–72] are examples oil removing macroporous materials.

Energy conversion and storage is essential for the development of humanity. Here too, materials that possess hierarchical porosity have an important role to play in a variety of applications.[73–80] Typically macro pores in hierarchically porous structures offer enhanced mass transport and act as ion-buffering reservoirs, while micro/meso pores provide large specific surface area for reaction and reduced diffusion paths. By incorporation of macroporosity in hierarchical materials, such as in TiO_2/ZrO_2 network structures; SnO_2/ TiO_2 thin films; WO_3/TiO_2 layers, macro channels[81–85] can be introduced that allow localization of light, allowing enhancement of light harvesting efficiency.[86,87] Therefore, these porous materials have applications in photocatalysis, photocatalytic H_2 production, photochemical

bioreactors and in dye sensitized solar cells and fuel cells. Additionally, these channels promote light scattering that leads to elongation of light path and thus can be a useful candidate as metamaterials[88–92] for electromagnetic radiation in a way that is not observed in bulk materials. In electrochemical and electrical storage devices, such as in battery and supercapacitors, macroporous materials can contribute to the improvement in energy storage performance and efficiency. Electrochemical performance of these devices is mainly influenced by the diffusion of ions between electrodes and at the electrode/electrolyte interface. Here, electrodes with interconnected porous networks can facilitate ion transport and large macro pores can act as buffer electrolyte reservoirs. Porous carbon composites, carbon nanotubes, graphene, several metal oxides including SnO_2, MnO_2, V_2O_5, Co_3O_4 and TiO_2 have been used as electrode materials. In several cases these devices fail due to their inability to accommodate large electrical stress generated during charge/discharge cycles. Thus, they tend to collapse or distort under compression. Recently researchers have addressed this using damage tolerant, high porosity sponge-like 3D electrodes based on polypyrrole mediated graphene.[93] In this material, the macroporous structure allows large compression without the graphene sheets getting stacked up and elastic nature of the wall ensures complete recovery.

Hierarchical porous materials that combine micro/mesopores with macropores have demonstrated advantages in catalysis as catalyst supports.[94–99] Techniques that allow control of pore characteristics at each length scale, and that afford chemical functionalization at each level of structural hierarchy can provide precise size selectivity for desired products for a catalytic reaction. Such materials have implications for chromatographic separations and mixing at low Reynolds number. In one example, researchers employed dynamic surfactant templating to prepare hybrid meso porous silica scaffolds with macropore size continuously varying from 0.5 μm to 50 μm by a spatial variation in cooling rate.[100] Cooling rate determines the domain size of surfactant mesophase which set the macropore length scale whereas mesoporosity of silica particles can be independently varied between 2 to 4 nm. In this process micro-meso pores serve as high specific surface area catalytic supports while the macroporous network enhances mass diffusion by minimizing flow resistance.

Porous materials have also been used in applications in the life sciences, including in tissue engineering and drug delivery.[101–110] For example, a porous material that is

encountered in Nature is bone. Thus, any defects in bone can be healed by using biocompatible macroporous scaffolding. In this context a large number of biodegradable naturally occurring polymers such as chitosan,[111] silk,[112] collagen[113] and gelatin[114] have been used as scaffolding material in tissue engineering and regenerative medicine. Porous materials have also been exploited for their storage capacity, that allows controlled release of a variety of drug molecules in both spatially and temporally controlled manner.[115–117]

Several foods are also macroporous. Porosity imparts a pleasing texture to foods. Bread, ice cream, chocolate bar, Jaffa cake, breakfast cereals are few examples of porous food.

1.3 Strategies for the preparation of synthetic porous materials

Over the last decade, significant number of strategies have been developed to prepare macroporous materials. In this section we will describe some of the key techniques developed to make such materials:

Porogen based methods:

1.3.1 Dynamic surfactant templating

Self-assembled molecular aggregates of surfactant molecules[118–121] can be employed as agents to build macroporous architecture. In one case, Sharma et al.[122] exploited hexagonal mesophase of a nonionic surfactant to organize variety of particles such as inorganic, organic, surface modified ceramics, and biological particles. They cross-linked these particle networks through suitable cross-linking chemistry that irreversibly froze the particle network structure. Removal of surfactant assembly by benign water washing afforded macroporous self-standing monoliths. Here, the size of the template, viz. surfactant mesophase domain, determined the pore size. They also demonstrated how pore size can be tuned from submicron to several tens of microns by simply controlling the cooling rate that controls nucleation and growth of mesophase domains.

1.3.2 Emulsion templating

Emulsion templating is one of the most commonly used routes for preparation of macroporous materials.[123–127] In several cases, water is used as one of the solvents. An emulsion can be prepared by dispersing water droplets in a continuous phase of oil or vice versa using a surfactant above its critical micellar concentration as stabilizer. The former case is called as a "water-in-oil (W/O) emulsion" while the latter is known as oil-in-water (O/W) emulsion. Careful adjustment of the water or oil phase droplets in the emulsions allows formation of porous structures with pore sizes that span from a few to hundreds of microns. Application of emulsions in the preparation of macroporous oxides has been reported by Pine et al.[123] In a typical procedure, sol-gel chemistry[128] is used to solidify precursors around the droplets. In subsequent steps solvent is evaporated to produce interconnected open cell porous materials.

1.3.3 Colloidal crystal templating followed by particulate leaching

Monodisperse polymer and ceramic particles can be assembled to form colloidal crystals, that can be used as templates to produce ordered macroporous monolithic materials.[129–135] Close packing of spherical template particles creates voids that can be filled up with ceramic or metal precursors. Selective removal of the colloidal template via solvent extraction or calcination can offer macroporous structures whose pore size depends upon the size of the colloids chosen to make the assembly. Polymer particles such as poly(methylmethacrylate) (PMMA) and polystyrene (PS) can be easily decomposed into volatile species while silica particles can be extracted by treatment with hydrofluoric acid or with strong bases. Colloidal polymer templates such as PMMA and PS can also be extracted from the structure by using suitable solvents such as tetrahydrofuran or toluene. In one example, Wang et al.[135] prepared a colloidal suspension with small (150 nm) and large (1000 nm) PS spheres and spread this on a glass slide. Evaporation of the solvent resulted in self-assembly of the colloidal spheres. Infiltration of the porous structure by tetraethylorthosilicate solution resulted in infilling the interstitial pores and the structure was subsequently solidified by drying. Finally the template was extracted in toluene, resulting in the formation of a hierarchical network structure of larger macropores with smaller pores in the walls. Therefore, colloidal crystal templates can be readily manipulated to allow precise control over pore geometry and pore size.

1.3.4 Gas bubbling

Gas bubbling provides an alternative route to the use of solid phase porogens to induce porosity.[136–143] Gas bubbling exploits the nucleation and growth of gas bubbles in precursor solutions to introduce pores. Gas bubbles can be generated by either mixing a blowing agent or by saturating a precursor solution with gas at high pressure. In the former case, blowing agents such as calcium carbonate or sodium bicarbonate are mixed with precursor and chemical decomposition of the agent generates gas. In the latter case, depressurization a saturated precursor solution leads to nucleation, growth and coalescence of gas bubbles. An advantage of gas bubbling is that this process does not require the use of organic solvents. However, pore formation and porosity are difficult to control since they strongly depend upon the rate of nucleation and gas diffusion. Dehghani et al.[142]fabricated macroporous scaffolds by supercritical carbon dioxide gas foaming. Several studies showed that a higher processing temperature (above the critical temperature of CO_2) at constant pressure during bubbling process may lead to larger pores and more open pores in the resultant architecture. In contrast, a higher soaking pressure at constant temperature may result in the generation of smaller pores when the system is depressurized. Thus, following the gas bubbling method, pore size and overall porosity of the porous microstructure can be tuned.

1.3.5 Breath figures

The breath figure method, also known as “moist-casting” has been traditionally used to prepare porous polymer films.[144–147] Cooling polymer solutions in controlled humidity condition can enable condensation, followed by growth and subsequent ordering of water droplets on the film surface. Complete evaporation of both the solvent and the water in the subsequent step results in 2D or 3D arrays of holes in the matrix depending upon the relative density of the solvent relative to water. When a denser solvent, such as carbon disulphide, is used samples with a single layer of pores can be generated. In contrast, when less dense solvents, such as toluene, are used, a hexagonal array of water droplets forms that can percolate through the matrix, resulting in a 3D ordered structure. This technique of pore formation is extremely attractive as it allows the formation of porous films using materials ranging from polymers, biocomposites, and metals with pore sizes that can be easily tuned from 2 to 20 μm by varying the preparation conditions.

1.3.6 Sacrificial templating:

Sacrificial template technique is a flexible route to obtain porous scaffolds with various chemical compositions. Mostly polymer based porous materials with defined pore size and porosity are selected as a sacrificial phase.[147–155] The advantages of this process are its simplicity and the ready availability of polymeric porous materials with various morphologies and sizes. In a typical method, various ceramics, metal precursors are deposited on the walls of a sacrificial phase through a sol-gel process or chemical vapour deposition technique to obtain a conformal coating. Subsequently, the sacrificial element is leached off by appropriate thermal or solvent treatment. Carefully controlled treatments enable the final material to retain the template structure and morphology.

1.3.7 Ice templating:

The application of freezing to colloidal dispersions to prepare porous materials is known as ice-templating or freeze-casting.[156–166] The process of ice-templating has been known for several decades but there is a revival of interest in this technique due to interesting developments over the past 20 years. In cryochemical synthesis routes, macroporous materials are shaped using ice-crystals as templates to generate pores. During the freezing process, ice crystals grow and colloids are spatially organized by the crystals. Ice is used as a generic term for solidification of a solvent. In this thesis, we work primarily with aqueous dispersions. Therefore, here we use the term ice exclusively to refer to crystals of water. The growth of ice crystals can be controlled to achieve desired porous architecture and mechanical properties in the final products. The freezing conditions influence the growth behaviour of ice crystals. To investigate the growth kinetics, morphologies and crystalline structure of crystals a number of imaging techniques such as X-ray imaging techniques, optical interferometry, electron and confocal microscopy are widely used. Imaging studies of ice crystals indicates that crystals can grow in the 1-100 μm/s range and size of the crystal can range typically from 1-100 μm. Therefore freezing routes can provide different levels of porosity. Additionally, porosity can be directional and well-organised, or it can be isotropic and random, depending on the freezing protocol.

While ice templating does not lend itself to structures with either ordered or monodisperse pores, unlike templating of sacrificial ordered templates such as colloidal crystals, it has other advantages. Ice templating is a versatile green technique that uses water

as a solvent and porogen. It can be applied to aqueous dispersions of a wide variety of colloids and the pore structures that form can be controlled to some extent by using additives such as zirconyl acetate and ice shaping proteins.

Additional levels of porosity in templated materials can be introduced by the incorporation of organic particles such as polystyrene[167], poly(methylmethacrylate)[168] or cotton fibers[169] into the initial ice-templated suspension. The dispersion is frozen and organic components are subsequently eliminated by thermal treatment or by solvent extraction from the templated matrix.

When pores result only from the use of ice as porogen, then the solute to solvent ratio has direct consequence on the total pore content. Therefore ice-templating is a versatile route for the preparation of materials with a wide range of porosity. The ice templating process can be used to prepare materials with porosity as low as 10 vol.% to as high as 99 vol.%. Aerogels are typical examples of high porosity materials. However below a critical particle concentration it is not possible to obtain macroporous material using ice templating. For particle concentrations above a critical concentration[170], the growing ice crystals cannot repel the particles and engulf them to produce materials with low porosity (below 40%) and no templating effect is obtained.

One of the most unique features of ice-templated materials is their attractive pore morphologies. These unique features of ice-templating are accessed when the particle concentration in the freezing suspensions lies within a critical range. Recently, researchers have employed unidirectional ice growth to control the pore geometry.[171–174] The macropores obtained represent the negative replica of the ice crystals. Thus nature of solvent also plays an important role in determining the pore morphology. Typically water is extensively used as solvent in ice-templating. When aqueous slurry is frozen unidirectionally, typically a lamellar morphology is obtained. The lamellar morphology is believed to result from anisotropic growth of the hexagonal form of ice. The size of the particles used to template the ice crystals also influences the pore morphology. Better replication of morphology is attained when the size of the suspended particle is much smaller than the template crystal size. For particle sizes larger than the crystals, the particles fail to pack properly and the particle is unable to replicate the contour of the crystals. In any case the rule is particle size should be at least an order of magnitude smaller than the half-periodicity of the lamellar pattern.

Pore size is another important parameter in macroporous materials. The desired pore size is critical for many structural applications like tissue engineering to mixing to absorption. Pore size can be easily tuned in the cryocasting process. Pore size is largely governed by

cooling rate.[175] It is reported in the literature that pore diameter is inversely related to the cooling rate. When additives such as salts (NaCl, $MgCl_2$ etc), antifreeze protein, various soluble solvents (alcohol, acetone), polymers are incorporated to the initial suspension prior to freezing, that leads to different morphology of the ice-crystals, and thus the pore size.[175] The effect of additives can be multidimensional. For instance, additives can change phase diagram of water and can modify the suspension properties, viz. freezing point, viscosity, charges in the system. Additives, for example, antifreeze protein[176] can even modify the growth kinetics of crystals by blocking selective crystallographic planes. Therefore, this rich tool box can be exploited to architect morphologies on demand.

Solidification of water is also accompanied by latent heat release. Therefore, heat flow between container and a suspension, and within a suspension has a strong impact on freezing phenomena. Design and property of the container determines the efficiency of the latent heat release and its conduction from the frozen crystals.[177] This heat flow directly impacts pore size and pore morphology. Imposition of a temperature gradient enables one-dimensional growth of ice crystals. Single and even dual temperature gradients have been applied during the freezing process to design ice templated macroporous materials with complex architectures. Thus controlling temperature gradients and controlling cooling rates can provide a spectrum of different architectures.

Ice templating is a versatile technique to prepare macroporous materials and almost any material can be ice-templated – ranging from polymer to ceramics to metals. This technique allows several levers to control the structure and properties of the final macroporous material. Discussion of all these parameters individually for different kinds of macroporous ice-templated materials is beyond the scope of this thesis. Control over porosity and pore morphology determines the mechanical response of ice-templated materials. Mechanical properties are strongly correlated to porosity and pore orientation. [178–183] Polymer scaffolds are inherently soft, and in order to improve their mechanical properties and structural integrity they are often blended with metals or ceramics. Biopolymer based composite scaffolds are particularly of interest for their special applications in biomedical implants. Aerogels that are fabricated via ice-templating can be used in a variety of applications spanning from sensors to electrodes for batteries and supercapacitors, fire resistance to oil absorption applications. In many such applications the mechanical responses of the ice templated materials is critical.

In ice –templated materials, ice crystals act as porogen that are typically removed via supercritical drying or sublimation to afford porous structure. Noticeably the structure

obtained after drying are lost once the sample is exposed to solvent. Typically to provide mechanical resiliency to the structure, ceramic, metals; and composite scaffolds are often subjected to thermal sintering. To overcome this multi-step processing, our group[184] has proposed a simpler strategy where we cross-link the polymeric component of ice-templated polymer-inorganic composites in the frozen state. Since the structure is chemically cross-linked, no additional post treatment is required. Instead, simple thawing of the frozen sample at room temperature affords a monolithic structure.

Macroporous ceramics fail abruptly when subjected to large strains.[185] To circumvent brittle failure of particle based monoliths, interparticle linkages are modified by organic capping molecules.[186,187] Our group has recently demonstrated a macroporous, centimetre-sized monolith that primarily comprises of rigid particles but that can recover elastically even after 90% compression. This mechanical response originates from a special microstructure where inorganic colloids are enmeshed in a cross-linked polymer matrix. This remarkable microstructure can be obtained using a variety of colloids, polymers and even with different cross-linking chemistry.

1.4 Statement of the problem

In this thesis work, we investigate applications of ice-templated sponges prepared using the ice templating method described by Rajamanickam et. al.[184] These sponges are macroporous and recover from compressive deformation despite their high inorganic content. The sponge walls have uncross-linked amine groups, that allow covalent customization of the sponge for specific end applications. We investigate the suitability of these sponges as fire retardant materials, that do not use environmentally hazardous additives. We prepare flexible supercapacitors by modifying the ice-templated sponges, that have potential applications as a power source in wearable devices. We also explore the use of these sponges as universal absorbents for solvent spillage. We investigate the kinetics of solvent uptake in these sponges, and rationalize our data in the context of the Ergun Forchheimer equation. Finally, we explore novel methods to control the wall structure in sponges, and to introduce voids in these to decrease the pressure drop required to pump fluids through the sponge.

1.5 Thesis objective

The aim of this work is to customize ice-templated macroporous sponges for a wide variety of applications. We demonstrate the versatility of ice-templated sponges by using them for applications as diverse as fire retardant materials, to flexible energy storage devices to omniphilic absorbents. We also shed light on the fluid transport through soft swellable sponges. Another objective of our work relates to developing modifications in the synthesis protocol to introduce holes in the pore walls, by the use of non-solvents.

1.6 Thesis outline

In this chapter (**Chapter 1),** we provide background to motivate our investigations on the applications of macroporous sponges prepared via ice-templating.

Chapter 2 examines the fire retardant behavior of ice-templated "memory foams". Usage of polyurethane (PU) foams is widespread - however, PU foams are flammable. To ensure compliance with fire safety standards, brominated and phosphate based additives are incorporated into the PU. These additives are highly toxic and hazardous to environment. Therefore, there is clearly a need for foams with excellent fire retardant properties achieved without compromising mechanical properties and that can be prepared using scalable techniques. We demonstrate hybrid inorganic/polymer foams that have superior fire retardant properties compared with commercial polyurethane foams containing FR additives. Our hybrid foams are elastic and recover completely from large compressive deformations. Interestingly, these foams exhibit tunable memory, viz. the time scale for complete recovery can be varied. Further, varying particle concentration in the hybrid foams allows us to tune their mechanical stiffness over a wide range. Flame applied to this foam does not spread and is self-extinguished. Peak release rates for these hybrid foams are about 75% lower than those for the FR-polyurethane foams (FR-PU).

In **Chapter 3** we report the preparation of compressible supercapacitors that retain their specific capacitance after large compression and that recover elastically after at least a hundred compression-expansion cycles. Compressible supercapacitors are prepared using a facile method that readily yields centimeter-scale macroporous objects. We ice template a solution of polyethyleneimine in green tea extract to prepare a macroporous crosslinked polymer gel (PG) whose walls are impregnated with green tea derived polyphenols. As the PG is insulating, we impart conductivity by deposition of gold on it. Gold deposition is done

in two steps: first, silver nanoparticles are formed on the PG walls by in-situ reduction by polyphenols and then gold films are deposited on these walls. Gold coated PGs (GPGs) were used as electrodes to deposit poly(3,4-ethylenedioxythiophene) as a pseudocapacitive material. The specific capacitance of PEDOT coated GPGs (PGPG) was found to be 253 F/g at 1 A/g. PGPG could be subjected to over a hundred compression/expansion cycles without any mechanical failure or loss of capacitative performance. The capacitance was found to be 243 F/g upon compressing the device to 25% of its original size (viz. compressive strain = 75%). Thus, even large compression does not affect the device performance. This device shows power and energy densities of 2715 W/kg and 22 Wh/kg, respectively, in the uncompressed state. The macroporous nature of PGPG makes it possible to fill the PGPG pores with gel electrolyte. We report that the gel electrolyte filled supercapacitor exhibited a specific capacitance of 200 F/g, that increased by 4 % upon 75 % compression.

Chapter 4 focuses on the development of omniphilic sponges that absorb a large quantity of solvent relative to their weight, independent of the solvent polarity. These materials represent useful universal absorbents for laboratory and industrial spills. The as-prepared monolith is hydrophilic and absorbs over 30-fold its weight in water. Modification of this sponge using valeroyl chloride renders it omniphilic, viz. a modified sponge absorbs over 10-fold its dry weight of either water or hexane. Modification using palmitoyl chloride that has a longer chain length results in the preparation of a hydrophobic sponge with a water contact angle around 130^{o}, that retains its oleophilicity underwater. The solvent absorbed in these sponges can be simply squeezed out and the sponges are stable to several hundred compression/expansion cycles. The large pore sizes of these sponges allow rapid absorption of even high viscosity solvents such as pump oil. Finally, we demonstrate that these sponges are also able to separate apolar oils that are emulsified in water using surfactants. These high porosity sponges with controllable solvophilicity represent inexpensive, high performance universal absorbents for general solvent spills.

In **chapter 5** we studied capillarity driven uptake of liquid in swellable, highly porous sponges which has significant industrial importance. The effect of systematic variation of sponge characteristics on solvent uptake had not been investigated in the literature. We report experiments that study capillary uptake in a variety of flexible, centimetre-sized macroporous cylindrical sponges. Ice-templating is used to prepare a series of model macroporous sponges where the porosity, modulus and composition are systematically varied. Two kinds of

sponges are investigated: (a) those comprised purely of cross-linked polymer and (b) those prepared as composites of inorganic particles and polymer. When one end of the sponge is plunged into a large reservoir, water rises through capillary action, against gravity. A transition from an inertial-capillary regime is observed where the liquid column height rises linearly with time, t, to a viscous-capillary regime where the liquid height rises with $t^{0.5}$. It is shown that these results can be rationalized using analyses developed for rigid sponges. Differential momentum balance equations for uptake in rigid capillaries are combined with the phenomenological Ergun-Forchheimer[188] relations to account for the effect of sponge microstructure. This approach works remarkably well in the viscous capillary regime and shows that capillary uptake is governed primarily by the total porosity and pore dimensions of the soft sponges.

In **Chapter 6** we investigate the role of non-solvent added during sponge synthesis on the microstructure of the ice-templated monolith. We demonstrate that this change in synthesis protocol introduces voids in the pore walls, thus resulting in a hierarchically porous structure. We observed a systematic increase in the number of voids with increasing non-solvent concentration. The modulus of these hierarchically porous sponges is, however, similar to that of sponges prepared without the addition of non-solvent. Sponges prepared with the highest non-solvent concentration exhibited a significantly decreased pressure drop at high flow rates.

References:

(1) Russell, H. W. Principles of Heat Flow in Porous Insulators. *J. Am. Ceram. Soc.* **1935**, *18*, 1–5.

(2) Ball, G. W.; Haggis, G. A.; Hurd, R.; Wood, J. F. A New Heat Resistant Rigid Foam. *J. Cell. Plast.* **1968**, *4*, 248–261.

(3) Schuetz, M. A.; Glicksman, L. R. A Basic Study of Heat Transfer Through Foam Insulation. *J. Cell. Plast.* **1984**, *20*, 114–121.

(4) Cunningham, A. A Structural Model of Heat Transfer through Rigid Polyurethane Foam. *International Symposium on Heat and Mass Transfer in Refrigeration and Cryogenics - Dubrovnik, Yugoslavia, 1 - 5 September, 1986*. Begel House Inc. **1987**.

(5) Glicksman, L. R.; Torpey, M. Factors Governing Heat Transfer through Closed Cell

Foam Insulation. *J. Therm. Insul.* **1989**, *12*, 257–269.

(6) Reim, M.; Körner, W.; Manara, J.; Korder, S.; Arduini-Schuster, M.; Ebert, H.-P.; Fricke, J. Silica Aerogel Granulate Material for Thermal Insulation and Daylighting. *Sol. Energy* **2005**, *79*, 131–139.

(7) Baetens, R.; Jelle, B. P.; Gustavsen, A. Aerogel Insulation for Building Applications: A State-of-the-Art Review. *Energy Build.* **2011**, *43*, 761–769.

(8) Gibson, L. J.; Ashby, M. F. *Cellular Solids : Structure and Properties*; Cambridge University Press, **1999.**

(9) Abd-El-Khalick, F.; Lederman, N. G. Improving Science Teachers' Conceptions of Nature of Science: A Critical Review of the Literature. *Int. J. Sci. Educ.* **2000**, *22*, 665–701.

(10) Rusch, K. C. Load–compression Behavior of Flexible Foams. *J. Appl. Polym. Sci.* **1969**, *13*, 2297–2311.

(11) Rusch, K. C. Load-Compression Behavior of Brittle Foams. *J. Appl. Polym. Sci.* **1970**, *14*, 1263–1276.

(12) Meinecke, E. A.; Schwaber, D. M. Energy Absorption in Polymeric Foams. I. Prediction of Impact Behavior from Instron Data for Foams with Rate-Independent Modulus. *J. Appl. Polym. Sci.* **1970**, *14*, 2239–2248.

(13) Lee, W. M.; Williams, B. M. Cushioning and Load Distribution Performance of Plastic Foams. *J. Cell. Plast.* **1971**, *7*, 72–77.

(14) Rusch, K. C. Impact Energy Absorption by Foamed Polymers. *J. Cell. Plast.* **1971**, *7*, 78–83.

(15) Hilyard, N. C.; Djiauw, L. K. Observations on the Impact Behaviour of Polyurethane Foams; I. The Polymer Matrix. *J. Cell. Plast.* **1971**, *7*, 33–42.

(16) Miltz, J.; Gruenbaum, G. Evaluation of Cushioning Properties of Plastic Foams from Compressive Measurements. *Polym. Eng. Sci.* **1981**, *21*, 1010–1014.

(17) Gibson, L. J.; Ashby, M. F. The Mechanics of Three-Dimensional Cellular Materials. *Proc. R. Soc. A Math. Phys. Eng. Sci.* **1982**, *382*, 43–59.

(18) Maiti, S. K.; Gibson, L. J.; Ashby, M. F. Deformation and Energy Absorption Diagrams for Cellular Solids. *Acta Metall.* **1984**, *32*, 1963–1975.

(19) Zhu, H. X.; Mills, N. J.; Knott, J. F. Analysis of the High Strain Compression of Open-Cell Foams. *J. Mech. Phys. Solids* **1997**, *45*, 1875–1904.

(20) Christensen, R. M. Mechanics of Cellular and Other Low-Density Materials. *Int. J. Solids Struct.* **2000**, *37*, 93–104.

(21) Lowther Y. L. Auxiliary Flotation Gear for Fishing Boats. **1979**.

(22) Polidan, G. D. Pontoon Boat. **1999**.

(23) Wills, B.R. Slamming-Resistant Sonar Dome Canoe. **1980**.

(24) Howell, B.; Prendergast, P.; Hansen, L. Examination of Acoustic Behavior of Negative Poisson's Ratio Materials. *Appl. Acoust.* **1994**, *43*, 141–148.

(25) Han, F.; Seiffert, G.; Zhao, Y.; Gibbs, B. Acoustic Absorption Behaviour of an Open-Celled Aluminium Foam. *J. Phys. D. Appl. Phys.* **2003**, *36*, 294–302.

(26) Scarpa, F.; Bullough, W. A.; Lumley, P. Trends in Acoustic Properties of Iron Particle Seeded Auxetic Polyurethane Foam. *Proc. Inst. Mech. Eng. Part C J. Mech. Eng. Sci.* **2004**, *218*, 241–244.

(27) Etchessahar, M.; Sahraoui, S.; Benyahia, L.; Tassin, J. F. Frequency Dependence of Elastic Properties of Acoustic Foams. *J. Acoust. Soc. Am.* **2005**, *117*, 1114–1121.

(28) Verdejo, R.; Stämpfli, R.; Alvarez-Lainez, M.; Mourad, S.; Rodriguez-Perez, M. A.; Brühwiler, P. A.; Shaffer, M. Enhanced Acoustic Damping in Flexible Polyurethane Foams Filled with Carbon Nanotubes. *Compos. Sci. Technol.* **2009**, *69*, 1564–1569.

(29) Mosanenzadeh, S. G.; Naguib, H. E.; Park, C. B.; Atalla, N. Development, Characterization, and Modeling of Environmentally Friendly Open-Cell Acoustic Foams. *Polym. Eng. Sci.* **2013**, *53*, 1979–1989.

(30) Jahani, D.; Ameli, A.; Jung, P. U.; Barzegari, M. R.; Park, C. B.; Naguib, H. Open-Cell Cavity-Integrated Injection-Molded Acoustic Polypropylene Foams. *Mater. Des.* **2014**, *53*, 20–28.

(31) Zimny, K.; Merlin, A.; Ba, A.; Aristégui, C.; Brunet, T.; Mondain-Monval, O. Soft Porous Silicone Rubbers as Key Elements for the Realization of Acoustic Metamaterials. *Langmuir* **2015**, *31*, 3215–3221.

(32) Reddy, C. M.; Arey, J. S.; Seewald, J. S.; Sylva, S. P.; Lemkau, K. L.; Nelson, R. K.; Carmichael, C. A.; McIntyre, C. P.; Fenwick, J.; Ventura, G. T.; Van Mooy, B. A. S.; Camilli, R. Composition and Fate of Gas and Oil Released to the Water Column during the Deepwater Horizon Oil Spill. *Proc. Natl. Acad. Sci. U. S. A.* **2012**, *109*, 20229–20234.

(33) Botsford, L. W.; Tinker, S. D.; Williams, J. W.; Doak, D.; Bodkin, J. L.; Ballachey, B. E.; Irons, D. B. The Management of Fisheries and Marine Ecosystems. *Science (80-.).* **1997**, *277*, 509–515.

(34) Atlas, R. M. Petroleum Biodegradation and Oil Spill Bioremediation. *Mar. Pollut. Bull.* **1995**, *31*, 178–182.

(35) Choi, H. M.; Cloud, R. M. Natural Sorbents in Oil Spill Cleanup. *Environ. Sci. Technol.* **1992**, *26*, 772–776.

(36) Adebajo, M. O.; Frost, R. L.; Kloprogge, J. T.; Carmody, O.; Kokot, S. Porous Materials for Oil Spill Cleanup: A Review of Synthesis and Absorbing Properties. *J. Porous Mater.* **2003**, *10*, 159–170.

(37) Bayat, A.; Aghamiri, S. F.; Moheb, A.; Vakili-Nezhaad, G. R. Oil Spill Cleanup from Sea Water by Sorbent Materials. *Chem. Eng. Technol.* **2005**, *28*, 1525–1528.

(38) Lim, T.-T.; Huang, X. Evaluation of Kapok (Ceiba Pentandra (L.) Gaertn.) as a Natural Hollow Hydrophobic–oleophilic Fibrous Sorbent for Oil Spill Cleanup. *Chemosphere* **2007**, *66*, 955–963.

(39) Zhu, H.; Qiu, S.; Jiang, W.; Wu, D.; Zhang, C. Evaluation of Electrospun Polyvinyl Chloride/Polystyrene Fibers As Sorbent Materials for Oil Spill Cleanup. *Environ. Sci. Technol.* **2011**, *45*, 4527–4531.

(40) Yang, C.; Kaipa, U.; Mather, Q. Z.; Wang, X.; Nesterov, V.; Venero, A. F.; Omary, M. A. Fluorous Metal–Organic Frameworks with Superior Adsorption and Hydrophobic Properties toward Oil Spill Cleanup and Hydrocarbon Storage. *J. Am. Chem. Soc.* **2011**, *133*, 18094–18097.

(41) Gui, X.; Wei, J.; Wang, K.; Cao, A.; Zhu, H.; Jia, Y.; Shu, Q.; Wu, D. Carbon Nanotube Sponges. *Adv. Mater.* **2010**, *22*, 617–621.

(42) Choi, S.-J.; Kwon, T.-H.; Im, H.; Moon, D.-I.; Baek, D. J.; Seol, M.-L.; Duarte, J. P.; Choi, Y.-K. A Polydimethylsiloxane (PDMS) Sponge for the Selective Absorption of Oil from Water. *ACS Appl. Mater. Interfaces* **2011**, *3*, 4552–4556.

(43) Zhu, Q.; Pan, Q.; Liu, F. Facile Removal and Collection of Oils from Water Surfaces through Superhydrophobic and Superoleophilic Sponges. *J. Phys. Chem. C* **2011**, *115*, 17464–17470.

(44) Nguyen, D. D.; Tai, N.-H.; Lee, S.-B.; Kuo, W.-S. Superhydrophobic and Superoleophilic Properties of Graphene-Based Sponges Fabricated Using a Facile Dip Coating Method. *Energy Environ. Sci.* **2012**, *5*, 7908.

(45) Dong, X.; Chen, J.; Ma, Y.; Wang, J.; Chan-Park, M. B.; Liu, X.; Wang, L.; Huang, W.; Chen, P. Superhydrophobic and Superoleophilic Hybrid Foam of Graphene and Carbon Nanotube for Selective Removal of Oils or Organic Solvents from the Surface of Water. *Chem. Commun.* **2012**, *48*, 10660.

(46) He, Y.; Liu, Y.; Wu, T.; Ma, J.; Wang, X.; Gong, Q.; Kong, W.; Xing, F.; Liu, Y.; Gao, J. An Environmentally Friendly Method for the Fabrication of Reduced Graphene

Oxide Foam with a Super Oil Absorption Capacity. *J. Hazard. Mater.* **2013**, *260*, 796–805.

(47) Bi, H.; Yin, Z.; Cao, X.; Xie, X.; Tan, C.; Huang, X.; Chen, B.; Chen, F.; Yang, Q.; Bu, X.; Lu, X.; Sun, L.; Zhang, H. Carbon Fiber Aerogel Made from Raw Cotton: A Novel, Efficient and Recyclable Sorbent for Oils and Organic Solvents. *Adv. Mater.* **2013**, *25*, 5916–5921.

(48) Nardecchia, S.; Carriazo, D.; Ferrer, M. L.; Gutiérrez, M. C.; del Monte, F. Three Dimensional Macroporous Architectures and Aerogels Built of Carbon Nanotubes And/or Graphene: Synthesis and Applications. *Chem. Soc. Rev.* **2013**, *42*, 794–830.

(49) Wang, C.-F.; Lin, S.-J. Robust Superhydrophobic/Superoleophilic Sponge for Effective Continuous Absorption and Expulsion of Oil Pollutants from Water. *ACS Appl. Mater. Interfaces* **2013**, *5*, 8861–8864.

(50) Hayase, G.; Kanamori, K.; Fukuchi, M.; Kaji, H.; Nakanishi, K. Facile Synthesis of Marshmallow-like Macroporous Gels Usable under Harsh Conditions for the Separation of Oil and Water. *Angew. Chemie Int. Ed.* **2013**, *52*, 1986–1989.

(51) Tuteja, A.; Choi, W.; Ma, M.; Mabry, J. M.; Mazzella, S. A.; Rutledge, G. C.; McKinley, G. H.; Cohen, R. E. Designing Superoleophobic Surfaces. *Science* **2007**, *318*, 1618–1622.

(52) Tuteja, A.; Choi, W.; Mabry, J. M.; McKinley, G. H.; Cohen, R. E. Robust Omniphobic Surfaces. *Proc. Natl. Acad. Sci. U. S. A.* **2008**, *105*, 18200–18205.

(53) Campos, R.; Guenthner, A. J.; Meuler, A. J.; Tuteja, A.; Cohen, R. E.; McKinley, G. H.; Haddad, T. S.; Mabry, J. M. Superoleophobic Surfaces through Control of Sprayed-on Stochastic Topography. *Langmuir* **2012**, *28*, 9834–9841.

(54) Pan, S.; Kota, A. K.; Mabry, J. M.; Tuteja, A. Superomniphobic Surfaces for Effective Chemical Shielding. *J. Am. Chem. Soc.* **2013**, *135*, 578–581.

(55) Khan, E.; Virojnagud, W.; Ratpukdi, T. Use of Biomass Sorbents for Oil Removal from Gas Station Runoff. *Chemosphere* **2004**, *57*, 681–689.

(56) Huang, X.; Lim, T.-T. Performance and Mechanism of a Hydrophobic–oleophilic Kapok Filter for Oil/water Separation. *Desalination* **2006**, *190*, 295–307.

(57) Ali, N.; El-Harbawi, M.; Jabal, A. A.; Yin, C.-Y. Characteristics and Oil Sorption Effectiveness of Kapok Fibre, Sugarcane Bagasse and Rice Husks: Oil Removal Suitability Matrix. *Environ. Technol.* **2012**, *33*, 481–486.

(58) Wang, J.; Zheng, Y.; Wang, A. Superhydrophobic Kapok Fiber Oil-Absorbent: Preparation and High Oil Absorbency. *Chem. Eng. J.* **2012**, *213*, 1–7.

(59) Wang, J.; Zheng, Y.; Wang, A. Effect of Kapok Fiber Treated with Various Solvents on Oil Absorbency. *Ind. Crops Prod.* **2012**, *40*, 178–184.

(60) Wang, J.; Zheng, Y.; Wang, A. Coated Kapok Fiber for Removal of Spilled Oil. *Mar. Pollut. Bull.* **2013**, *69*, 91–96.

(61) Tu, C.-W.; Tsai, C.-H.; Wang, C.-F.; Kuo, S.-W.; Chang, F.-C. Fabrication of Superhydrophobic and Superoleophilic Polystyrene Surfaces by a Facile One-Step Method. *Macromol. Rapid Commun.* **2007**, *28*, 2262–2266.

(62) Li, A.; Sun, H.-X.; Tan, D.-Z.; Fan, W.-J.; Wen, S.-H.; Qing, X.-J.; Li, G.-X.; Li, S.-Y.; Deng, W.-Q. Superhydrophobic Conjugated Microporous Polymers for Separation and Adsorption. *Energy Environ. Sci.* **2011**, *4*, 2062.

(63) Pan, Y.; Shi, K.; Peng, C.; Wang, W.; Liu, Z.; Ji, X. Evaluation of Hydrophobic Polyvinyl-Alcohol Formaldehyde Sponges As Absorbents for Oil Spill. *ACS Appl. Mater. Interfaces* **2014**, *6*, 8651–8659.

(64) Zou, J.; Liu, J.; Karakoti, A. S.; Kumar, A.; Joung, D.; Li, Q.; Khondaker, S. I.; Seal, S.; Zhai, L. Ultralight Multiwalled Carbon Nanotube Aerogel. *ACS Nano* **2010**, *4*, 7293–7302.

(65) Gui, X.; Li, H.; Wang, K.; Wei, J.; Jia, Y.; Li, Z.; Fan, L.; Cao, A.; Zhu, H.; Wu, D. Recyclable Carbon Nanotube Sponges for Oil Absorption. *Acta Mater.* **2011**, *59* (12), 4798–4804.

(66) Sun, H.; Xu, Z.; Gao, C. Multifunctional, Ultra-Flyweight, Synergistically Assembled Carbon Aerogels. *Adv. Mater.* **2013**, *25*, 2554–2560.

(67) Wu, Z.-Y.; Li, C.; Liang, H.-W.; Zhang, Y.-N.; Wang, X.; Chen, J.-F.; Yu, S.-H. Carbon Nanofiber Aerogels for Emergent Cleanup of Oil Spillage and Chemical Leakage under Harsh Conditions. *Sci. Rep.* **2014**, *4*, 4079.

(68) Reynolds, J. G.; Coronado, P. R.; Hrubesh, L. W. Hydrophobic Aerogels for Oil-Spill Clean up – Synthesis and Characterization. *J. Non. Cryst. Solids* **2001**, *292*, 127–137.

(69) John G. Reynolds, Paul R. Coronado, P. R. C. L. W. H. Hydrophobic Aerogels for Oil-Spill Cleanup? Intrinsic Absorbing Properties. *Energy Sources* **2001**, *23*, 831–843.

(70) Korhonen, J. T.; Kettunen, M.; Ras, R. H. A.; Ikkala, O. Hydrophobic Nanocellulose Aerogels as Floating, Sustainable, Reusable, and Recyclable Oil Absorbents. *ACS Appl. Mater. Interfaces* **2011**, *3*, 1813–1816.

(71) Nguyen, S. T.; Feng, J.; Le, N. T.; Le, A. T. T.; Hoang, N.; Tan, V. B. C.; Duong, H. M. Cellulose Aerogel from Paper Waste for Crude Oil Spill Cleaning. *Ind. Eng. Chem. Res.* **2013**, *52*, 18386–18391.

(72) Ge, J.; Ye, Y.-D.; Yao, H.-B.; Zhu, X.; Wang, X.; Wu, L.; Wang, J.-L.; Ding, H.; Yong, N.; He, L.-H.; Yu, S.-H. Pumping through Porous Hydrophobic/Oleophilic Materials: An Alternative Technology for Oil Spill Remediation. *Angew. Chemie* **2014**, *126*, 3686–3690.

(73) Chai, G. S.; Shin, I. S.; Yu, J.-S. Synthesis of Ordered, Uniform, Macroporous Carbons with Mesoporous Walls Templated by Aggregates of Polystyrene Spheres and Silica Particles for Use as Catalyst Supports in Direct Methanol Fuel Cells. *Adv. Mater.* **2004**, *16*, 2057–2061.

(74) Woo, S.-W.; Dokko, K.; Nakano, H.; Kanamura, K. Preparation of Three Dimensionally Ordered Macroporous Carbon with Mesoporous Walls for Electric Double-Layer Capacitors. *J. Mater. Chem.* **2008**, *18*, 1674.

(75) Wang, Z.; Fierke, M. A.; Stein, A. Porous Carbon/Tin (IV) Oxide Monoliths as Anodes for Lithium-Ion Batteries. *J. Electrochem. Soc.* **2008**, *155*, A658.

(76) Wang, Z.; Li, F.; Ergang, N. S.; Stein, A. Synthesis of Monolithic 3D Ordered Macroporous Carbon/nano-Silicon Composites by Diiodosilane Decomposition. *Carbon N. Y.* **2008**, *46*, 1702–1710.

(77) Fang, B.; Kim, J. H.; Kim, M.-S.; Bonakdarpour, A.; Lam, A.; Wilkinson, D. P.; Yu, J.-S. Fabrication of Hollow Core Carbon Spheres with Hierarchical Nanoarchitecture for Ultrahigh Electrical Charge Storage. *J. Mater. Chem.* **2012**, *22*, 19031.

(78) Yan, Y.; Yin, Y.-X.; Guo, Y.-G.; Wan, L.-J. A Sandwich-Like Hierarchically Porous Carbon/Graphene Composite as a High-Performance Anode Material for Sodium-Ion Batteries. *Adv. Energy Mater.* **2014**, *4*, 1301584.

(79) Zhang, B.; Xiao, M.; Wang, S.; Han, D.; Song, S.; Chen, G.; Meng, Y. Novel Hierarchically Porous Carbon Materials Obtained from Natural Biopolymer as Host Matrixes for Lithium–Sulfur Battery Applications. *ACS Appl. Mater. Interfaces* **2014**, *6*, 13174–13182.

(80) Zhao, B.; Wang, Q.; Zhang, S.; Deng, C. Self-Assembled Wafer-like Porous $NaTi_2(PO_4)_3$ Decorated with Hierarchical Carbon as a High-Rate Anode for Aqueous Rechargeable Sodium Batteries. *J. Mater. Chem. A* **2015**, *3*, 12089–12096.

(81) Li, Y.; Fu, Z.-Y.; Su, B.-L. Hierarchically Structured Porous Materials for Energy Conversion and Storage. *Adv. Funct. Mater.* **2012**, *22*, 4634–4667.

(82) Li, X.-Y.; Chen, L.-H.; Li, Y.; Rooke, J. C.; Wang, C.; Lu, Y.; Krief, A.; Yang, X.-Y.; Su, B.-L. Self-Generated Hierarchically Porous Titania with High Surface Area: Photocatalytic Activity Enhancement by Macrochannel Structure. *J. Colloid Interface*

Sci. **2012**, *368*, 128–138.

(83) Chen, L.-H.; Li, X.-Y.; Deng, Z.; Hu, Z.-Y.; Rooke, J. C.; Krief, A.; Yang, X.-Y.; Su, B.-L. Hydrothermal and Surfactant Treatment to Enhance the Photocatalytic Activity of Hierarchically Meso–macroporous Titanias. *Catal. Today* **2013**, *212*, 89–97.

(84) Chen, X.; Wang, C.; Baker, E.; Sun, C. Numerical and Experimental Investigation of Light Trapping Effect of Nanostructured Diatom Frustules. *Sci. Rep.* **2015**, *5*, 11977.

(85) Yan, R.; Chen, M.; Zhou, H.; Liu, T.; Tang, X.; Zhang, K.; Zhu, H.; Ye, J.; Zhang, D.; Fan, T. Bio-Inspired Plasmonic Nanoarchitectured Hybrid System Towards Enhanced Far Red-to-Near Infrared Solar Photocatalysis. *Sci. Rep.* **2016**, *6*, 20001.

(86) Fukuzumi, S. Bioinspired Energy Conversion Systems for Hydrogen Production and Storage. *Eur. J. Inorg. Chem.* **2008**, *2008*, 1351–1362.

(87) Zhou, H.; Li, X.; Fan, T.; Osterloh, F. E.; Ding, J.; Sabio, E. M.; Zhang, D.; Guo, Q. Artificial Inorganic Leafs for Efficient Photochemical Hydrogen Production Inspired by Natural Photosynthesis. *Adv. Mater.* **2010**, *22*, 951–956.

(88) Smith, D. R.; Pendry, J. B.; Wiltshire, M. C. K. Metamaterials and Negative Refractive Index. *Science* **2004**, *305*, 788–792.

(89) Sihvola, A. Metamaterials in Electromagnetics. *Metamaterials* **2007**, *1*, 2–11.

(90) Biener, J.; Nyce, G. W.; Hodge, A. M.; Biener, M. M.; Hamza, A. V.; Maier, S. A. Nanoporous Plasmonic Metamaterials. *Adv. Mater.* **2008**, *20*, 1211–1217.

(91) Yao, J.; Liu, Z.; Liu, Y.; Wang, Y.; Sun, C.; Bartal, G.; Stacy, A. M.; Zhang, X. Optical Negative Refraction in Bulk Metamaterials of Nanowires. *Science* **2008**, *321*, 930.

(92) Zhang, X.; Zheng, Y.; Liu, X.; Lu, W.; Dai, J.; Lei, D. Y.; MacFarlane, D. R. Hierarchical Porous Plasmonic Metamaterials for Reproducible Ultrasensitive Surface-Enhanced Raman Spectroscopy. *Adv. Mater.* **2015**, *27*, 1090–1096.

(93) Zhao, Y.; Liu, J.; Hu, Y.; Cheng, H.; Hu, C.; Jiang, C.; Jiang, L.; Cao, A.; Qu, L. Highly Compression-Tolerant Supercapacitor Based on Polypyrrole-Mediated Graphene Foam Electrodes. *Adv. Mater.* **2013**, *25*, 591–595.

(94) Manton, M. R. S.; Davidtz, J. C. Controlled Pore Sizes and Active Site Spacings Determining Selectivity in Amorphous Silica-Alumina Catalysts. *J. Catal.* **1979**, *60*, 156–166.

(95) Corma, A. From Microporous to Mesoporous Molecular Sieve Materials and Their Use in Catalysis. *Chem. Rev.* **1997**, *97*, 2373–2420.

(96) Jones, C. W.; Tsuji, K.; Davis, M. E. Organic-Functionalized Molecular Sieves as

Shape-Selective Catalysts. *Nature* **1998**, *393*, 52–54.

(97) Rooke, J. C.; Barakat, T.; Finol, M. F.; Billemont, P.; De Weireld, G.; Li, Y.; Cousin, R.; Giraudon, J.-M.; Siffert, S.; Lamonier, J.-F.; Su, B. L. Influence of Hierarchically Porous Niobium Doped TiO2 Supports in the Total Catalytic Oxidation of Model VOCs over Noble Metal Nanoparticles. *Appl. Catal. B Environ.* **2013**, *142–143*, 149–160.

(98) Davis, S. C.; Sheppard, V. C.; Begum, G.; Cai, Y.; Fang, Y.; Berrigan, J. D.; Kröger, N.; Sandhage, K. H. Rapid Flow-Through Biocatalysis with High Surface Area, Enzyme-Loaded Carbon and Gold-Bearing Diatom Frustule Replicas. *Adv. Funct. Mater.* **2013**, *23*, 4611–4620.

(99) Franco Finol, M.; Rooke, J.; Siffert, S.; Cousin, R.; Carniti, P.; Gervasini, A.; Giraudon, J.-M.; Su, B.-L.; Lamonier, J.-F. Hierarchically Porous Nb–TiO_2 Nanomaterials for the Catalytic Transformation of 2-Propanol and N-Butanol. *New J. Chem.* **2014**, *38*, 1988–1995.

(100) Ganai, A. K.; Kumari, S.; Sharma, K. P.; Panda, C.; Kumaraswamy, G.; Gupta, S. Sen. Synthesis of Functional Hybrid Silica Scaffolds with Controllable Hierarchical Porosity by Dynamic Templating. *Chem. Commun.* **2012**, *48*, 5292.

(101) Madihally, S. V.; Matthew, H. W. T. Porous Chitosan Scaffolds for Tissue Engineering. *Biomaterials* **1999**, *20*, 1133–1142.

(102) Hutmacher, D. W. Scaffolds in Tissue Engineering Bone and Cartilage. *Biomaterials* **2000**, *21*, 2529–2543.

(103) Freyman, T. M.; Yannas, I. V.; Gibson, L. J. Cellular Materials as Porous Scaffolds for Tissue Engineering. *Prog. Mater. Sci.* **2001**, *46*, 273–282.

(104) Yoshimoto, H.; Shin, Y. M.; Terai, H.; Vacanti, J. P. A Biodegradable Nanofiber Scaffold by Electrospinning and Its Potential for Bone Tissue Engineering. *Biomaterials* **2003**, *24*, 2077–2082.

(105) Wei, G.; Ma, P. X. Structure and Properties of Nano-Hydroxyapatite/polymer Composite Scaffolds for Bone Tissue Engineering. *Biomaterials* **2004**, *25*, 4749–4757.

(106) Hollister, S. J. Porous Scaffold Design for Tissue Engineering. *Nat. Mater.* **2005**, *4*, 518–524.

(107) Williams, J. M.; Adewunmi, A.; Schek, R. M.; Flanagan, C. L.; Krebsbach, P. H.; Feinberg, S. E.; Hollister, S. J.; Das, S. Bone Tissue Engineering Using Polycaprolactone Scaffolds Fabricated via Selective Laser Sintering. *Biomaterials* **2005**, *26*, 4817–4827.

(108) Rezwan, K.; Chen, Q. Z.; Blaker, J. J.; Boccaccini, A. R. Biodegradable and Bioactive Porous Polymer/inorganic Composite Scaffolds for Bone Tissue Engineering. *Biomaterials* **2006**, *27*, 3413–3431.

(109) Gaharwar, A. K.; Dammu, S. A.; Canter, J. M.; Wu, C.-J.; Schmidt, G. Highly Extensible, Tough, and Elastomeric Nanocomposite Hydrogels from Poly(ethylene Glycol) and Hydroxyapatite Nanoparticles. *Biomacromolecules* **2011**, *12*, 1641–1650.

(110) Gentile, P.; Chiono, V.; Tonda-Turo, C.; Mattu, C.; Baino, F.; Vitale-Brovarone, C.; Ciardelli, G. Bioresorbable Glass Effect on the Physico-Chemical Properties of Bilayered Scaffolds for Osteochondral Regeneration. *Mater. Lett.* **2012**, *89*, 74–76.

(111) Levengood, S. K. L.; Zhang, M. Chitosan-Based Scaffolds for Bone Tissue Engineering. *J. Mater. Chem. B* **2014**, *2*, 3161.

(112) Hofmann, S.; Hilbe, M.; Fajardo, R. J.; Hagenmüller, H.; Nuss, K.; Arras, M.; Müller, R.; von Rechenberg, B.; Kaplan, D. L.; Merkle, H. P. Remodeling of Tissue-Engineered Bone Structures in Vivo. *Eur. J. Pharm. Biopharm.* **2013**, *85*, 119–129.

(113) Glowacki, J.; Mizuno, S. Collagen Scaffolds for Tissue Engineering. *Biopolymers* **2008**, *89*, 338–344.

(114) Kang, H.-W.; Tabata, Y.; Ikada, Y. Fabrication of Porous Gelatin Scaffolds for Tissue Engineering. *Biomaterials* **1999**, *20*, 1339–1344.

(115) Kim, H.-W.; Knowles, J. C.; Kim, H.-E. Hydroxyapatite/poly(ε-Caprolactone) Composite Coatings on Hydroxyapatite Porous Bone Scaffold for Drug Delivery. *Biomaterials* **2004**, *25*, 1279–1287.

(116) Zhang, L. F.; Sun, R.; Xu, L.; Du, J.; Xiong, Z. C.; Chen, H. C.; Xiong, C. D. Hydrophilic Poly (Ethylene Glycol) Coating on PDLLA/BCP Bone Scaffold for Drug Delivery and Cell Culture. *Mater. Sci. Eng. C* **2008**, *28*, 141–149.

(117) Kundu, B.; Lemos, A.; Soundrapandian, C.; Sen, P. S.; Datta, S.; Ferreira, J. M. F.; Basu, D. Development of Porous HAp and β-TCP Scaffolds by Starch Consolidation with Foaming Method and Drug-Chitosan Bilayered Scaffold Based Drug Delivery System. *J. Mater. Sci. Mater. Med.* **2010**, *21*, 2955–2969.

(118) Attard, G. S.; Glyde, J. C.; Göltner, C. G. Liquid-Crystalline Phases as Templates for the Synthesis of Mesoporous Silica. *Nature* **1995**, *378*, 366–368.

(119) Goltner, C. G.; Antonietti, M. Mesoporous Materials by Templating of Liquid Crystalline Phases. *Adv. Mater.* **1997**, *9*, 431–436.

(120) Schüth, F. Endo- and Exotemplating to Create High-Surface-Area Inorganic Materials. *Angew. Chemie Int. Ed.* **2003**, *42*, 3604–3622.

(121) Smarsly, B.; Antonietti, M. Block Copolymer Assemblies as Templates for the Generation of Mesoporous Inorganic Materials and Crystalline Films. *Eur. J. Inorg. Chem.* **2006**, *2006*, 1111–1119.

(122) Sharma, K. P.; Ganai, A. K.; Gupta, S. Sen; Kumaraswamy, G. Self-Standing Three-Dimensional Networks of Nanoparticles With Controllable Morphology by Dynamic Templating of Surfactant Hexagonal Domains. *Chem. Mater.* **2011**, *23*, 1448–1455.

(123) Imhof, A.; Pine, D. J. Ordered Macroporous Materials by Emulsion Templating. *Nature* **1997**, *389*, 948–951.

(124) Imhof, A.; Pine, D. J. Uniform Macroporous Ceramics and Plastics by Emulsion Templating. *Adv. Mater.* **1998**, *10*, 697–700.

(125) Imhof, A.; Pine, D. J. Preparation of Titania Foams. *Adv. Mater.* **1999**, *11*, 311–314.

(126) Zhang, H.;. Hardy, C. G.; Khimyak, Z. Y.; Rosseinsky, J. M.; Cooper, A. I. Synthesis of Hierarchically Porous Silica and Metal Oxide Beads Using Emulsion-Templated Polymer Scaffolds. **2004,** *16*, 4245–4256.

(127) Zhou, S.; Bismarck, A.; Steinke, J. H. G. Thermoresponsive Macroporous Scaffolds Prepared by Emulsion Templating. *Macromol. Rapid Commun.* **2012**, *33*, 1833–1839.

(128) Feinle, A.; Elsaesser, M. S.; Hüsing, N. Sol–gel Synthesis of Monolithic Materials with Hierarchical Porosity. *Chem. Soc. Rev.* **2016**, *45*, 3377–3399.

(129) Templin, M.; Franck, C. F.; Du Chesne A, A.; Leist; Zhang; Ulrich; Schadler; Wiesner. Organically Modified Aluminosilicate Mesostructures from Block Copolymer Phases. *Science (80-.).* **1997**, *278*, 1795–1798.

(130) Zhao, D.; Feng, W. L.; Huo; Melosh; Fredrickson; Chmelka; Stucky. Triblock Copolymer Syntheses of Mesoporous Silica with Periodic 50 to 300 Angstrom Pores. *Science* **1998**, *279*, 548–552.

(131) Stein, A.; Schroden, R. C. Colloidal Crystal Templating of Three-Dimensionally Ordered Macroporous Solids: Materials for Photonics and beyond. *Curr. Opin. Solid State Mater. Sci.* **2001**, *5*, 553–564.

(132) Jiang, P.; McFarland, M. J. Large-Scale Fabrication of Wafer-Size Colloidal Crystals, Macroporous Polymers and Nanocomposites by Spin-Coating. **2004**, *126*, 13778–13786.

(133) Stein, A.; Li, F.; Denny, N. R. Morphological Control in Colloidal Crystal Templating of Inverse Opals, Hierarchical Structures, and Shaped Particles. *Chem. Mater.* **2008**, *20*, 649–666.

(134) Zheng, Z.; Gao, K.; Luo, Y.; Li, D.; Meng, Q.; Wang, Y.; Zhang, D. Rapidly Infrared-

Assisted Cooperatively Self-Assembled Highly Ordered Multiscale Porous Materials. *J. Am. Chem. Soc.* **2008**, *130*, 9785–9789.

(135) Wang, L.; Wan, Y.; Li, Y.; Cai, Z.; Li, H.-L.; Zhao, X. S.; Li, Q. Binary Colloidal Crystals Fabricated with a Horizontal Deposition Method. *Langmuir* **2009**, *25*, 6753–6759.

(136) Nam, Y. S.; Yoon, J. J.; Park, T. G. A Novel Fabrication Method of Macroporous Biodegradable Polymer Scaffolds Using Gas Foaming Salt as a Porogen Additive. *J. Biomed. Mater. Res.* **2000**, *53*, 1–7.

(137) Yoon, J. J.; Kim, J. H.; Park, T. G. Dexamethasone-Releasing Biodegradable Polymer Scaffolds Fabricated by a Gas-Foaming/salt-Leaching Method. *Biomaterials* **2003**, *24*, 2323–2329.

(138) Şenel, S.; McClure, S. J. Potential Applications of Chitosan in Veterinary Medicine. *Adv. Drug Deliv. Rev.* **2004**, *56*, 1467–1480.

(139) Montjovent, M.-O.; Mathieu, L.; Hinz, B.; Applegate, L. L.; Bourban, P.-E.; Zambelli, P.-Y.; Månson, J.-A.; Pioletti, D. P. Biocompatibility of Bioresorbable Poly(L-Lactic Acid) Composite Scaffolds Obtained by Supercritical Gas Foaming with Human Fetal Bone Cells. *Tissue Eng.* **2005**, *11*, 1640–1649.

(140) Montjovent, M.-O.; Mathieu, L.; Schmoekel, H.; Mark, S.; Bourban, P.-E.; Zambelli, P.-Y.; Laurent-Applegate, L. A.; Pioletti, D. P. Repair of Critical Size Defects in the Rat Cranium Using Ceramic-Reinforced PLA Scaffolds Obtained by Supercritical Gas Foaming. *J. Biomed. Mater. Res. Part A* **2007**, *83*, 41–51.

(141) Ju, Y. M.; Park, K.; Son, J. S.; Kim, J.-J.; Rhie, J.-W.; Han, D. K. Beneficial Effect of Hydrophilized Porous Polymer Scaffolds in Tissue-Engineered Cartilage Formation. *J. Biomed. Mater. Res. Part B Appl. Biomater.* **2008**, *85*, 252–260.

(142) Dehghani, F.; Annabi, N. Engineering Porous Scaffolds Using Gas-Based Techniques. *Curr. Opin. Biotechnol.* **2011**, *22*, 661–666.

(143) Ji, C.; Annabi, N.; Hosseinkhani, M.; Sivaloganathan, S.; Dehghani, F. Fabrication of Poly-DL-Lactide/polyethylene Glycol Scaffolds Using the Gas Foaming Technique. *Acta Biomater.* **2012**, *8*, 570–578.

(144) Monnier, A.; Schuth, F.; Huo, Q.; Kumar, D.; Margolese, D.; Maxwell, R. S.; Stucky, G. D.; Krishnamurty, M.; Petroff, P.; Firouzi, A.; Janicke, M.; Chmelka, B. F. Cooperative Formation of Inorganic-Organic Interfaces in the Synthesis of Silicate Mesostructures. *Science.* **1993**, *261*, 1299–1303.

(145) Song, L.; Bly, R. K.; Wilson, J. N.; Bakbak, S.; Park, J. O.; Srinivasarao, M.; Bunz, U.

H. F. Facile Microstructuring of Organic Semiconducting Polymers by the Breath Figure Method: Hexagonally Ordered Bubble Arrays in Rigid Rod-Polymers. *Adv. Mater.* **2004**, *16*, 115–118.

(146) Böker, A.; Lin, Y.; Chiapperini, K.; Horowitz, R.; Thompson, M.; Carreon, V.; Xu, T.; Abetz, C.; Skaff, H.; Dinsmore, A. D.; Emrick, T.; Russell, T. P. Hierarchical Nanoparticle Assemblies Formed by Decorating Breath Figures. *Nat. Mater.* **2004**, *3*, 302–306.

(147) Connal, L. A.; Gurr, P. A.; Qiao, G. G.; Solomon, D. H. From Well Defined Star-Microgels to Highly Ordered Honeycomb Films. *J. Mater. Chem.* **2005**, *15*, 1286–1292.

(148) Katsuki, H.; Kawahara, A.; Ichinose, H. Preparation and Some Properties of Porous Alumina Ceramics Obtained by the Gelatination of Ammonium Alginate. *J. Mater. Sci.* **1992**, *27*, 6067–6070.

(149) Bouler, J.M.; Trècant, M.; Delécrin, J.; Royer, J.; Passuti, N.; Daculsi, G. Macroporous Biphasic Calcium Phosphate Ceramics: Influence of Five Synthesis Parameters on Compressive Strength. *J. Biomed. Mater. Res.* **1996**, *32*, 603–609.

(150) Androff, N. W.; Francis, L. F.; Velamakanni, B. V. Macroporous Ceramics from Ceramic-Polymer Dispersion Methods. *AIChE J.* **1997**, *43*, 2878–2888.

(151) Prado da Silva, M. H.; Lemos, A. F.; Gibson, I. R.; Ferreira, J. M. F.; Santos, J. D. Porous Glass Reinforced Hydroxyapatite Materials Produced with Different Organic Additives. *J. Non. Cryst. Solids* **2002**, *304*, 286–292.

(152) Bowden, M. E.; Rippey, M. S. Porous Ceramics Formed Using Starch Consolidation. *Key Eng. Mater.* **2002**, *206–213*, 1957–1960.

(153) Thijs, I.; Luyten, J.; Mullens, S. Producing Ceramic Foams with Hollow Spheres. *J. Am. Ceram. Soc.* **2004**, *87*, 170–172.

(154) Wang, C.; Kasuga, T.; Nogami, M. Macroporous Calcium Phosphate Glass-Ceramic Prepared by Two-Step Pressing Technique and Using Sucrose as a Pore Former. *J. Mater. Sci. Mater. Med.* **2005**, *16*, 739–744.

(155) Studart, A. R.; Gonzenbach, U. T.; Tervoort, E.; Gauckler, L. J. Processing Routes to Macroporous Ceramics: A Review. *J. Am. Ceram. Soc.* **2006**, *89*, 1771–1789.

(156) Laurie, J.; Bagnall, C. M.; Harris, B.; Jones, R. W.; Cooke, R. G.; Russell-Floyd, R. S.; Wang, T. H.; Hammett, F. W. Colloidal Suspensions for the Preparation of Ceramics by a Freeze Casting Route. *J. Non. Cryst. Solids* **1992**, *147–148*, 320–325.

(157) Statham, M. J.; Hammett, F.; Harris, B.; Cooke, R. G.; Jordan, R. M.; Roche, A. Net-Shape Manufacture of Low-Cost Ceramic Shapes by Freeze-Gelation. *J. Sol-Gel Sci. Technol.* **1998**, *13*, 171–175.

(158) Fukasawa, T.; Ando, M.; Ohji, T.; Kanzaki, S. Synthesis of Porous Ceramics with Complex Pore Structure by Freeze-Dry Processing. *J. Am. Ceram. Soc.* **2001**, *84*, 230–232.

(159) Fukasawa, T.; Deng, Z.-Y.; Ando, M.; Ohji, T.; Goto, Y. Pore Structure of Porous Ceramics Synthesized from Water-Based Slurry by Freeze-Dry Process. *J. Mater. Sci.* **2001**, *36*, 2523–2527.

(160) Hench, L. L.; Polak, J. M.; Nalla, R. K.; Tomsia, A. P. Third-Generation Biomedical Materials. *Science.* **2002**, *295*, 1014–1017.

(161) Mukai, S. R.; Nishihara, H.; Tamon, H. Formation of Monolithic Silica Gel Microhoneycombs (SMHs) Using Pseudosteady State Growth of Microstructural Ice Crystals. *Chem. Commun.* **2004**, *0*, 874.

(162) Nishihara, H.; Mukai, S. R.; Yamashita, D., and; Tamon, H. ; Ordered Macroporous Silica by Ice Templating. *Chem. Mater.* **2005** , *17*, 683–689.

(163) Gutiérrez, M. C.; Ferrer, M. L.; del Monte, F. Ice-Templated Materials: Sophisticated Structures Exhibiting Enhanced Functionalities Obtained after Unidirectional Freezing and Ice-Segregation-Induced Self-Assembly. *Chem. Mater.* **2008**, *20*, 634–648.

(164) Deville, S.; Sylvain. Freeze-Casting of Porous Biomaterials: Structure, Properties and Opportunities. *Materials (Basel).* **2010**, *3*, 1913–1927.

(165) Deville, S. Ice-Templating, Freeze Casting: Beyond Materials Processing. *J. Mater. Res.* **2013**, *28*, 2202–2219.

(166) Wu, S.; Zhu, C.; He, Z.; Xue, H.; Fan, Q.; Song, Y.; Francisco, J. S.; Zeng, X. C.; Wang, J. Ion-Specific Ice Recrystallization Provides a Facile Approach for the Fabrication of Porous Materials. *Nat. Commun.* **2017**, *8*, 15154.

(167) Kim, J.-W.; Tazumi, K.; Okaji, R.; Ohshima, M. Honeycomb Monolith-Structured Silica with Highly Ordered, Three-Dimensionally Interconnected Macroporous Walls. *Chem. Mater.* **2009**, *21*, 3476–3478.

(168) Zuo, K. H.; Zhang, Y.; Zeng, Y.-P.; Jiang, D. Pore-Forming Agent Induced Microstructure Evolution of Freeze Casted Hydroxyapatite. *Ceram. Int.* **2011**, *37*, 407–410.

(169) Huang, Z.; Zhou, K.; Lei, D.; Li, Z.; Zhang, Y.; Zhang, D. Fabrication of CaSiO3 Bioceramics with Open and Unidirectional Macro-Channels Using an Ice/fiber-

Templated Method. *Ceram. Int.* **2013**, *39*, 6035–6040.

(170) Shanti, N. O.; Araki, K.; Halloran, J. W. Particle Redistribution During Dendritic Solidification of Particle Suspensions. *J. Am. Ceram. Soc.* **2006**, *89*, 2444–2447.

(171) Schoof, H.; Apel, J.; Heschel, I.; Rau, G. Control of Pore Structure and Size in Freeze-Dried Collagen Sponges. *J. Biomed. Mater. Res.* **2001**, *58*, 352–357.

(172) Zhang, H.; Cooper, A. I. Aligned Porous Structures by Directional Freezing. *Adv. Mater.* **2007**, *19*, 1529–1533.

(173) Wu, X.; Liu, Y.; Li, X.; Wen, P.; Zhang, Y.; Long, Y.; Wang, X.; Guo, Y.; Xing, F.; Gao, J. Preparation of Aligned Porous Gelatin Scaffolds by Unidirectional Freeze-Drying Method. *Acta Biomater.* **2010**, *6*, 1167–1177.

(174) Deville, S.; Viazzi, C.; Leloup, J.; Lasalle, A.; Guizard, C.; Maire, E.; Adrien, J.; Gremillard, L. Ice Shaping Properties, Similar to That of Antifreeze Proteins, of a Zirconium Acetate Complex. *PLoS One* **2011**, *6*, e26474.

(175) Waschkies, T.; Oberacker, R.; Hoffmann, M. J. Control of Lamellae Spacing During Freeze Casting of Ceramics Using Double-Side Cooling as a Novel Processing Route. *J. Am. Ceram. Soc.* **2009**, *92*, S79–S84.

(176) Inada, T.; Modak, P. R. Growth Control of Ice Crystals by Poly(vinyl Alcohol) and Antifreeze Protein in Ice Slurries. *Chem. Eng. Sci.* **2006**, *61*, 3149–3158.

(177) Pawelec, K. M.; Husmann, A.; Best, S. M.; Cameron, R. E. Altering Crystal Growth and Annealing in Ice-Templated Scaffolds. *J. Mater. Sci.* **2015**, *50*, 7537–7543.

(178) Soon, Y.-M.; Shin, K.-H.; Koh, Y.-H.; Lee, J.-H.; Kim, H.-E. Compressive Strength and Processing of Camphene-Based Freeze Cast Calcium Phosphate Scaffolds with Aligned Pores. *Mater. Lett.* **2009**, *63*, 1548–1550.

(179) Tang, Y.; Miao, Q.; Qiu, S.; Zhao, K.; Hu, L. Novel Freeze-Casting Fabrication of Aligned Lamellar Porous Alumina with a Centrosymmetric Structure. *J. Eur. Ceram. Soc.* **2014**, *34*, 4077–4082.

(180) Bai, H.; Chen, Y.; Delattre, B.; Tomsia, A. P.; Ritchie, R. O. Bioinspired Large-Scale Aligned Porous Materials Assembled with Dual Temperature Gradients. *Sci. Adv.* **2015**, *1*, e1500849–e1500849.

(181) Lichtner, A.; Roussel, D.; Jauffrès, D.; Martin, C. L.; Bordia, R. K. Effect of Macropore Anisotropy on the Mechanical Response of Hierarchically Porous Ceramics. *J. Am. Ceram. Soc.* **2016**, *99*, 979–987.

(182) Roy, S.; Butz, B.; Wanner, A. Damage Evolution and Domain-Level Anisotropy in Metal/ceramic Composites Exhibiting Lamellar Microstructures. *Acta Mater.* **2010**, *58*,

2300–2312.

(183) Flauder, S.; Gbureck, U.; Müller, F. A. Structure and Mechanical Properties of β-TCP Scaffolds Prepared by Ice-Templating with Preset Ice Front Velocities. *Acta Biomater.* **2014**, *10*, 5148–5155.

(184) Rajamanickam, R.; Kumari, S.; Kumar, D.; Ghosh, S.; Kim, J. C.; Tae, G.; Sen Gupta, S.; Kumaraswamy, G. Soft Colloidal Scaffolds Capable of Elastic Recovery after Large Compressive Strains. *Chem. Mater.* **2014**, *26*, 5161–5168.

(185) Seuba, J.; Deville, S.; Guizard, C.; Stevenson, A. J. Mechanical Properties and Failure Behavior of Unidirectional Porous Ceramics. *Sci. Rep.* **2016**, *6*, 24326.

(186) Lin, Y; Skaff, H ; Böker, A ; Dinsmore, A. D.,; Emrick, T; Russell T. P. Ultrathin Cross-Linked Nanoparticle Membranes. *J. Am. Chem. Soc.* **2003**, *125*, 12690.

(187) Mueggenburg, K. E.; Lin, X.-M.; Goldsmith, R. H.; Jaeger, H. M. Elastic Membranes of Close-Packed Nanoparticle Arrays. *Nat. Mater.* **2007**, *6*, 656–660.

(188) Ergun, S.; Orning, A. A. Fluid Flow through Randomly Packed Columns and Fluidized Beds. *Ind. Eng. Chem.* **1949**, *41*, 1179–1184.

Fire retardant, self-extinguishing inorganic-polymer composite memory foams

In this chapter, we demonstrate the application of ice templating to prepare fire retardant foams from inorganic/polymer hybrids. Importantly, these foams do not incorporate fire retardant additives. Since these foams are predominantly comprised of inorganic, they exhibit exceptional fire retardance in torch burn tests and, are self-extinguishing. After subjecting to a flame, the foam retains its porous structure and does not drip. In microcombustion calorimetry, the hybrid foams show a peak heat release rate that is only 25% that of a commercial fire retardant polyurethane. Despite the high inorganic content, the hybrid foams are elastic to large compressional strain and exhibit tunable mechanical response, including viscoelastic "memory".

2.1 Introduction

Flexible polymeric foams based on latex rubber and polyurethane find use in applications ranging from mattresses, furniture, upholstery and automotive seats.[1,2] The annual global production of flexible polyurethane foams alone exceeds 7 million tons currently, with an anticipated annual growth exceeding 5% in Asia over the next 5 years.[3] This growth is fuelled, in part, by the remarkable improvements that have been made in polyurethane chemistry. It is now possible to have exquisite control over the pore structure[4] of the foams, over transport of vapor through foams and over the viscoelastic response of the foams.[5] Thus, foams that are "breathable" and that have "memory"[6] (viz. that conform to the shape of an object placed on it, and gradually recover their original shape after removal of the object) are now available. All flexible polymeric foams are combustible – therefore, their widespread use in households, in public transportation (including seating in buses, railways and airplanes) and in auditoria has necessitated the development of strict fire safety standards in several countries. For example, in the United States, in Canada and in the United Kingdom, safety regulations mandate the use of foam materials that meet minimal fire retardant specifications.[7] These fire safety standards mandate the resistance to ignition and flame spread, as well as resistance to dripping on being ignited, that must be exhibited by polymeric foams.

For foams to be compliant with fire safety standards, fire retardant additives are typically added to the polymers. Brominated compounds, including polybrominated diphenyl esters were the most commonly used legacy flame retardants. However, these compounds have been identified as persistent organic pollutants (POP), due to their toxicity and persistence in the environment.[8–11] Environmental concerns have led to the recent adoption of another class of compounds, organophosphates, as flame retardant additives.[12–15] These include tris(1,3-dichloro-2-propyl) phosphate (TDCPP); 2,3,4,5-tetrabromo-ethylhexylbenzoate (TBB) and tris(2-chloroethyl) phosphate (TCEP). However, recent studies have revealed that the presence of these organophosphate compounds in marine sediments in the Arctic Ocean.[16] This suggests that these flame retardants too are persistent and undergo transport over long distances and might, therefore, invite sanction due to environmental reasons. While there are efforts[17] towards sustainable, bio-based fire retardant compounds, these have not yet been adopted commercially.

Researchers have explored the flame retardant properties of polymer composites,[18] especially nanocomposites. For example, polymer composites that contain montmorillonites, magnesium hydrate, alumina and silsesquioxanes have demonstrated improvements in flame retardance, due to enhanced char formation and reduced dripping of the polymer.[19–24] However, typically, addition of inorganic fillers results in the reduction of the compressive strength and strain at failure of the polymer.[25]Special processing techniques that are challenging to scale up to industrial practice are required to produce elastomeric materials that retain their mechanical performance even after reinforcing with inorganic nanofillers.[26] Recently, the fire retardant properties of composites of polymers with anisotropic carbon-based particles (such as rod-like carbon nanotubes and plate-like graphene or graphene oxide) have been investigated. It has been hypothesized that the formation of jammed percolated networks of carbon nanotubes in a polymeric matrix supresses the burning process.[27,28] Plate-like carbon nanoparticles also have promised in retarding the flammability of polymer matrices.[29–31]However, in such nanocomposites too, the mechanical properties at failure are compromised, restricting their applications. A different sort of composite can be prepared by surface treatment of polymeric foams to create a char forming layer to inhibit flammability. Such composites can be prepared, for example, by employing layer-by-layer techniques.[32–36] Sun et al.[37] have reported the use of unidirectional ice- templating[38,39] to prepare polymer aerogels[40] that were surface coated with silica nanoparticles to improve their flame retardance. Recently, Cho et al.[41]have reported the formation of conformal coatings of polydopamine on the surface of polyurethane foams that supresses burning of the foam. Coating based strategies[42]require additional processing steps, thus increasing both complexity and cost of the final product. Further, coated products suffer from the possibility of delamination of the protective surface layer.

Therefore, there is clearly a need for foams with excellent fire retardant properties achieved without compromising mechanical properties and that can be prepared using scalable techniques. Here, we demonstrate hybrid inorganic/polymer foams that are mechanically resilient and that have superior fire retardant properties compared with commercial polyurethane foams containing FR additives. Interestingly, these foams exhibit tunable memory, viz. the time scale for complete recovery can be varied. Further, varying particle concentration in the hybrid foams allows us to tune their mechanical stiffness over a wide range. Flame applied to this foam does not spread and is self-extinguished. Peak release rates for these hybrid foams are about 75% lower than those for the FR-polyurethane foams

(FR-PU). Remarkably, these hybrid foams do not contain any fire retardant additive. Rather, they are predominantly comprised of inorganic particles (> 90% w/w) bonded together through a cross-linked polymer. Notably, these foams are prepared using environmentally benign components, in a process that uses water, an environmentally friendly solvent.

2.2 Experimental

2.2.1 Materials:

Polyethylenimine (PEI, branched polymer with supplier specified molecular weight M_w= 750 kDa) and 1,4-butanediol diglycidyl ether were obtained from Sigma Aldrich and were used as received. We performed SEM on the silica particles and used image analysis to obtain an average size and standard deviation of 1.03±0.08 μm, consistent with supplier specifications. Surface charge distribution on the silica surface in aqueous dispersion was earlier reported by our group[43] using zeta potential analyser and the measured peak surface charge was -71.1 mV. PEI is a weak polycation, and is protonated in neutral or acidic aqueous solution. PEI coated silica particles shows charge inversion to give a zeta potential of 38.1 mV as reported earlier by our group.[43] Distilled deionized water (resistivity ~18.2 MΩ.cm) from a Millipore MilliQ unit was used to prepare sponges. A commercial fire retardant polyurethane (FR-PU) sponge was generously supplied to us by Dr. Sangaj from the Indian Polyurethane Technical Center and was used as received. This sponge is designated FR-PU sponge, indicating that it is a fire retardant sponge. This sponge is an open cell foam used in interior applications in automotives and passes the FMVSS 302 test (a horizontal flammability test for burn resistance).[44]

2.2.2 Fabrication of composite sponge:

A detailed protocol for the ice-templated synthesis of polymer –particle hybrid sponges was described in Scheme 2.1. Briefly, in a 2 ml polypropylene vial, 120 mg silica particle was dispersed in 1092 μl of water by sonication for 15 min. To this, 100 μl PEI solution (from a 200 mg/ml stock solution) was added. Here we use PEI, an inexpensive, commercially available polymer to coat the particle surface. To the PEI-coated particle dispersion, 8 mg cross-linker (1,4-butanediol diglycidyl ether) was mixed and the mixture was maintained at -10 °C. On freezing the aqueous dispersion, the silica particles, PEI and cross-linker are concentrated at the grain boundaries between ice crystals. The enhanced local concentration of polymer and cross-linker at the grain boundaries facilitates the cross-linking reaction, that

takes place in the frozen condition. We allowed 24 h for the cross-linking reaction to be completed. Subsequently, melting of ice at room temperature, followed by drying, affords a composite sponge. This sponge is termed as "S10", since it is prepared by ice-templating a ϕ = 10% (w/v) dispersion of silica particles. Similarly, we also prepare a composite sponge (S5) by ice templating ϕ = 5% (w/v) silica dispersions, where the ratio of silica to polymer and cross-linker is identical to S10.

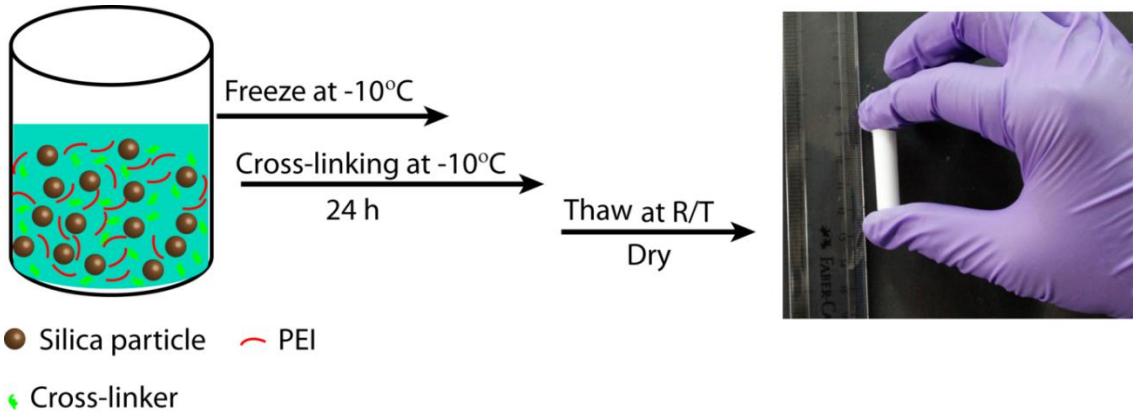

Scheme 2.1: Schematic representation for a route to prepare ice-templated composite sponge.

2.2.3 Control sponge:

We also prepared an ice-templated sponge that comprises purely cross-linked PEI, prepared using ice-templating (Scheme 2.2). This sponge was prepared at the same ratio of PEI to cross-linker concentrations as used for the composite sponge and is termed "control sponge".

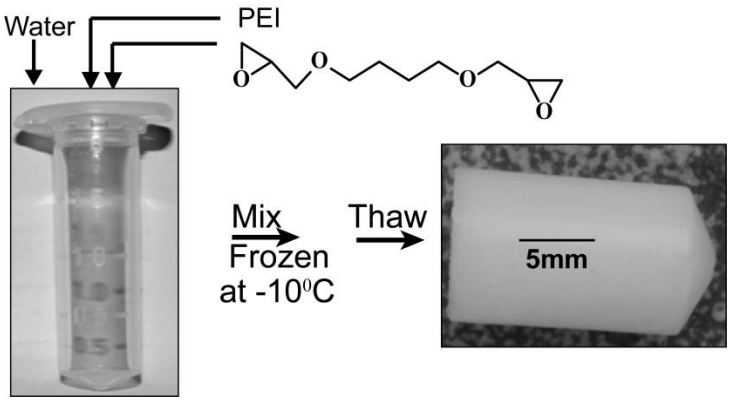

Scheme 2.2: Schematic representation for a route to prepare ice-templated polymer sponge.

2.3 Characterization

2.3.1 Scanning Electron Microscopy (SEM):

Morphology of the ice-templated sponges was imaged using a Quanta 200 3D scanning electron microscope. Sponge surfaces were sputtered using an Au target prior to SEM analysis to prevent charging.

2.3.2 Mechanical Property:

Mechanical properties of sponges were measured using a strain controlled rheometer from TA Instruments, RSA-III, equipped with a normal force transducer. All the samples were subjected to compressive strain at a rate of 0.05 mm/s. Compression set of the sponge was evaluated following ASTM D1056. The sponge was compressed to a strain of 50 % and was held compressed for 22 h at 70 °C. After 22 h, the load was released and sample height was measured after allowing 30 minutes of equilibration at room temperature. Compression set was calculated using equation 5.1.

$$\boldsymbol{CS} = \left[\frac{(\boldsymbol{h_0} - \boldsymbol{h_i})}{(\boldsymbol{h_0} - \boldsymbol{h_c})}\right] \times \mathbf{100} \qquad (\mathbf{5.1})$$

$\boldsymbol{CS}$ = compression set, $\boldsymbol{h_0}$= original height, $\boldsymbol{h_i}$= final height, $\boldsymbol{h_c}$= compressed height

2.3.3 Memory effect:

Viscoelastic recovery of foams was measured as follows. The foam sample was compressed to 50% of its initial height and then the strain was released and the foam was allowed to recover. We record and analyse video data using code written in Python to monitor the height of the sponge as it recovers.

2.3.4 Thermogravimetric Analysis (TGA):

The thermal stability of the sponges was investigated with a thermogravimetric analyser (STA 7000), by heating the samples from 100 to 800 °C at a heating rate of 1 °C/min in a nitrogen atmosphere (flow 50 mL/min).

2.3.5 Flammability Test:

Sponge flammability was qualitatively evaluated by direct exposure to flame using a Bunsen burner for 10 s, similar to the procedure in the UL 94 standard. The Bunsen burner flame

height was set to ≈ 30 mm. We test flammability for cylindrical samples (20 mm long, 8 mm diameter) by positioning the tip of the sample 15 mm above the top of a blue flame generated by the burner. A blue flame from the burner indicates that the flame temperature is approximately 1200 °C. The burning of samples was evaluated from the video records of this experiment.

2.3.6 Combustion Test:

hSponge flame retardancy was also evaluated using a micro combustion calorimeter (MCC) and tests were carried out at the Interscience Fire Laboratory, UK according to ASTM D 7309 (Methods A and B). A sample size of approximately 5 mg was tested at a constant heating rate between 0.2 and 2 K/s under anaerobic (Method A) and aerobic (Method B) conditions, from 100 to 800 °C. The combustor temperature was set at 900 °C and nitrogen/oxygen flow rate was set at 80/20 ml/min. All the samples were conditioned at 23±2 °C and 50±5% relative humidity for 3 days prior to testing.

2.4 Results and Discussion

2.4.1 Mechanical properties

Ice-templated sponges are highly compressible and recover completely after large compressive deformation. The mechanical response is characteristic of the hybrid colloid/polymer architecture of the sponge.It originates from the cross-linked polymer structure that forms a network that holds the particles together. We do not observe a role for particle interlocking for the large strain elasticity. This has been discussed in detail in recent work from our group.[45,46] Further, it is possible to vary the modulus of the sponges. For example, the elastic modulus (E') of the composite sponges can be varied two-fold by adjusting particle concentration from S5 to S10 (Table 5.1). We showed that E' scales with ϕ for composite sponges, where ϕ is the concentration of the ice templated dispersion. E' for control and FR-PU sponges is in the range of 4000 to 7000 Pa (Table 2.1).

Table 2.1: Elastic moduli of the sponges are obtained from stress-strain curve at very low values of strain (≈1-2%) in dry state.

Samples	Elastic modulus (Pa)
S5	24000±500
S10	57000±8000
Control	4100±400
FR-PU sponge	6500±200

The "compression set" of an elastomeric material characterizes its ability to return to its original state after a holding in a compressed state for a prolonged time at a constant temperature. Materials with lower compression set are able to better resist permanent deformation. For open cell elastomeric sponges, it is desirable for the compression set to be less than 25%. We performed compression set measurements following the ASTM D1056 protocol that are prescribed for elastomeric sponges. The test sponge is compressed to a strain of 50% and is held at that strain for 22 h at a temperature of 70 °C. Then, the strain is released and the sponge is allowed to recover for an hour at room temperature. Then, the dimensions of the sponge are measured to determine compression set. The ice-templated hybrid sponges, S5 and S10 show compression set of 6±3 % and 18±5 %, respectively, higher than that for FR-PU (7%), but below the 25% threshold. The hybrid sponges continue to recover slowly even after an hour and completely regain their original size after a few hours at room temperature (Figure 2.1). Thus, the initial rapid recovery is followed by a slower process for complete recovery to the original size.

We track the recovery of sponge height after strain is released (Figure 2.2). All sponges, FR-PU and the hybrid sponges, are elastic and eventually recover to their original uncompressed size. The sponges exhibit a rapid initial recovery, followed by slower process to completely recover their original size. For FR-PU and S5, the sponges rapidly recover to 95% of their original size within 10 s and 60 s respectively, and then recover to their original size over about 30 minutes. In contrast, S10 expands to about 75% of its original size within 35 s, and then recovers to 88% after 30 min and to 93% after 90 min. For S10, complete recovery is slow and takes several hours. Thus, while the hybrid sponges are elastic and eventually recover to their original size after release of compressive strain, the rate of recovery is controlled by ϕ, and can be varied over a considerable range. We note in passing that water-

saturated hybrid sponges (both S5 and S10) exhibit complete recovery very rapidly, within minutes of releasing strain. SEM images of the sponges before and after the compression set experiment suggest that the cellular structure of the foam is well preserved for S5, and S10 sponges and no microstructural damage is evident. FR-PU too recovers rapidly from after strain is released and there is no change in the pore microstructure before and after compression (Figure 2.1).

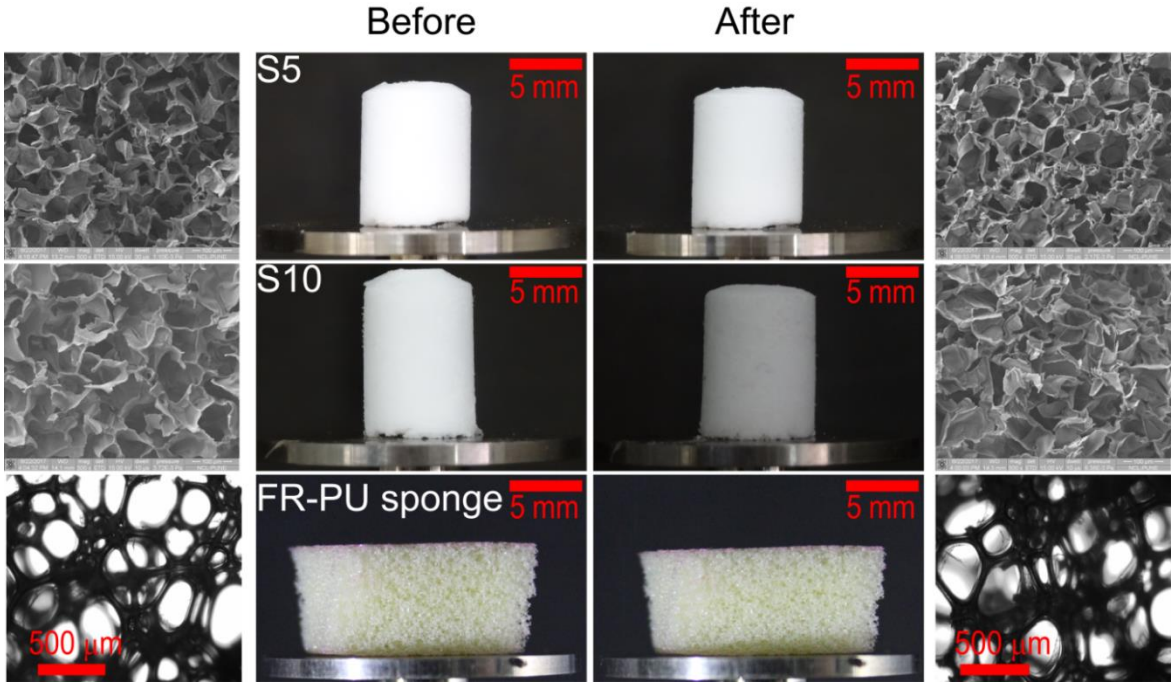

Figure 2.1: Photographs of the sponges before and after compression set experiment (middle two columns). In the left and right panel of the photographs we present their corresponding microscopy images before and after compression set experiment, respectively.

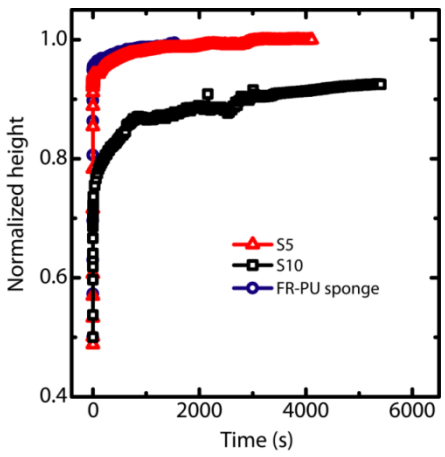

Figure 2.2: Strain Recovery-time Measurement starting at 50% compression. Time zero in this example when the top plate started moving (≈ 7.5 mm/s) from the sponge surface.

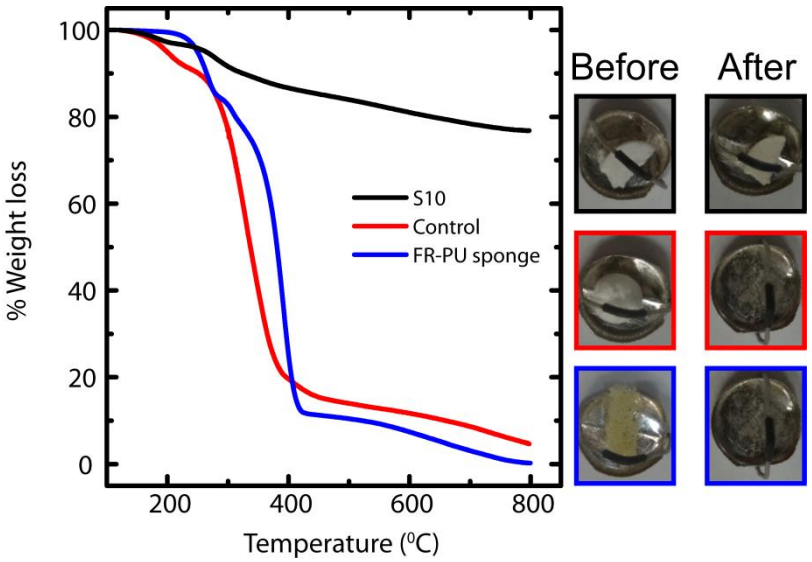

Figure 2.3: Thermogravimetric analysis (TGA) in nitrogen shows that composite sponge has higher thermal stability than the cross-linked polymer (control) and the FR-PU sponges. The images before and after TGA analysis shows composite sponge maintains the original shape after degradation at 800°C.

2.4.3 Thermal Analysis

We have performed thermogravimetric analysis (TGA) on the sponges by heating them to 800 °C in nitrogen gas, at a heating rate of 10 °C min^{-1} (Figure 2.3a). All samples were dried thoroughly prior to TGA measurements. The control sponge (comprising purely of crosslinked polymer) starts degrading at 170 °C with a maximum degradation of 333 °C and completely decomposes by 400 °C leaving no residue (Figure 2.3). The thermogram of FR-PU sponge shows two distinct degradation steps: in the first step, 20% weight loss occurs between 200 and 286 °C and in the second step 70% weight loss occurs between 286 and 427 °C. This TGA curve is characteristic of soft PU.[47]In contrast, only 13% weight loss occurs in case of S10 between 200 and 650 °C leaving significant particle residue. The residue of S10, after the TGA experiment, maintains the shape of the original sample. This suggests that there is no collapse in the structure after the TGA heating and the sponge microstructure is preserved (Figure 2.3, photograph). The ratio of inorganic silica to organic cross-linked polymer is similar for S5 and S10. Therefore, the TGA curve from heating S5 is similar to that from S10. In the rest of the manuscript, we test the flame retardant behaviour of S10, and compare this with the FR-PU and the control pure cross-linked polymeric foam.

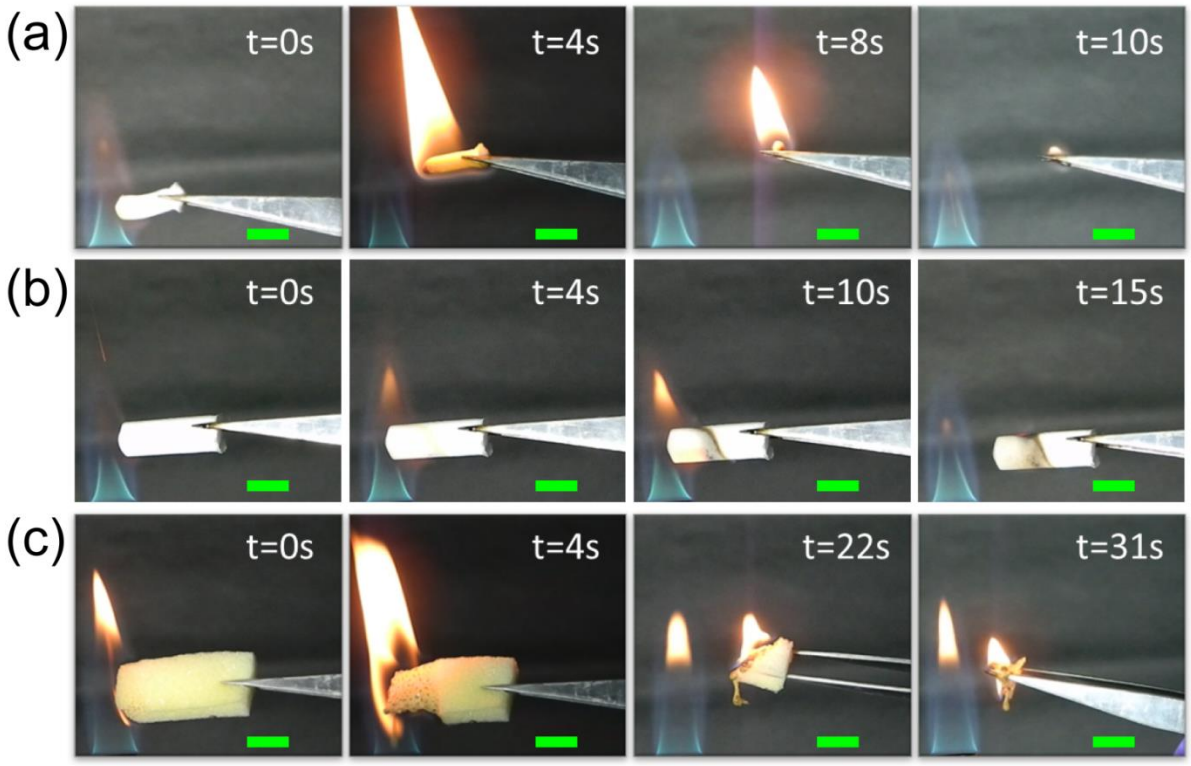

Figure 2.4: Photographs showing the torch burn test for the following samples: (a) control, (b) composite, and (c) FR-PU sponges. Samples were ignited using a Bunsen burner (similar to UL 94 standard). While cross-linked polymer and FR-PU sponges burned vigorously, composite sponge self-extinguished within 5 s after removal from the burner flame. Scale bars in the photographs correspond to 10 mm.

2.4.4 Flame Retardant Behavior

Flammability of the sponges is tested using a torch burn test, similar to UL-94. The behaviour of FR-PU, the control sponge and S10 are shown in Figure 2.4. The control sponge (based purely on cross-linked PEI) ignites as soon as it is exposed to the flame and the flame spreads quickly along the axis of the sample. We observe a significant shrinkage of the sample as it burns. We attribute the high flame height to the release of volatile combustion products that interfere with the formation of the char heat-transfer barrier at the interface between gas and condensed phase, during burning. FR-PU sponge on the other hand swells and burns less aggressively when compared to the control sponge. The composite sponge, S10, generates a small flame at its tip section where the burner flame is in contact, but the flame self-extinguishes within 5 s. When S10 burns, initially the small flame burns the cross-linked polymeric component. The char from burning the organic, together with the underlying network of silica particles forms a barrier that prevents flame spread and that is

mechanically rigid so that there is no dripping of the molten sponge during the propagation of the fire.

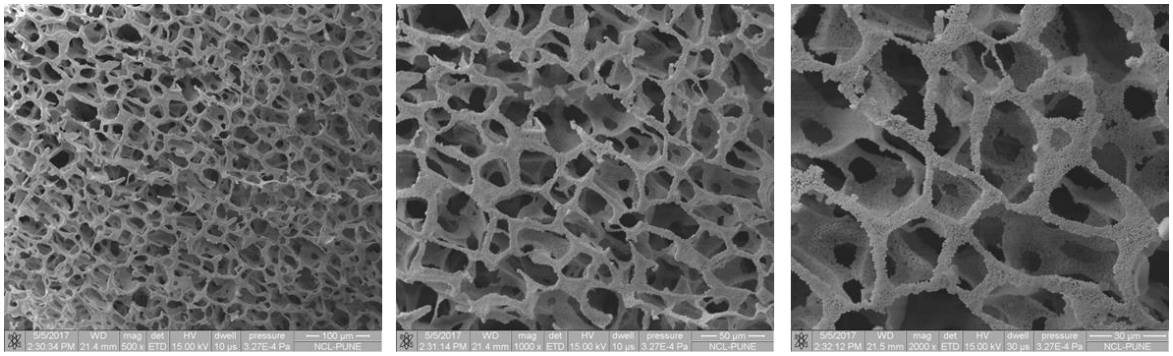

Figure 2.5 SEM images of the post-burn samples at different magnifications indicate that the composite sponge retains its structural integrity on exposure to flame. Image at higher magnification suggest that the hybrid silica/polymer structure is preserved in the interior of the sample and only the exterior portions of the sample are burnt by the flame.

Dripping of molten polymer can cause severe injuries to people and also ignite other materials in the vicinity. The fact that the hybrid sponges do not melt or drip adds a strong element of fire safety to these sponges. A representative cross-section of the post-burn sample was examined using SEM and we observe that the cellular morphology of the sponge is well-preserved even after exposure to the Bunsen flame (Figure 2.5). Thus, the composite sponges represent self-extinguishing, flame retardant materials. It is worth noting that, in contrast to recently reported advances in fire retardant materials, our composite sponge does not contain any environmentally hazardous additives and is obtained by a single step ice-templating process, with no coating steps.

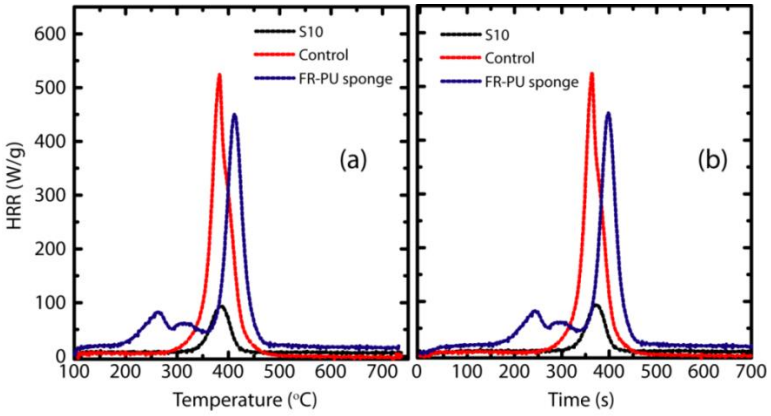

Figure 2.6 HRR curves as a function of (a) temperature, and (b) time for S10, control and FR-PU sponges by micro combustion calorimetry (MCC- Method A test).

2.4.5 Micro Combustion Calorimetry

To get more insights on the pyrolysis and the flame retardancy of the foams, we tested specimens using MCC (micro combustion calorimetry) using a standard protocol (ASTM D 7309). In the MCC test, 5 mg of the test sample (dimension of FR-PU ≈ 5.9 mm x 5.4 mm x 4.4 mm; of S10 ≈ 6 mm x 3.1 mm x 3.1 mm) is subjected to controlled heating in an anaerobic environment, viz., the sample experiences controlled thermal decomposition. During this process, the heat of combustion of the volatile gaseous component of the specimen is measured. In a second independent measurement, a fresh specimen is subjected to controlled heating in an aerobic environment. In this controlled oxidative thermal decomposition method, the sample is heated from 100 to 800 °C at 0.8 °C s^{-1} in a dry air atmosphere and the combustor temperature is set at 900 ˚C. The baseline oxygen concentration is 20% O_2 v/v and the net calorific value of the specimen gases and solid residue are measured during the test. Each test is repeated three times for each sample and values of measured parameters are averaged. Heat release curves (HRR) from the MCC measurements are recorded as a function of temperature and time. We define the temperature

Table 2.2: MCC results for control, composite and FR-PU sponges following Method A. The samples were tested in triplicate and the values of measured parameters are averaged.

Samples	T_p(˚C)	A-pHRR(W/g) (% reduction)	A-THR (kJ/g) (% reduction)	A-HR capacity (J/g-K)	% Char residue
Control	378±4	477± 45	34± 7	552± 50	1.14
S10	387±2	113± 16(76.3, 75.4)	12± 2 (70.7, 67.3)	130± 18	69
FR-PU sponge	411±1	453± 10	36± 3	526± 14	11.01

for the peak in heat release rate (pHRR) as T_p. In Figure 2.6 we compare MCC data from Method A for the commercial FR-PU sponge, the cross-linked PEI control sponge and the composite sponge (S10). PU foams, one of the most flammable polymeric materials, are characterized by a large heat release curve in MCC. FR-PU shows two peaks in the HRR.

The HRR increases slowly, showing a broad low intensity peak at 260 °C around 240 s and then exhibits a rapid burning to reach the pHRR at T_p = 410 °C around 400 s (Figure 2.6 a-b ,Table 2.2). Thus, FR-PU undergoes two step degradation. We attribute the first peak between 200 and 270 °C to the cleaving of low molecular weight species from the PU backbone while the second peak at 410 °C represents complete decomposition. The control sponge reaches a pHRR (476 W/g) at T_p = 378 °C leaving negligible char residue (≈ 1%) after complete decomposition at 800 °C. In contrast to the FR-PU, the ice-templated composite sponge, S10 exhibits single step degradation. The HRR for S10 shows T_p = 385 °C, corresponding to a peak value of 113 W/g (Figure 2.6 a-b). Since heat released during burning of a material can make the combustion self-sustaining, pHRR is considered as one of the most important parameter to evaluate fire safety.[48] It reflects the point in a fire where the heat generation is sufficient to propagate the flame or ignite adjacent material. The reduction in the total heat release in Method A (A-THR) and in pHRR for S10 relative to FR-PU is about 75% (Table 2.2). This is consistent with our observations during the torch burn test and indicates that the susceptibility of S10 to fire is significantly lower than for the control sponge or for FR-PU. We define the average heat release capacity (A-HR capacity) as the pHRR divided by the nominal heating rate (0.8 °C s^{-1}). The A-HR capacity of control and FR-PU sponges are 552 and 526 $Jg^{-1}K^{-1}$ respectively (Table 2.2). In comparison, S10 has an A-HR capacity of 130 $Jg^{-1}K^{-1}$, over 75% lower than the control sponge and FR-PU. The A-HR capacity is an indication of the thermal stability of a material; a low A-HR capacity is considered a good predictor of ignition resistance. Thus, S10 exhibits a significantly lower fire hazard compared to a commercial fire retardant PU. We also note that at the end of the MCC Method A experiment, S10 leaves behind a whitish residue, corresponding to ≈ 70% of the original sample weight, with size comparable to that of the original sample, consistent with the results from TGA. In comparison, only 11% char residue is obtained for FR-PU sponge after the MCC Method A test (Table 2.2). When the samples are subjected to MCC test following Method B (viz. in an aerobic environment), the pHRR is shifted to lower T_p and time (Figure 2.7 a-b). Here too, the test is performed in triplicate for each sample and average values for the results are reported in Table 2.3. We note that in this experiment, we observe an additional peak between 560- 570 °C in the HRR for FR-PU and for the control sponge. We attribute this peak to the decomposition of the char barrier in the presence of oxygen in the pyrolysis chamber. During anaerobic combustion (Method A), this char is preserved after the MCC experiment. As a consequence, we note that the char yield for FR-PU in Method B is reduced to ≈ 1% (compare with ≈ 11% in Method A). For S10, an

additional peak appears at 595 °C in the HRR in the MCC Method B experiment. However, only a small (2%) decrease in char yield is observed. For S10, we observe a pHRR of 44 W/g at 242 °C, a reduction of about 80-90% compared with FR-PU and the control sponge (Table 2.3). The A-HR capacity for S10 in Method B is lower than in Method A. Thus, the exceptional fire retardant performance of S10 is apparent, independent of the test conditions.

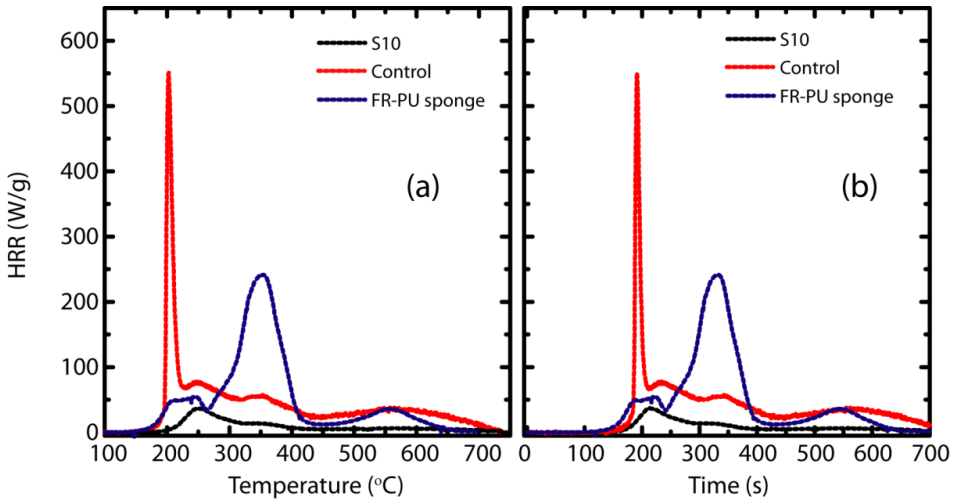

Figure 2.7 HRR curves as a function of (a) temperature, and (b) time for sponges by micro combustion calorimetry (MCC- Method B) test.

Heat, fuel, oxygen and a chemical chain reaction constitute the four elements leading to sustained fire. Abatement of fire necessitates inhibition or elimination of one of these elements from the fire tetrahedron. Most flame retardants for polymeric materials and PU foams in specific are designed to inhibit the pyrolysis of polymer by scavenging radicals (gas phase) or form a solid protective char layer that acts as a heat and mass barrier between the flame and burning material (condensed phase). The flame retardant is usually added during foam processing or post foam processing, often replacing bulk of the polymer and compromising mechanical properties. Quite atypically, these hybrid foams have been constructed from inherently non-flammable materials without compromising mechanical properties. This unique approach renders self-extinguishing characteristics to the foam and with very less ignitable content the foams release less smoke or toxic gases during burning.

Table 2.3: MCC results for control, composite and FR-PU sponges following Method B. The samples were tested in triplicate and the values of measured parameters are averaged.

Samples	T_p (°C)	A-pHRR(W/g) (% reduction	A-THR (kJ/g) (% reduction	A-HR Capacity (J/g-K)	% Char residue
Control	199±4	578±26	27±1	663±23	0
S10	242±6	44±8 (92.3, 79.2)	7±1 (75.2, 77.0)	51±10	67.76
FR-PU sponge	362±5	217±22	29±1	250±20	1.14

2.4.6 Scale up

The fire retardant performance of the ice templated composite sponges is a consequence of their composition and microstructure. These sponges comprise predominantly inorganic components. We have presented data for composite sponges prepared by ice templating a dispersion of silica particles. However, the ice templating method can be used to prepare sponges from other inorganic particulates as well. Here, we demonstrate that fire retardant sponges can be prepared using inexpensive calcium carbonate colloidal particles, and that the ice-templating method is amenable to a 100-fold scale-up based on sample volume, without loss in fire retardant or mechanical properties. We ice-template aqueous dispersions of calcium carbonate nanoparticles (average particle size ≈ 500 nm, zeta potential -30 mV; Figure 2.8), PEI and diepoxy cross-linker. We note that ice-templating 0.6 ml dispersions of these in 8 mm plastic tubes (as for the silica dispersions) results in the formation of elastic macroporous sponges, that have similar mechanical response as S10. We attempted the synthesis of larger sponges by ice templating 60 ml aqueous dispersions comprising 6 gm calcium carbonate nanoparticles, 500 mg PEI and 400 mg cross-linker. Our initial attempts in scaling up the size of the sponges by ice-templating a 60 ml colloidal dispersion were unsuccessful. The key constraint in scaling up the ice-templating method to prepare elastic sponges arise from heat transfer limitations during the freezing process. A container with the colloidal dispersion was placed in the freezer at -10 °C and heat transfer through the walls of

the container resulted in freezing of the dispersion. This resulted in the formation of sheet-like ice crystals and the sponges so obtained were characterized by thick parallel walls, rather than the cellular architecture observed for the sponges described in the earlier sections (that were prepared using 0.6 ml dispersions).

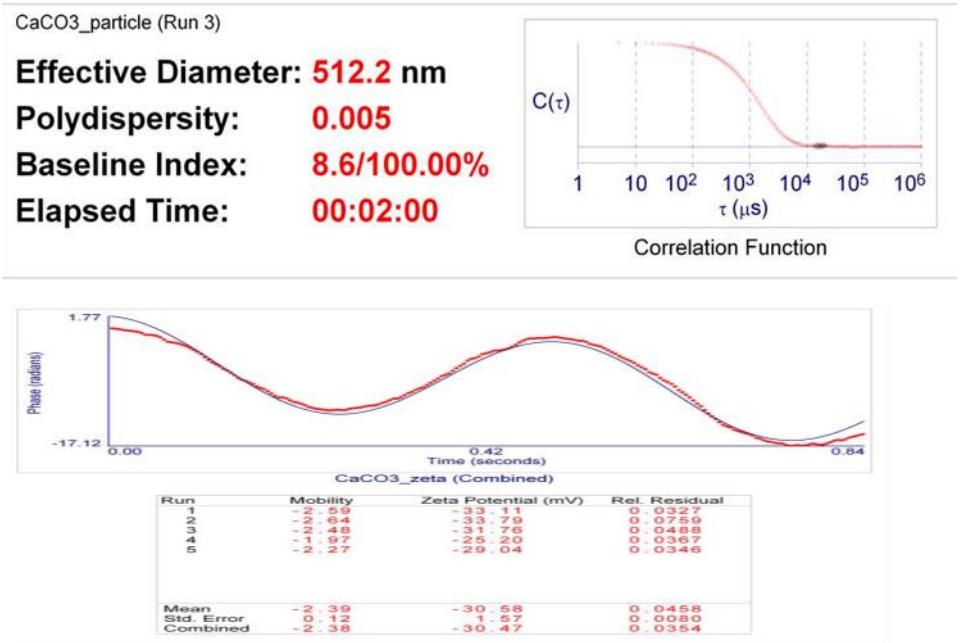

Figure 2.8 Characterization of $CaCO_3$ particle using dynamic light scattering (DLS) and zeta potential.

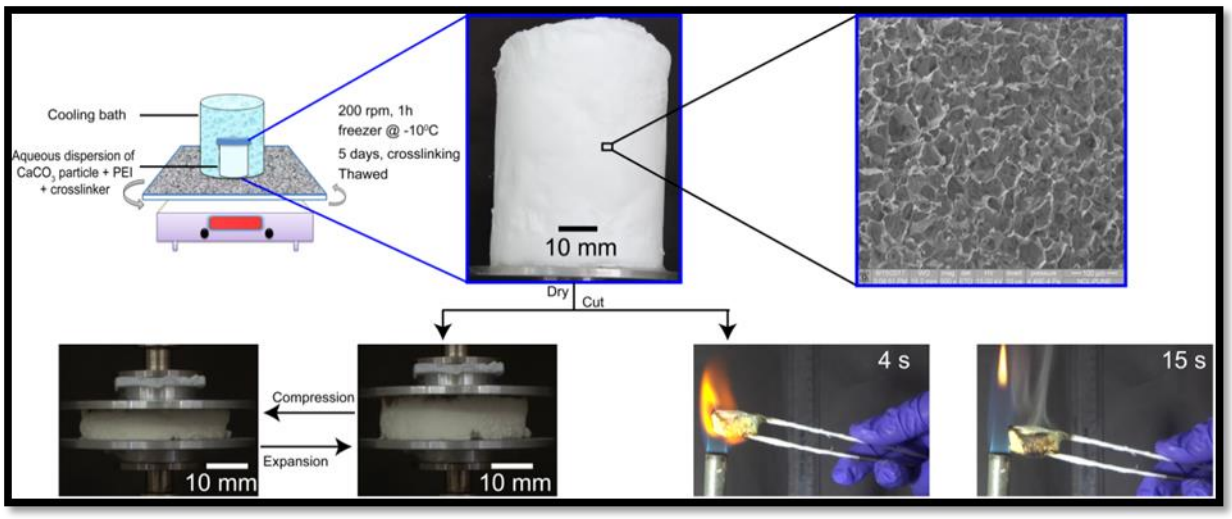

Figure 2.9 Preparation of large scaled-up sponge, its microstructure; mechanical recovery and flame retardant behavior in a torch burn test.

These scaled-up sponges were brittle and failed on compression to modest strains. Therefore, in a modified process, we froze the 60 ml dispersion while continuously agitating the container using a mechanical shaker that allowed us to precisely control rotation speed. We froze the dispersion by placing it in an ice bath and placing the entire assembly on a mechanical shaker whose speed was set at 200 rpm. The cross-linker was dropwise added while agitating the mixture and mechanical shaking was continued for next 1 hour, until the entire sample was frozen (Figure 2.9). The frozen sample was then placed inside a -10 ^{0}C freezer for 5 days during which the polymer is cross-linked. After 5 days, the sponge was thawed at room temperature for a day. This results in the preparation of a large sponge, with 100-fold larger volume compared to the silica based sponges, S5 and S10 (Figure 2.9). We have characterized the mechanical response of this sponge in the dry state (Figure 2.9) and note that it exhibits elastic recovery after large compressive deformation. SEM indicates that these sponges are characterized by a cellular microstructure, similar to those for S10 (Figure 2.9). Finally, we investigated the performance of this sample when subjected to a torch burn test. These samples exhibit flame retardance that is comparable to the S10. This is not surprising since these sponges comprise predominantly calcium carbonate, and therefore, it is only the minor organic component, the cross-linked polymer that can catch fire on exposure to a flame. This demonstrates that it is possible to prepare elastic sponges using dispersions of different inorganic particles and that these sponges exhibit exceptional fire retardant properties.

2.5 Conclusions

We demonstrate that ice-templated hybrid foams exhibit a desirable combination of properties: (i) they have a tunable elastic modulus and are mechanically robust, with low compression set and; (ii) they have exceptional fire retardant properties since they are predominantly inorganic. These hybrid foams do not contain any fire retardant additive and are synthesized from environmentally benign constituents. They are prepared by freezing an aqueous dispersion of inorganic colloids, cross-linkable polymer (polyethyleneimine, PEI) and diepoxy cross-linker, and by allowing the polymer to crosslink around the inorganic colloids in the frozen state. This protocol results in foams that are elastic and that can recover their shape after compression, despite being comprised largely of inorganic particles (> 85% by weight). We demonstrate that ice-templating can be used to prepare foams using different inorganic colloids, such as silica and calcium carbonate. We also demonstrate 100-fold scale

up of foam synthesis, by shaking the dispersion during the freezing process to ensure uniform heat transfer. There is no compromise in mechanical properties and fire retardant characteristics of the scaled-up sponges. Ice-templated hybrid foams show low compression set, and recover their original size after compression is released. The kinetics of shape recovery depends on the volume fraction of the ice-templated dispersion, ϕ. The higher the volume fraction of colloids and polymer, the slower the recovery. The modulus of the foam also depends on ϕ, and increases linearly with ϕ. Thus, the modulus and kinetics of foam recovery from compression can be tuned by adjusting ϕ during foam synthesis. When subjected to a torch burn test, the hybrid foams catch fire, but the flame does not spread and is self-extinguished. The foam structure does not collapse, due to the inorganic framework. Microscale combustion calorimetry, using both Method A (combustion in nitrogen) and Method B (combustion in 20/80 oxygen/nitrogen mixture) shows that the hybrid foams show > 75% decrease in peak heat release rate relative to commercial fire retardant polyurethane sponges. Our results have important implications for foam applications in furniture, upholstery and automotive, airline or auditorium seating applications.

2.6 References

(1) Flambard, X.; Bourbigot, S.; Kozlowski, R.; Muzyczek, M. .; Mieleniak, B.; Ferreira, M.; Vermeulen, B.; Poutch, F. Progress in Safety, Flame Retardant Textiles and Flexible Fire Barriers for Seats in Transportation. *Polym. Degrad. Stab.* **2005**, *88*, 98–105.

(2) Kozlowski, R.; Mieleniak, B.; Muzyczek, M.Fire Resistant Composites for Upholstery. *Polym. Degrad. Stab.* **1999**, *64*, 511–515.

(3) Chemical Economics Handbook: Polyurethane Foams, *HIS Markit*, **2016**.

(4) Cao, L.; Chen, D.; Li, W.; Caruso, R. A. Hierarchically Porous Titania Networks with Tunable Anatase:Rutile Ratios and Their Enhanced Photocatalytic Activities. *ACS*

Appl. Mater. Interfaces **2014**, *6*, 13129–13137.

(5) McCoy, M. To sleep, perchance on foam. Advances in polyurethane chemistry are helping revolutionize the mattress industry. *C&EN* **2017**, *95*, 20-21.

(6) Aou, K.; Schrock, A.K.; Baugh, D.; Gamboa, R.R.; Ulmer, L.C. Viscoelastic Recovery Behavior and Imperfection in Reactive Polymer Network of Viscoelastic Polyurethane Memory Foams. *Polymer.* **2017**, *117*, 183–197.

(7) Specification for resistance to ignition of mattresses, mattress pads, divans and bed bases. British standards BS 7177:**2008**+A1:**2011.**

(8) de Wit, C. A. An Overview of Brominated Flame Retardants in the Environment. *Chemosphere* **2002**, *46*, 583–624.

(9) Alaee, M.; Arias, P.; Sjödin, A.; Bergman, Å. An Overview of Commercially Used Brominated Flame Retardants, Their Applications, Their Use Patterns in Different Countries/regions and Possible Modes of Release. *Environ. Int.* **2003**, *29*, 683–689.

(10) Birnbaum, L. S.; Staskal, D. F. Brominated Flame Retardants: Cause for Concern? *Environ. Health Perspect.* **2004**, *112*, 9–17.

(11) Iqbal, M.; Syed, J. H.; Katsoyiannis, A.; Malik, R. N.; Farooqi, A.; Butt, A.; Li, J.; Zhang, G.; Cincinelli, A.; Jones, K. C. Legacy and Emerging Flame Retardants (FRs) in the Freshwater Ecosystem: A Review. *Environ. Res.* **2017**, *152*, 26–42.

(12) Salamova, A.; Hermanson, M. H.; Hites, R. A. Organophosphate and Halogenated Flame Retardants in Atmospheric Particles from a European Arctic Site. *Environ. Sci. Technol.* **2014**, *48*, 6133–6140.

(13) Camarasa, J. G.; Serra-Baldrich, E. Allergic Contact Dermatitis from Triphenyl Phosphate. *Contact Dermatitis* **1992**, *26*, 264–265.

(14) Castro-Jiménez, J.; Berrojalbiz, N.; Pizarro, M.; Dachs, J. Organophosphate Ester (OPE) Flame Retardants and Plasticizers in the Open Mediterranean and Black Seas Atmosphere. *Environ. Sci. Technol.* **2014**, *48*, 3203–3209.

(15) Möller, A.; Sturm, R.; Xie, Z.; Cai, M.; He, J.; Ebinghaus, R. Organophosphorus Flame Retardants and Plasticizers in Airborne Particles over the Northern Pacific and

Indian Ocean toward the Polar Regions: Evidence for Global Occurrence. *Environ. Sci. Technol.* **2012**, *46*, 3127–3134.

(16) Ma, Y.; Xie, Z.; Lohmann, R.; Mi, W.; Gao, G. Organophosphate Ester Flame Retardants and Plasticizers in Ocean Sediments from the North Pacific to the Arctic Ocean. *Environ. Sci. Technol.* **2017**, *51*, 3809–3815.

(17) Costes, L.; Laoutid, F.; Brohez, S.; Dubois, P. Bio-Based Flame Retardants: When Nature Meets Fire Protection. *Mater. Sci. Eng. R Reports* **2017**, *117*, 1–25.

(18) Kumar, S. K.; Benicewicz, B. C.; Vaia, R. A.; Winey, K. I. *50th Anniversary Perspective* : Are Polymer Nanocomposites Practical for Applications? *Macromolecules* **2017**, *50*, 714–731.

(19) Morgan, A. B.; Wilkie, C. A. Flame Retardant Polymer Nanocomposites; Wiley-Interscience, 2007 (ISBN: 978-0-471-73426-0).

(20) Bourbigot, S.; Turf, T.; Bellayer, S.; Duquesne, S. Polyhedral Oligomeric Silsesquioxane as Flame Retardant for Thermoplastic Polyurethane. *Polym. Degrad. Stab.* **2009**, *94*, 1230–1237.

(21) Gilman, J. Flammability and Thermal Stability Studies of Polymer Layered-Silicate (Clay) Nanocomposites. *Appl. Clay Sci.* **1999**, *15*, 31–49.

(22) Xie, H.; Yang, W.; Yuen, A. C. Y.; Xie, C.; Xie, J.; Lu, H.; Yeoh, G. H. Study on Flame Retarded Flexible Polyurethane Foam/alumina Aerogel Composites with Improved Fire Safety. *Chem. Eng. J.* **2017**, *311*, 310–317.

(23) Laoutid, F.; Bonnaud, L.; Alexandre, M.; Lopez-Cuesta, J.-M.; Dubois, P. New Prospects in Flame Retardant Polymer Materials: From Fundamentals to Nanocomposites. *Mater. Sci. Eng. R Reports* **2009**, *63*, 100–125.

(24) Ding, Z.; Li, Y.; He, M.; Wang, W.; Wang, C. The Combination of Expandable Graphite, Organic Montmorillonite, and Magnesium Hydrate as Fire-Retardant Additives for Ethylene-Propylene-Diene Monomer/chloroprene Rubber Foams. *J. Appl. Polym. Sci.* **2017**, *134*, 44929.

(25) Cao, X.; James Lee, L.; Widya, T.; Macosko, C. Polyurethane/clay Nanocomposites Foams: Processing, Structure and Properties. *Polymer.* **2005**, *46*, 775–783.

(26) Liff, S. M.; Kumar, N.; McKinley, G. H. High-Performance Elastomeric Nanocomposites via Solvent-Exchange Processing. *Nat. Mater.* **2007**, *6*, 76–83.

(27) Kashiwagi, T.; Du, F.; Douglas, J. F.; Winey, K. I.; Harris, R. H.; Shields, J. R. Nanoparticle Networks Reduce the Flammability of Polymer Nanocomposites. *Nat. Mater.* **2005**, *4*, 928–933.

(28) Li, J.; Srivastava, S.; Ok, J. G.; Zhang, Y.; Bedewy, M.; Kotov, N. A.; Hart, A. J. Multidirectional Hierarchical Nanocomposites Made by Carbon Nanotube Growth within Layer-by-Layer-Assembled Films. *Chem. Mater.* **2011**, *23*, 1023–1031.

(29) Wicklein, B.; Kocjan, A.; Salazar-Alvarez, G.; Carosio, F.; Camino, G.; Antonietti, M.; Bergström, L. Thermally Insulating and Fire-Retardant Lightweight Anisotropic Foams Based on Nanocellulose and Graphene Oxide. *Nat. Nanotechnol.* **2014**, *10*, 277–283.

(30) Nine, M. J.; Tran, D. N. H.; Tung, T. T.; Kabiri, S.; Losic, D. Graphene-Borate as an Efficient Fire Retardant for Cellulosic Materials with Multiple and Synergetic Modes of Action. *ACS Appl. Mater. Interfaces* **2017**, *9*, 10160–10168.

(31) Lorenzetti, A.; Dittrich, B.; Schartel, B.; Roso, M.; Modesti, M. Expandable Graphite in Polyurethane Foams: The Effect of Expansion Volume and Intercalants on Flame Retardancy. *J. Appl. Polym. Sci.* **2017**, *134*, 45173.

(32) Li, Y.-C.; Schulz, J.; Mannen, S.; Delhom, C.; Condon, B.; Chang, S.; Zammarano, M.; Grunlan, J. C. Flame Retardant Behavior of Polyelectrolyte–Clay Thin Film Assemblies on Cotton Fabric. *ACS Nano* **2010**, *4*, 3325–3337.

(33) Pan, H.; Pan, Y.; Wang, W.; Song, L.; Hu, Y.; Liew, K. M. Synergistic Effect of Layer-by-Layer Assembled Thin Films Based on Clay and Carbon Nanotubes To Reduce the Flammability of Flexible Polyurethane Foam. *Ind. Eng. Chem. Res.* **2014**, *53*, 14315–14321.

(34) Li, Y.-C.; Kim, Y. S.; Shields, J.; Davis, R.; Wilson, M. A.; Lamb, R. N.; Yoo, P. J.; Qi, Y.; Hart, A. J.; Hammond, P. T.; Kotov, N. A. Controlling Polyurethane Foam Flammability and Mechanical Behaviour by Tailoring the Composition of Clay-Based Multilayer Nanocoatings. *J. Mater. Chem. A* **2013**, *1*, 12987.

(35) Pan, H.; Wang, W.; Pan, Y.; Song, L.; Hu, Y.; Liew, K. M. Formation of Self-Extinguishing Flame Retardant Biobased Coating on Cotton Fabrics via Layer-by-Layer Assembly of Chitin Derivatives. *Carbohydr. Polym.* **2015**, *115*, 516–524.

(36) Kim, Y. S.; Davis, R.; Cain, A. A.; Grunlan, J. C. Development of Layer-by-Layer Assembled Carbon Nanofiber-Filled Coatings to Reduce Polyurethane Foam Flammability. *Polymer.* **2011**, *52*, 2847–2855.

(37) Sun, H.; Schiraldi, D. A.; Chen, D.; Wang, D.; Sánchez-Soto, M. Tough Polymer Aerogels Incorporating a Conformal Inorganic Coating for Low Flammability and Durable Hydrophobicity. *ACS Appl. Mater. Interfaces* **2016**, *8*, 13051–13057.

(38) Deville, S. Ice-templating, freeze casting: Beyond materials processing. J. Mater. Res. 2013,28, 2202-2219.

(39) Gutiérrez, M. C.; Ferrer, M. L.; del Monte, F. Ice-Templated Materials: Sophisticated Structures Exhibiting Enhanced Functionalities Obtained after Unidirectional Freezing and Ice-Segregation-Induced Self-Assembly. *Chem. Mater.* **2008**, *20*, 634–648.

(40) Leventis, N.; Chidambareswarapattar, C.; Bang, A.; Sotiriou-Leventis, C. Cocoon-in-Web-Like Superhydrophobic Aerogels from Hydrophilic Polyurea and Use in Environmental Remediation. *ACS Appl. Mater. Interfaces* **2014**, *6*, 6872–6882.

(41) Cho, J. H.; Vasagar, V.; Shanmuganathan, K.; Jones, A. R.; Nazarenko, S.; Ellison, C. J. Bioinspired Catecholic Flame Retardant Nanocoating for Flexible Polyurethane Foams. *Chem. Mater.* **2015**, *27*, 6784–6790.

(42) Cain, A. A.; Plummer, M. G. B.; Murray, S. E.; Bolling, L.; Regev, O.; Grunlan, J. C. Iron-Containing, High Aspect Ratio Clay as Nanoarmor That Imparts Substantial Thermal/flame Protection to Polyurethane with a Single Electrostatically-Deposited Bilayer. *J. Mater. Chem. A* **2014**, *2*, 17609–17617.

(43) Rajamanickam, R.; Kumari, S.; Kumar, D.; Ghosh, S.; Kim, J. C.; Tae, G.; Sen Gupta, S.; Kumaraswamy, G. Soft Colloidal Scaffolds Capable of Elastic Recovery after Large Compressive Strains. *Chem. Mater.* **2014**, *26*, 5161–5168.

(44) U.S. Government Publishing Office. Flammability of interior materials, *Code of Federal Regulations (annual edition)*, 36 FR 22902, Dec. 2, 1971, as amended at 40

FR 14319, Mar. 31, **1975**.

(45) Suresh, K.; Patil S.; Rajamohanan P. Ramanpillai; Kumaraswamy, G. The Template Determines Whether Chemically Identical Nanoparticle Scaffolds Show Elastic Recovery or Plastic Failure. *Langmuir*. **2016**, *32*, 11623-11630.

(46) Suresh, K.; Sharma, D.; Chulliyil, R.; Sarode, K.; Kumar, R.; Chowdhury, A.; Kumaraswamy, G. Single-Particle Tracking To Probe the Local Environment in Ice-Templated Crosslinked Colloidal Assemblies. *Langmuir*. **2018**, *15*, 4603-4613.

(47) Trovati, G.; Sanches, E. A.; Neto, S. C.; Mascarenhas, Y. P.; Chierice, G. O. Characterization of Polyurethane Resins by FTIR, TGA, and XRD. *J. Appl. Polym. Sci.* **2010**, *115*, 263–268.

(48) Babrauskas, V.; Peacock, R. D. Heat Release Rate: The Single Most Important Variable in Fire Hazard. *Fire Saf. J.* **1992**, 18, 255-272.

Elastic Compressible Energy Storage Devices from Ice Templated Polymer Gels treated with Polyphenols

Design and fabrication of rechargeable energy storage devices that are robust to mechanical deformation is essential for wearable electronics. In this chapter we report the preparation of compressible supercapacitors that retain their specific capacitance after large compression and that recover elastically after at least a hundred compression-expansion cycles. Compressible supercapacitors are prepared using a facile, scalable method that readily yields centimeter-scale macroporous objects. We ice template a solution of polyethyleneimine in green tea extract to prepare a macroporous crosslinked polymer gel (PG) whose walls are impregnated with green tea derived polyphenols. As the PG is insulating, we impart conductivity by deposition of gold on it. Gold deposition is done in two steps: first, silver nanoparticles are formed on the PG walls by in-situ reduction by polyphenols and then gold films are deposited on these walls. Gold coated PGs (GPGs) were used as electrodes to deposit poly(3,4-ethylenedioxythiophene) as a pseudocapacitive material. The specific capacitance of PEDOT coated GPGs (PGPG) was found to be 253 F/g at 1 A/g. PGPG could be subjected to over a hundred compression/expansion cycles without any mechanical failure or loss of capacitative performance. The capacitance was found to be 243 F/g upon compressing the device to 25% of its original size (viz. compressive strain = 75%). Thus, even large compression does not affect the device performance. This device shows power and energy densities of 2715 W/kg and 22 Wh/kg, respectively, in the uncompressed state. The macroporous nature of PGPG makes it possible to fill the PGPG pores with gel electrolyte. We report that the gel electrolyte filled supercapacitor exhibited a specific capacitance of 200 F/g, that increased by 4 % upon 75 % compression.

3.1 Introduction

A major challenge in the development of wearable electronics is the availability of compact, rechargeable energy storage devices that are resistant to mechanical fatigue (viz. to several cycles of deformation and release).[1–7] Ideally, such energy sources need to have large charge storage capacity, be capable of rapid charging and discharging and should retain their energy storage capabilities over several charge/discharge cycles. For wearable applications, they also need to retain their mechanical integrity and energy storage functionality over several cycles of repeated mechanical deformation.[8–12] In this context, supercapacitors (SCs) represent an attractive possibility amongst the energy storage devices due to their high power density and rapid charging.[13–16] Recently, there has been considerable progress in the area of supercapacitors based on carbon nanotubes and graphene.[17–26] Material assemblies have been demonstrated that exhibit typical capacitance of several tens of F/g, with a few materials achieving values as high as 150 to 200 F/g.[27] However, preparing supercapacitors that have high charge storage capabilities and that are capable of retaining this functionality after sustaining several cycles of mechanical deformation remains challenging. SCs based on conjugated polymers, such as polyaniline[28], polythiophene and derivatives of polythiophene[29–32], are suitable candidates for fabrication of flexible SCs since such polymers are inherently flexible and conductive.[21,33–40] However, here, the polymer needs to be coated on a current collector (electrode) to fabricate the SCs.[23,41,42] The advantage of polymer flexibility is lost when one uses a rigid electrode. Compressible SCs (CSCs) have been successfully prepared by using conducting carbon-based materials as current collectors.[5] For example, a compressible supercapacitor based on a polyaniline-graphene composite with a maximum capacitance of 385 F/g has been reported.[43] In another approach, pyrrole was dissolved in water along with graphene oxide (GO) and the solution was used to prepare a sponge.[44] The pyrrole monomer acted as a reducing agent to convert the GO to graphene. However, in such materials, there is a possibility of reduction in the substrate conductivity due to the tendency of the graphene platelets to aggregate into graphitic stacks. In another approach, polymer-based sponges were rendered conductive by coating them with single walled carbon nanotubes (SWCNTs), and this substrate was subsequently coated with conjugated polymer to form a pseudocapacitive material.[5] Here, SWCNTs were dispersed in surfactant and the polymer sponges were dip coated to allow adsorption of the surfactant modified SWCNTs. In this approach, there are concerns about the long term performance of the CSC due to the presence of insulating surfactant and the possibility of aggregation of

CNTs. Compressible materials devices have been prepared using commercially available polymer sponges as substrates. The conductivity was imparted by coating the voids in the sponge by carbon materials that are dispersed in water using a dispersant. This approach is likely to encounter two problems, (i) the carbon may not penetrate and conformally coat the interiors of the sponge (ii) The graphene or CNTs tend to stack and segregate during the charge discharge cycles of the supercapacitors. To circumvent this issue, the conductor should be uniformly and conformally coated on the base substrate. Furthermore, the base substrates should be tolerant to mechanical fatigue over several thousand cycles.

A substrate for CSCs should have (i) compressibility without plastic yield over a large number of compression-expansion cycles, (ii) good electrical conductivity and (iii) large pores for deposition of pseudocapacitive material and to facilitate ion transport. Ideally, the substrate should also accommodate volume change of the pseudocapacitive material during charge-discharge cycling. Following the description of earlier chapter, we propose that ice templating[47–4950] can be employed to prepare elastic compressible macroporous sponge-like scaffolds using polymers or particle-polymer hybrids. These scaffolds exhibit complete elastic recovery over several hundred cycles of compression and expansion. Further, these scaffolds are characterized by pores that are several tens of microns in size, allowing easy diffusion of dissolved species through them. These sponges also afford easy customization of their properties, unlike commercial sponges. For example, their modulus can be varied over orders of magnitude, starting from very soft sponges with a modulus ~O (10 kPa), without compromising their elastic mechanical response. Further, amine groups on the sponge surface can be readily functionalized to tune their wettability and other properties.[46] Due to the flexible nature of the walls of the scaffold, we anticipate that they can accommodate volume changes of the pseudocapacitive materials. We also note that the ice templating process allows us to prepare sponges in arbitrary shapes as determined by the mold, and we have prepared sponges up to several centimeters in size. Considering these advantages, we envisioned ice templated polymer scaffolds (ITPSs) as suitable substrates to prepare CSCs. These scaffolds are insulators – hence conductivity must be imparted to use them as electrodes in CSCs. Das et al. previously reported a technique to render insulating substrates conducting.[51,52] In their work, they used polyphenols from green tea to diffuse into and adhere to the walls of silk cocoons.[52] The polyphenol coated surfaces reduce silver ions to metallic silver.[53,54] Subsequently, silver reduces gold ions to metallic gold, to form thin continuous conducting gold films that coat several layers of the cocoons. We envisioned that

this approach could be an effective way of converting insulating ice templated polymeric scaffolds into good electrical conductors, without the sponge losing its flexibility. Further, while the conductivity of graphene based conductive substrates decreases with time due to the aggregation of graphene sheets, this is unlikely to be a problem for flexible substrates that are rendered conducting by deposition of thin film of gold. Further, these gold coated scaffolds can be used as electrode to deposit a very stable conjugated polymer poly(3,4-ethylenedioxythiophene) (PEDOT)[55–57] as pseudocapacitive material for fabrication of CSCs. In this work, we demonstrate the preparation of CSCs and characterize their properties as a function of compression. We show that such CSCs have a specific capacitance of 253 F/g and that the CSCs properties are substantially retained during compression up to 100 repeated cycles of compression and expansion. Capacitance measurements reported in this chapter were carried out by our collaborators, Dr. Chayanika Das and Dr. K. Krishnamoorthy at CSIR-NCL.

3.2 Experimental

3.2.1 Materials:

Polyethylenimine (PEI, branched polymer with supplier specified molecular weight = 750 kDa), 1,4-butanediol diglycidyl ether, 3,4-ethylenedioxythiophene (EDOT), lithium perchlorate were obtained from Sigma Aldrich and were used as received. A commercial brand of green tea (Tetley Tea, India) was purchased from a local source and used as received. Silver nitrate ($AgNO_3$) was obtained from Rankem, India. Gold plating solution was purchased from Oromerse, USA. Distilled deionized water (conductivity 18.2 MΩ/cm) from a Millipore MilliQ unit was used as solvent to prepare ITPSs. Polyphenols (PP) were extracted by brewing green tea in hot water for 1 h. In a typical experiment, 480 µl of the tea extract, 12 mg PEI solution (200 mg/mL) and 10 mg 1,4-butanediol diglycidyl ether (cross-linker) was mixed and transferred into a plastic container. The dispersion was then immediately placed in a freezer maintained at a temperature of -15 °C for 24 h. During this period, cross linking reaction between the PEI and epoxy functionalities of the cross linker occurs, as reported in the previous chapters.[45,46] After 24 hours of crosslinking, the frozen gel was taken out from the freezer and allowed to defrost at room temperature. After defrosting, the gel was washed several times with water. The porous gel is termed as PG.

3.3 Characterization:

The morphology of the porous sponge was imaged using a Quanta 200 3D scanning electron microscope (SEM). Mechanical properties of the sponges were measured using a strain controlled rheometer equipped with a normal force transducer (RSA-III Dynamic Mechanical Analyzer, from TA Instruments, USA).Cyclic voltammetry (CV), cyclic charge–discharge (CCD) and electrochemical impedance spectroscopy (EIS) measurements were performed on Biologic electrochemistry instrument (SP-300, USA).

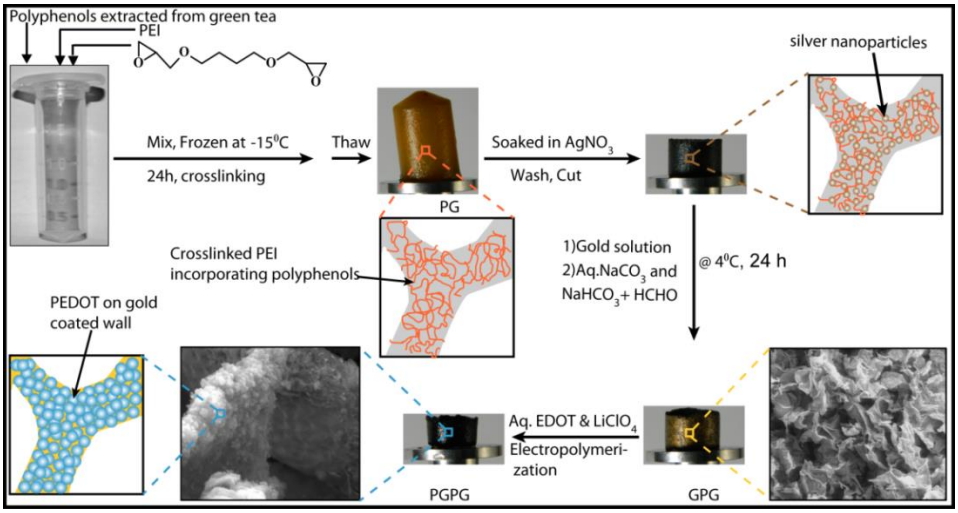

Figure 3.1: Schematic of preparation of the compressible supercapacitor. The polymeric gel (PG) is prepared by ice templating PEI and diepoxy in the presence of an aqueous solution of polyphenols extracted from green tea. Subsequently, silver nanoparticles are deposited on PG. The sponge after silver deposition is found to be non-conducting. Therefore, gold is deposited on the sponge walls to form a continuous gold coating that renders PG electrically conducting (that we term GPG). Finally, PEDOT is deposited by electropolymerization, using an aqueous solution of 10 mM EDOT and 100 mM lithium perchlorate ($LiClO_4$, as electrolyte). This compressible supercapacitor is termed PGPG.

3.4 Results and Discussion

We prepare a macroporous crosslinked polymer monolith by ice templating a solution of polyethyleneimine and 1,4-butanediol diglycidyl ether crosslinker in green tea extract, as described in the experimental section. Crosslinking the polymer in the frozen state allows us to recover the monolith simply by thawing, and we do not need to resort to freeze drying. Ice templating in the presence of green tea extract results in the walls of the monolith being impregnated with polyphenols derived from green tea. This as-prepared gel is termed PG.

PG is electrically insulating. Immersing PG in $AgNO_3$ solution for 2 h resulted in the deposition of silver nanoparticles on the amine groups that decorate the walls of PG (Figure 3.1). After two hours of immersion in $AgNO_3$ solution, the color of the PG turns faint brown indicating the formation of silver nanoparticles. On squeezing the PG, the silver nitrate solution is expelled from the pores. However, it is able to rapidly reabsorb the solution and expand when the strain is relaxed. We observe that repeated squeezing/expansion cycles when the PG is immersed in $AgNO_3$ solution helps formation of a uniform coating of silver nanoparticles on the PG walls. However, deposition of silver nanoparticles did not render the monolith electrically conducting. A conducting percolated network of silver nanoparticles could not be formed even after immersion in silver nitrate for a long time. It is known that only selective sites of polyphenol molecules can participate in the reduction of metal ions including Ag^+.[53] Since polyphenols are randomly incorporated in the sponge walls, growth and number density of Ag nanoparticles do not increase continuously with exposure time in solution. Therefore, a conducting percolated network of silver nanoparticles could not be formed even after immersion in silver nitrate solution for a long time. After deposition of silver nanoparticles, PG was thoroughly washed with water to remove residual silver ions. Next, the silver nanoparticle deposited PG was placed in gold plating solution (maintained at pH 10) for 24 h at 5°C (Figure 3.1). According to previous reports,[51,52] Ag nanoparticles reduce Au^+ to Au, and a continuous film of gold is deposited on the PG surface. PGs in gold solution were also periodically squeezed during this process to avoid pore blockage. It is not possible to gold plate PG directly, without deposition of silver nanoparticles. The presence of silver nanoparticles on the walls of the monolith is essential for reduction of Au^+ to Au. The gold plated monolith (termed GPG) was then washed multiple times with copious amount of hot water and was dried in a vacuum oven.

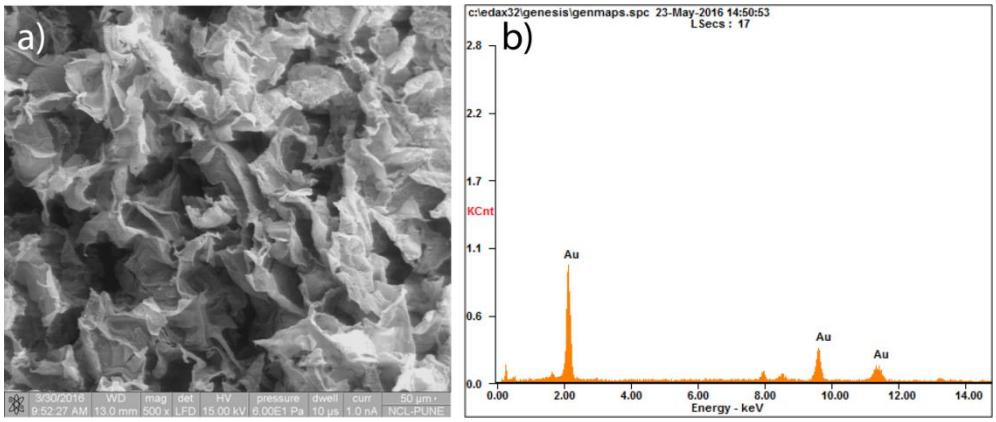

Figure 3.2: a) SEM image of gold deposited PG (GPG) and b) EDAX analysis of GPG.

We note that these gels are mechanically robust after gold plating and do not shrink significantly on drying. Deposition of gold on the GPG surface was confirmed using SEM and EDAX analysis (Figure 3.2). We measure the nominal density of polymer gels by weighing gels of known volume. These densities of the gels are found to be 0.04, 0.06, and 0.08 g/cm^3 for PG, after silver deposition and GPG respectively. The SEM images reveal large pores with size of the order of 100 µm bounded by thin walls (wall thickness ~ few microns) of the gold coated polymer scaffold. Only the walls of the porous sponge are gold coated – gold does not fill in and block the monolith pores. Gold coating renders the GPG electrically conducting, and we measure a resistance of about 6 Ω for GPG.

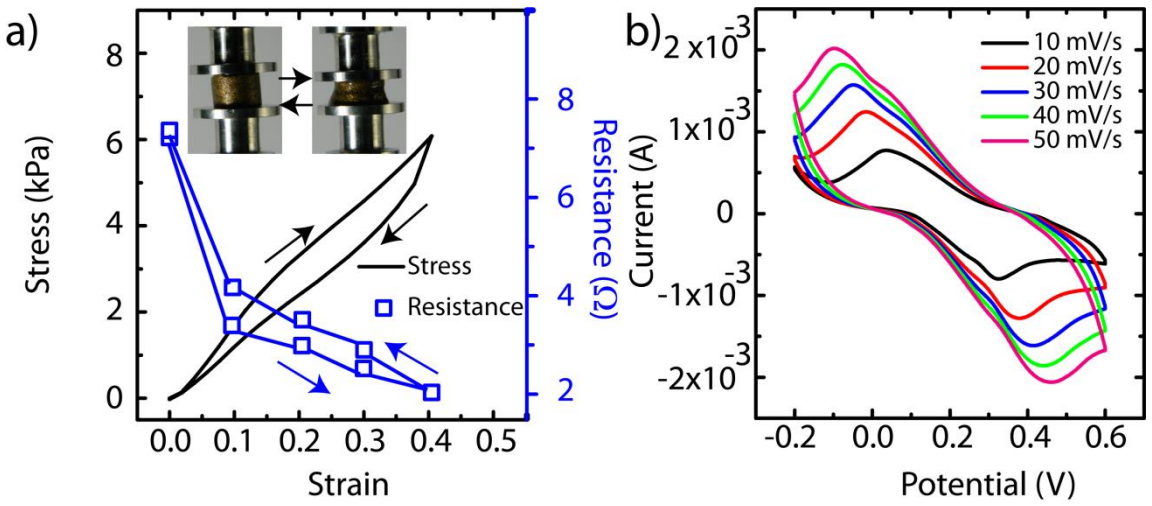

Figure 3.3: a) Stress-strain data (on left axis) for GPG and the corresponding electrical resistance (on the right axis) (the inset shows photographs of GPG during the compression-expansion cycle); b) CV of 1 mM ferrocenemethanol using GPG as working electrode.

Remarkably, GPG retains the flexibility of the original crosslinked polymer monoliths and recovers its shape even after large compressive deformation. On compression, there is a nonlinear increase in stress, typical of elastic foams (Figure 3.3a).[58] When the strain is released, there is hysteresis as the stress decays to zero. However, we note that there is almost complete recovery of the monolith after compression. The monolith is robust to repeated compression-expansion cycles and we present stress-strain data that shows that there is essentially no change in the mechanical response of the monolith over 100 cycles. On compression, the pores in the sponge collapse and the walls come into contact – correspondingly, there is a modest decrease in the electrical resistance to about 2 Ω (Figure 3.3a). The original resistance of the sponge is recovered when stress is released. We note that

repeated mechanical cycling (100 cycles of compression/re-expansion) do not change the overall resistance of the scaffolds. To understand the electrochemical activity of the GPG surface, CV of 1 mM (aq.) ferrocenemethanol was recorded at various scan rates (Figure 3.3b). Redox peaks of ferrocenemethanol indicate that the GPGs are conducting, thus confirming the formation of a continuous gold film on the GPG wall surface. We further plot peak current as a function of square root of scan rate and observe that this is linear (Figure 3.4). This confirms that the redox process is controlled by diffusion. From the peak current, the electroactive area was calculated and it was found to be 0.13 cm^2.

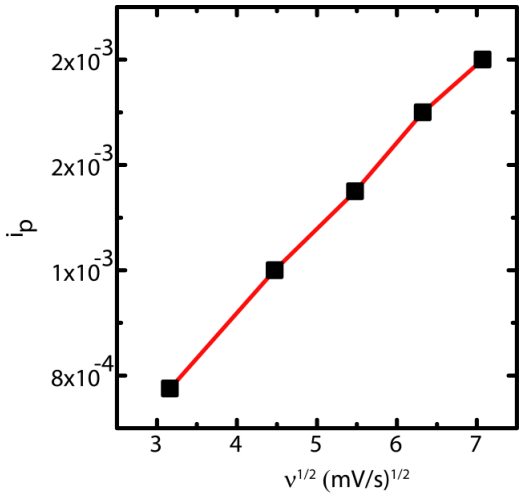

Figure 3.4: Plot of peak current density as a function of square root of scan rate.

We then proceeded to deposit PEDOT on GPG. PEDOT is a commercially exploited, stable conjugated polymer and a pseudocapacitive material. PEDOT can be deposited on various conducting surfaces by electrochemical polymerization of EDOT.[55–57] For deposition of PEDOT on GPG surface, GPG was attached to a button electrode using silver paste and immersed for 30 minutes in a 10 mM aqueous solution of EDOT containing 0.1 M lithium perchlorate. Here, lithium perchlorate acts as a supporting electrolyte. Electropolymerization of EDOT on GPG surface was performed in a standard 3-electrode configuration where GPG was the working electrode (WE), Pt-foil was used as counter electrode (CE) and Ag/AgCl was the reference electrode (RE). A constant potential of 1.3 V vs Ag/AgCl was applied during the polymerization process. We optimized the polymerization conditions and note that an optimal PEDOT thickness to achieve maximum capacitive performance of the PEDOT deposited GPG was obtained when polymerization was allowed to take place for 100 s. We term the sponge obtained by deposition of PEDOT on GPG as PGPG (Figure 3.1). PEDOT coating introduces roughness on the GPG surface. The morphology of the PEDOT coated

films is imaged using SEM (Figure 3.1) and shows characteristic polydisperse spheres of PEDOT (Figure 3.1).[59] Again, we note that deposition of PEDOT did not result in blockage of pores. We anticipate that the large pores in the composite sponge structure facilitate facile transport of ions through the PGPG. PEDOT undergoes volume change during the charge discharge process. We further anticipate that the presence of large macropores will help to accommodate PEDOT volume changes during the charge-discharge process. The PGPG was prepared in a cylindrical form (diameter ≈ 8 mm, length ≈ 5 mm) and was subjected to repeated compression/expansion cycles using a DMA, and nominal compressive stress (based on the initial cross sectional area) is reported as a function of compressive strain (Figure 3.5a).

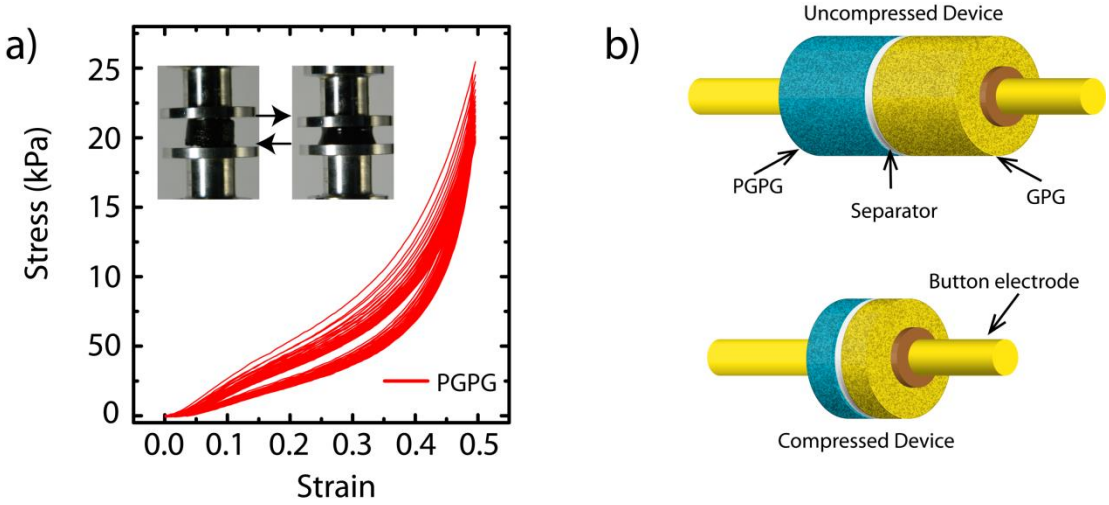

Figure 3.5: a) Stress-strain data over 100 compression/expansion cycles of PGPG saturated in electrolyte, $LiClO_4$ (the inset is pictorial demonstration of the process); b) Schematic representation of uncompressed and compressed device.

The cross-sectional area of the electrodes was approximately 50.3 mm^2. The electrodes were placed between two parallel plates (25 mm diameter) and were compressed up to 50 % of the initial unstrained height. To simulate the electrolyte-soaked working conditions of the electrode, DMA measurements were performed on electrodes saturated with water. When the electrodes are compressed, the water is squeezed out and there is an increase in stress. However, on release of compressive strain, the electrodes reabsorb the water and regain their initial dimensions, indicating elastic behavior. We performed 100 compression/expansion cycles repeatedly on PGPG and observe that there is no significant change in the stress-strain curves (Figure 3.5a). Thus, PGPG, with PEDOT deposited on the continuous gold film on the sponge surfaces, retains the elastic response characteristic of the original PG sponges and can

be reused after repeated compression to large strains. There is no decrease in stress after repeated compression cycles, indicating that there is no mechanical failure of the PGPGs during mechanical loading. Thus, the PGPG exhibit suitable mechanical performance for application as a CSC.

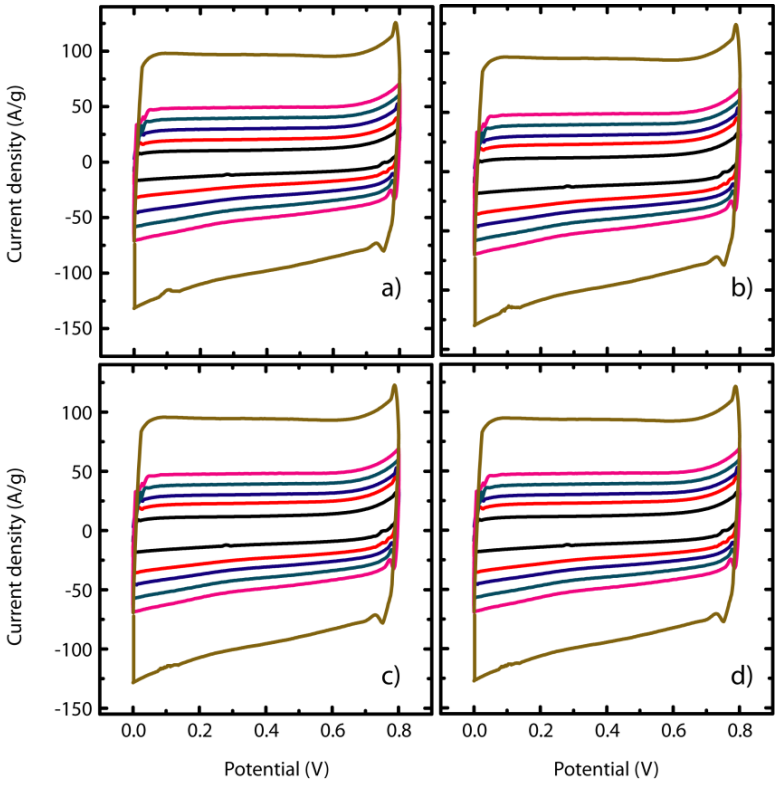

Figure 3.6: CVs recorded in liquid electrolyte at: a) uncompressed state, b) 25 % compression, c) 50 % compression and d) 75 % compression.

We have fabricated a two electrode device to study the redox performance of the PGPG at several compressions, where PGPG (WE) and GPG (CE) were pasted on gold button electrodes using silver paste. WE and CE were separated by a Celgard membrane (separator) (Figure 3.5b). This whole assembly was kept inside a graduated plastic tube, filled with electrolyte, which allowed us to control the compression. We note that all devices described here are unsymmetrical supercapacitors with PGPG as the working electrode and GPG as the counter electrode. Redox characteristics of PGPG were studied using CV at different strain: 0 %, 25 %, 50 % and 75 % respectively (Figure 3.6). Potential sweep between 0 to 0.8 V vs Ag/AgCl is employed for all CV measurements. Typical box type CVs of PEDOT were observed indicating capacitive behavior of the material for as prepared, undeformed PGPG (0 % strain).The capacitance was calculated to be 121 F/g at 10 mV/s. We then recorded CVs for PGPG compressed to 25 %, 50% and 75 % strain. The shape of the CVs did not change as

a function of strain. Further, the current density also remained constant independent of the strain (Figure 3.7). Thus, the capacitance of the electrodes is unaffected by the compressive strain. With this information in hand, we proceeded to fabricate CSCs. In one set of experiments, PGPG is used as working electrode with GPG as counter electrode, as discussed earlier. The electrolyte is 1 M $LiClO_4$. The charge discharge experiments were carried out between 0 and 0.8 V at various current densities (Figure 3.8).

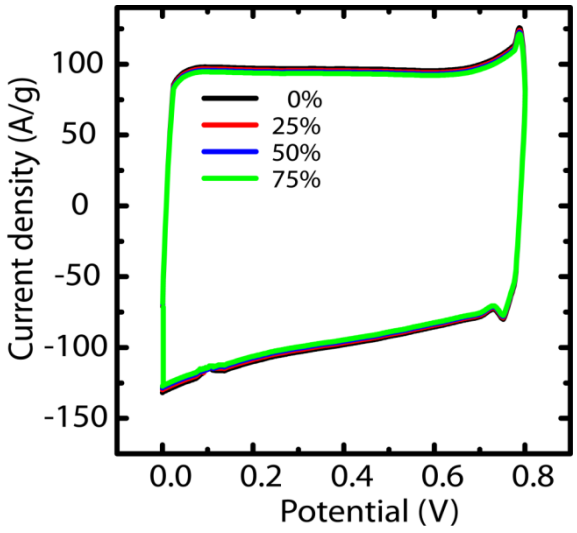

Figure 3.7: CV in 1 M $LiClO_4$ at 100 mV/s for 0 %, 25 %, 50 % and 75 % compression.

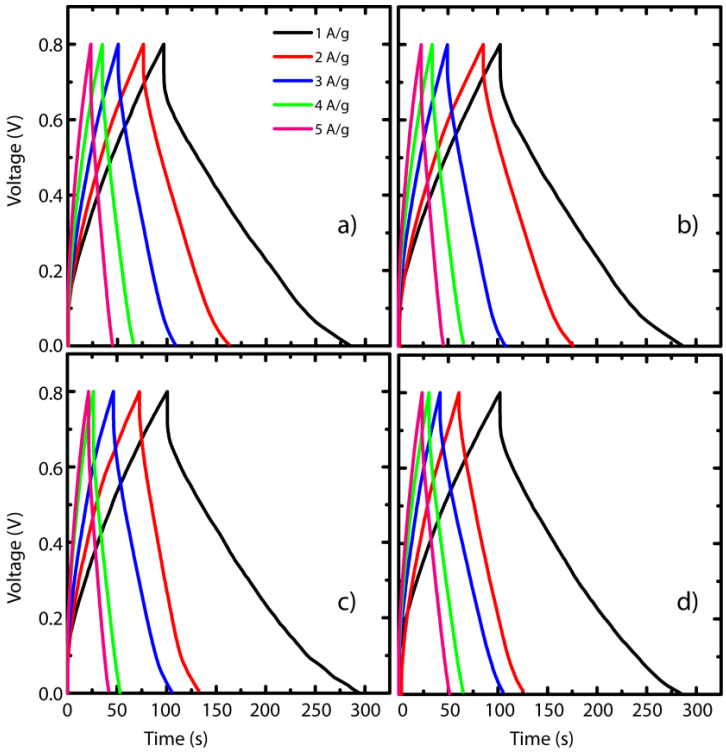

Figure 3.8: CCDs recorded in liquid electrolyte at: a) uncompressed state, b) 25 % compression, c) 50 % compression and d) 75 % compression.

PGPG showed unsymmetrical charge discharge profile, indicating increased IR drop. This resistance could be due to inherent lower conductivity of the electrochemically synthesized PEDOT. The capacitance of the uncompressed device was found to be 253 F/g (1 A/g). The capacitance decreased to 173 F/g when the charge discharge experiment was carried out at 5 A/g. This decrease is not unexpected in organic material based devices. We carried out charge discharge experiments at different current densities (1 A/g to 5 A/g) for PGPG compressed to different compressive strains (25 %, 50 % and 75 %). Remarkably, charge discharge curves of the PGPG are independent of the compressed state of the electrode, even for strains as large as 75 % for all current densities (representative data at a current density of 1 A/g is presented in Figure 3.9a).

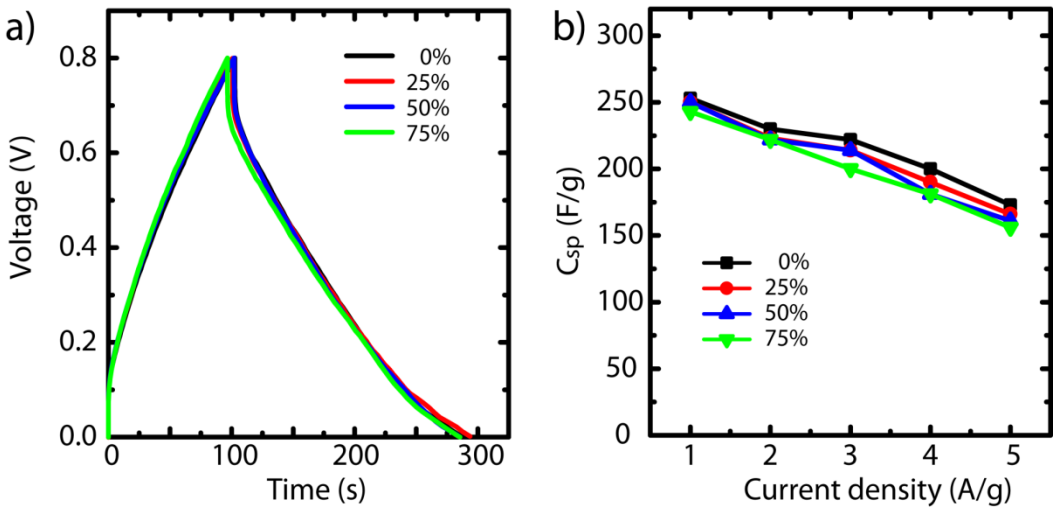

Figure 3.9: a) CCD in 1 M $LiClO_4$ at 1 A/g for 0%, 25 %, 50 % and 75 % compression; b) Calculated specific capacitances for 0%, 25 %, 50 % and 75 % at current densities of 1-5 A/g.

We calculated the capacitance for electrodes compressed to different strains and at different current densities and these device metrics are provided in Table 3.1. The charge discharge characteristics of PGPG are also unaffected by compressive strains up to 75 %. The highest specific capacitance (253 F/g) is measured for unstrained PGPG (0 % strain) at a current density of 1 A/g (Figure 3.9b, Table 3.1). There is a marginal decrease in capacitance on compression. For example, there is a ≈4 % decrease in capacitance on compression to 75 %, at a current density of 1 A/g, while the decrease in capacitance on compression to 75 % is ≈10 % at a high current density of 5 A/g. For use of CSCs in practical applications, it is important to study device performance over multiple compression and expansion cycles and over a large number of charge/discharge cycles. To study the effect of compression on the

performance of the devices, we mechanically compressed the PGPG device upto 50 % and held at that position while simultaneously measuring charge-discharge at 1 A/g current density. We then allow the electrode to relax and regain its original shape and then measure the charge/discharge characteristics in the relaxed state, viz. when there is no external force on the gel. We performed 100 compression–expansion cycles and recorded charge discharge at 0 % (Figure 3.10a) and at 50 % compressive strains (Figure 3.10b depicts data for 50 % compression at 1 A/g). Remarkably, we observe that all the charge discharge curves approximately overlap for PGPG in both compressed and unstrained states. Thus, the PGPG is mechanically elastic and there is no deterioration of its capacitative performance after multiple cycles of compression.

Table 3.1: Specific capacitances in liquid electrolyte at 0 %, 25 %, 50 % and 75 % compressions.

Current Density (A/g)	Capacitance measured in liquid electrolyte (F/g)			
	0 % compression	**25 % compression**	**50 % compression**	**75 % compression**
1	253	250	250	243
2	230	223	222	222
3	222	214	214	200
4	200	190	181	181
5	173	166	161	156

The impedance spectra of PGPG is recorded using the same experimental conditions as for capacitance measurements (Figure 3.10c for all compressions). Linearity of the Nyquist plot indicates diffusive mass transport. Resistance is calculated from the high frequency intercept of the semicircle. The resistance of the electrode is found to be 6 Ω. The variation in energy and power density of the flexible device under different compressions and at various current densities are also shown in a Ragone plot (Figure 3.10d, Table 3.2). The highest energy and power densities of 22 Wh/kg and 2715 W/kg, respectively are observed for unstrained PGPG. On compression of the PGPG to 50 %, a 5-6 % decrease in energy and power densities are observed. In next section, we describe the capacitative property of PGPG when the liquid electrolyte is replaced by a gel.

We describe the electrochemical measurements of the PGPG device containing gel electrolyte. To prepare the gel electrolyte, 1 g of PVA is added to 10 ml of water and the mixture is heated until a clear solution is formed. To this clear solution 1 M $LiClO_4$ is added. The heating is continued until the required consistency is achieved. In order to incorporate

the gel electrolyte, PGPG (pasted to a button electrode) is compressed and dipped in the gel electrolyte and kept for around 10 minutes. Then to ensure proper percolation of the gel electrolyte it is smeared on the scaffold with the help of a spatula. We note that the PVA concentration in the electrolyte gel is adjusted so as to obtain a material with a low yield stress (≈ 30 Pa,). We observe that the electrolyte gel yields and liquefies at the stresses experienced during the compression/expansion process. Also, PGPG is macroporous with pore size of the order of 100 μm. Therefore, we observe that the electrolyte gel is readily reabsorbed during the compression/expansion process. Finally, we note that there is no change in capacitance even after several cycles of compression/expansion for the gel electrolyte-filled macroporous PGPG, indicating that the gel electrolyte that is squeezed out during compression is reabsorbed by the PGPG during expansion.

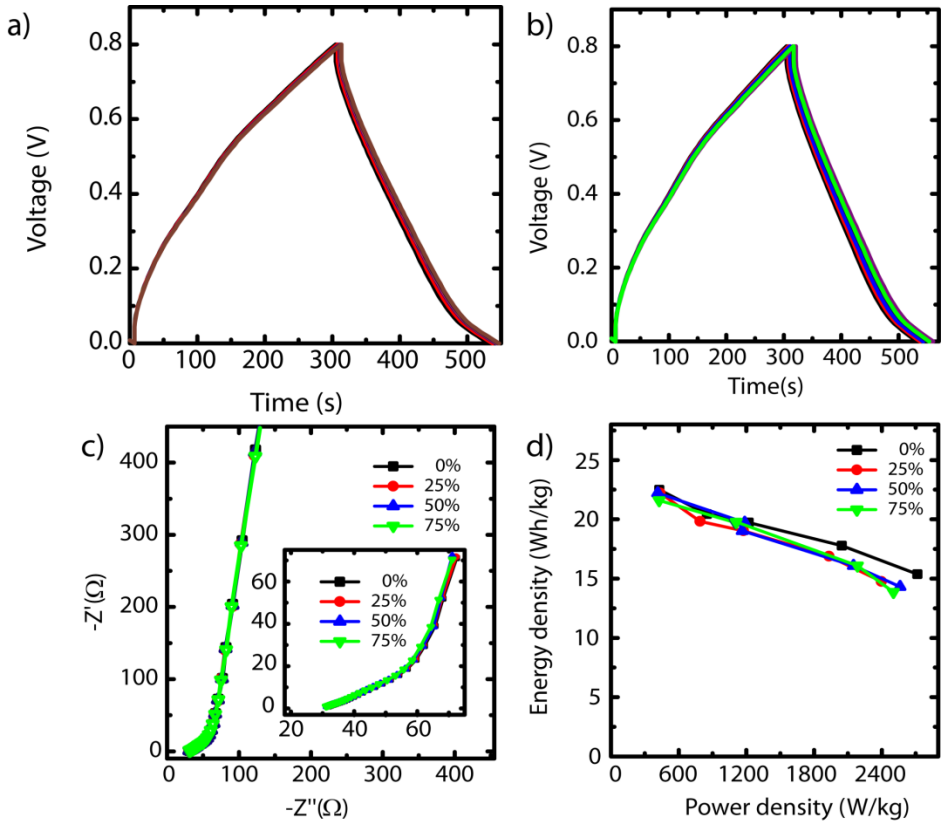

Figure 3.10: a) CCDs for uncompressed state at 1 A/g; b) 100 CCD cycles of 50 % compression at 1 A/g (every 10th cycle is shown); c) Nyquist plot for 0 %, 25 %, 50 % and 75 % compression and inset shows plot at high frequency; d) Ragone plot in liquid electrolyte.

We measure CV data using the same experimental setup as in the previous section. Here too, we obtain box type CV of PEDOT, indicating capacitive behavior of the PGPG containing

gel electrolyte (Figure 3.11). The capacitance was calculated to be 103 F/g at 10 mV/s. We recorded CVs at different compressive strains.

Table 3.2: Energy(Ed) and power (Pd) density for experiments in liquid electrolyte.

Current Density (A/g)	Ed (Wh/kg) 0%	Pd (W/kg) 0%	Ed (Wh/kg) 25%	Pd (W/kg) 25%	Ed (Wh/kg) 50%	Pd (W/kg) 50%	Ed (Wh/kg) 75%	Pd (W/kg) 75%
1	22	428	22	437	22	415	22	426
2	20	851	20	790	20	1186	20	1101
3	20	1221	19	1175	19	1164	18	1010
4	18	2046	17	1932	16	2148	16	1685
5	15	2715	15	2397	14	2561	14	1803

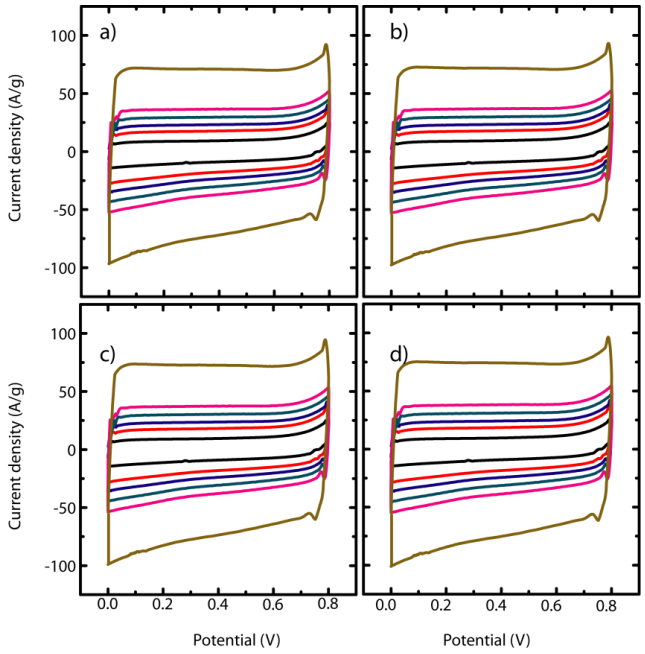

Figure 4.11: CVs recorded in gel electrolyte at: a) uncompressed state, b) 25 % compression, c) 50 % compression and d) 75 % compression.

As for the case of liquid electrolyte, the current density is independent of the compressive strain, up to 75 % strain (Figure 3.12a). Charge discharge experiments were carried for PGPG compressed to different strains and for different current densities. The capacitance of the device without compression was found to be 200 F/g (1 A/g). This decreased by 26 % upon increase in current density to 5 A/g. This decrease is 16 % more than that observed in liquid electrolyte. However, this is reasonable since we anticipate that the diffusion of ions in the gel electrolyte will be significantly slower as compared to liquid electrolyte. Then, we carried out charge discharge experiments at various compressive strains and at various current

densities. With gel electrolyte, we observe a strain dependence of the charge discharge profiles with compressive strains (Figure 3.12b). Electrodes compressed to strains of 50 % and 75 % exhibit faster charging characteristics relative to devices at 25 % and 0% compressive strains.

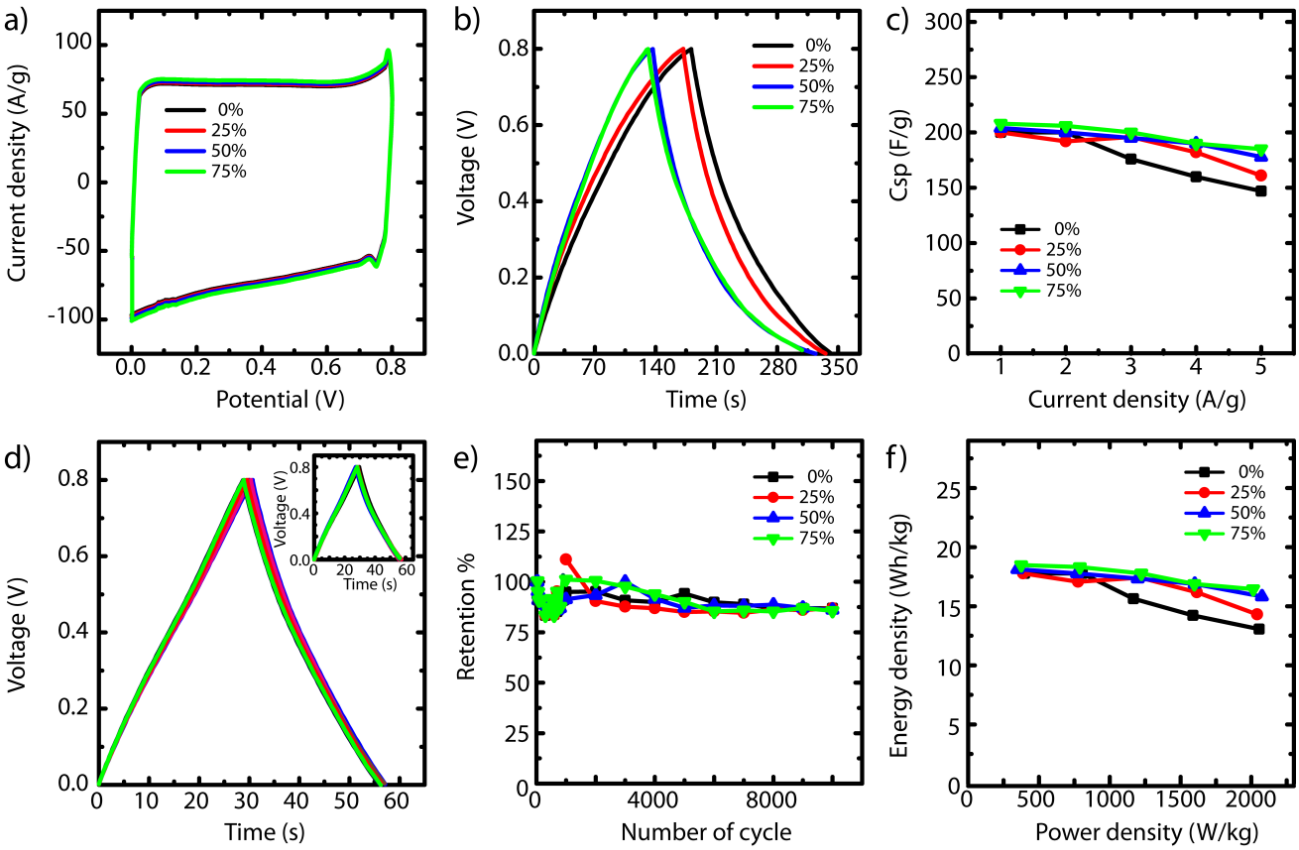

Figure 3.12: a) CV in gel electrolyte for 0 %, 25 %, 50 % and 75 % compressions at 100 mV/s ; b) CCD in gel electrolyte for 0 %, 25 %, 50 % and 75 % compressions at 1 A/g; c) Calculated specific capacitances for 0%, 25 %,50 % and 75 % at current densities 1-5 A/g; d) 100 CCD cycles at 5 A/g at 50 % compression and inset shows 100 CCD cycles at 0 % compression (every 10th cycle is shown); e) Retention after 10000 cycles; f) Ragone plot in gel electrolyte.

Furthermore, the capacitance calculated from the slope of discharge curve was found to decrease from electrodes compressed to 75 % to unstrained electrodes (strain = 0 %) (Figure 3.12c). Thus, the trend for PGPG containing gel electrolytes is opposite that for PGPG containing liquid electrolyte. We attribute this to better contact between gel electrolyte and PGPG at increased compressive strains. In the as prepared, uncompressed device, it is possible that the gel electrolyte may not have diffused and made contact with PEDOT on the walls of GPG. Upon compressing the device, the gel is squeezed and it is likely that the contact between the electrolyte gel and PGPG is improved. This would explain the increase in capacitance of the compressed devices. We note that the capacitance of device

compressed to 75 % and measured at 5 A/g current density (185 F/g) is 7 % higher than the capacitance of the uncompressed liquid electrolyte based device. We confirm that, just as with the electrode containing liquid electrolyte, the PGPG device containing electrolyte gel is mechanically elastic to large compressive strain and shows no deterioration in mechanical or capacitative performance even after 100 cycles of repeated compression-expansion (Figure 3.12d). We note that there is no change in the charge-discharge performance between the uncompressed state (Figure 3.12d, inset) and the compressed state (Figure 3d). The specific capacitance is virtually unchanged as a function of mechanical cycling. Further, we note that 86 % of the initial specific capacitance is retained even after 10000 charge discharge cycles, independent of the compressive strain that the electrode is subjected to (Figure 3.12e). From the Ragone plot (Figure 3.12f, Table 3.3), a maximum energy and power density of 18 Wh/kg and 2075 W/kg are observed, which suggests a marginal improvement in energy density relative to the PGPG containing liquid electrolyte. We reiterate that the highest specific capacitance and power density in this case (for the PGPG containing gel electrolyte) are observed for electrodes subjected to 75 % compressive strain, in contrast to the liquid electrolyte where optimum properties were obtained in the uncompressed state. Finally, we note that the balance of power and energy density for PGPG is intermediate to a battery and a conventional supercapacitor.

Table 3.3: Energy(Ed) and power (Pd) density for experiments in gel electrolyte.

Current Density (A/g)	Ed (Wh/kg) 0%	Pd (W/kg) 0%	Ed (Wh/kg) 25%	Pd (W/kg) 25%	Ed (Wh/kg) 50%	Pd (W/kg) 50%	Ed (Wh/kg) 75%	Pd (W/kg) 75%
1	18	399	18	389	18	348	18	374
2	18	807	17	776	18	770	18	790
3	16	1168	17	1214	17	1198	17	1224
4	14	1588	16	1616	17	1600	17	1598
5	13	2055	14	2041	16	2075	16	2013

3.5 Conclusions

Ice templated polymer gels (PGs) were prepared by crosslinking poly(ethylene imine) and diepoxides. The macroporous PGs were insulator and conductivity was imparted by electroless deposition of gold. Polyphenols extracted from green tea were used to reduce silver ions to silver nanoparticles. Subsequently, these nanoparticles reduced gold ions to gold, forming a continuous uniform film on the surface of the PG walls (GPGs). PEDOT was deposited on GPGs and they were used as one of the electrodes in supercapacitors. The PEDOT coated GPGs were mechanically stable over hundred compression-expansion cycles.

The uncompressed device exhibited a specific capacitance of 253 F/g, which decreased by 4 % upon 75 % compression while using liquid electrolyte. On the other hand, the specific capacitance increased upon compressing the device while using gel electrolyte. The increase has been attributed to better contact between the gel electrolyte and PEDOT upon compression. The power and energy density of the device were found to be 2075 W/kg and 18 Wh/kg, respectively. The variation in these parameters was insignificant as a function of compression expansion cycles as well as several thousand charge discharge experiments. Thus, these devices are robust and deliver impressive specific capacitance, power and energy.

3.6 References

(1) Rogers, J. A.; Someya, T.; Huang, Y. Materials and Mechanics for Stretchable Electronics. *Science* **2010**, *327*, 1603–1607.

(2) Liu, L.; Niu, Z. Unconventional Supercapacitors from Nanocarbon-Based Electrode Materials to Device Configurations. *Chem. Soc. Rev.* **2016**, *45*, 4340–4363.

(3) Nardecchia, S.; Carriazo, D.; Ferrer, M. L.; Gutiérrez, M. C.; del Monte, F.. Three Dimensional Macroporous Architectures and Aerogels Built of Carbon Nanotubes And/or Graphene: Synthesis and Applications. *Chem. Soc. Rev.* **2013**, *42*, 794–830.

(4) Dong, L.; Xu, C.; Li, Y.; Huang, Z.-H.; Kang, F.; Yang, Q.-H.; Zhao, X. Flexible Electrodes and Supercapacitors for Wearable Energy Storage: A Review by Category. *J. Mater. Chem. A* **2016**, *4*, 4659–4685.

(5) Niu, Z.; Zhou, W.; Chen, X.; Chen, J.; Xie, S. Highly Compressible and All-Solid-State Supercapacitors Based on Nanostructured Composite Sponge. *Adv. Mater.* **2015**, *27*, 6002–6008.

(6) Hu, H.; Zhao, Z.; Wan, W.; Gogotsi, Y.; Qiu, J. Ultralight and Highly Compressible Graphene Aerogels. *Adv. Mater.* **2013**, *25*, 2219–2223.

(7) Yu, Y.; Zeng, J.; Chen, C.; Xie, Z.; Guo, R.; Liu, Z.; Zhou, X.; Yang, Y.; Zheng, Z. Three-Dimensional Compressible and Stretchable Conductive Composites. *Adv. Mater.* **2014**, *26*, 810–815.

(8) Bao, L.; Li, X. Towards Textile Energy Storage from Cotton T-Shirts. *Adv. Mater.* **2012**, *24*, 3246–3252.

(9) Bao, L.; Zang, J.; Li, X. Flexible Zn_2SnO_4/MnO_2 Core/Shell Nanocable−Carbon

Microfiber Hybrid Composites for High-Performance Supercapacitor Electrodes. *Nano Lett.* **2011**, *11*, 1215–1220.

(10) Gao, Z.; Bumgardner, C.; Song, N.; Zhang, Y.; Li, J.; Li, X. Cotton-Textile-Enabled Flexible Self-Sustaining Power Packs via Roll-to-Roll Fabrication. *Nat. Commun.* **2016**, *7*, 11586.

(11) Gao, Z.; Song, N.; Li, X. Microstructural Design of Hybrid CoO@NiO and Graphene Nano-Architectures for Flexible High Performance Supercapacitors. *J. Mater. Chem. A* **2015**, *3*, 14833–14844.

(12) Gao, Z.; Song, N.; Zhang, Y.; Li, X. Cotton Textile Enabled, All-Solid-State Flexible Supercapacitors. *RSC Adv.* **2015**, *5*, 15438–15447.

(13) Wu, Z.; Parvez, K.; Feng, X.; Müllen, K. Graphene-Based in-Plane Micro-Supercapacitors with High Power and Energy Densities. *Nat. Commun.* **2013**, *4*.

(14) Yu, G.; Hu, L.; Liu, N.; Wang, H.; Vosgueritchian, M.; Yang, Y.; Cui, Y.; Bao, Z. Enhancing the Supercapacitor Performance of Graphene/MnO_2 Nanostructured Electrodes by Conductive Wrapping. *Nano Lett.* **2011**, *11*, 4438–4442.

(15) Wang, G.; Zhang, L.; Zhang, J. A Review of Electrode Materials for Electrochemical Supercapacitors. *Chem. Soc. Rev.* **2012**, *41*, 797–828.

(16) Cho, S. Il; Lee, S. B. Fast Electrochemistry of Conductive Polymer Nanotubes: Synthesis, Mechanism, and Application. *Acc. Chem. Res.* **2008**, *41*, 699–707.

(17) Chen, Z.; Augustyn, V.; Wen, J.; Zhang, Y.; Shen, M.; Dunn, B.; Lu, Y. High-Performance Supercapacitors Based on Intertwined CNT/V2O5 Nanowire Nanocomposites. *Adv. Mater.* **2011**, *23*, 791–795.

(18) Beidaghi, M.; Wang, C. Micro-Supercapacitors Based on Interdigital Electrodes of Reduced Graphene Oxide and Carbon Nanotube Composites with Ultrahigh Power Handling Performance. *Adv. Funct. Mater.* **2012**, *22*, 4501–4510.

(19) Simon, P.; Gogotsi, Y. Materials for Electrochemical Capacitors. *Nat. Mater.* **2008**, *7*, 845–854.

(20) Lv, T.; Yao, Y.; Li, N.; Chen, T. Highly Stretchable Supercapacitors Based on Aligned Carbon Nanotube/Molybdenum Disulfide Composites. *Angew. Chemie Int. Ed.* **2016**, *55*, 9191–9195.

(21) Zhu, C.; Liu, T.; Qian, F.; Han, T. Y.-J.; Duoss, E. B.; Kuntz, J. D.; Spadaccini, C. M.; Worsley, M. A.; Li, Y. Supercapacitors Based on Three-Dimensional Hierarchical Graphene Aerogels with Periodic Macropores. *Nano Lett.* **2016**, *16*, 3448–3456.

(22) Zhang, L. L.; Zhou, R.; Zhao, X. S. Graphene-Based Materials as Supercapacitor

Electrodes. *J. Mater. Chem.* **2010**, *20*, 5983.

(23) El-Kady, M. F.; Strong, V.; Dubin, S.; Kaner, R. B. Laser Scribing of High-Performance and Flexible Graphene-Based Electrochemical Capacitors. *Science* **2012**, *335* , 1326–1330.

(24) Huang, Y.; Liang, J.; Chen, Y. An Overview of the Applications of Graphene-Based Materials in Supercapacitors. *Small* **2012**, *8*, 1805–1834.

(25) Huang, X.; Qi, X.; Boey, F.; Zhang, H. Graphene-Based Composites. *Chem. Soc. Rev.* **2012**, *41*, 666–686.

(26) Chee, W. K.; Lim, H. N.; Zainal, Z.; Huang, N. M.; Harrison, I.; Andou, Y. Flexible Graphene-Based Supercapacitors: A Review. *J. Phys. Chem. C* **2016**, *120*, 4153–4172.

(27) Nyholm, L.; Nyström, G.; Mihranyan, A.; Strømme, M. Toward Flexible Polymer and Paper-Based Energy Storage Devices. *Adv. Mater.* **2011**, *23*, 3751.

(28) Pan, L.; Yu, G.; Zhai, D.; Lee, H. R.; Zhao, W.; Liu, N.; Wang, H.; Tee, B. C.-K.; Shi, Y.; Cui, Y.; Bao, Z. Hierarchical Nanostructured Conducting Polymer Hydrogel with High Electrochemical Activity. *Proc. Natl. Acad. Sci. U. S. A.* **2012**, *109*, 9287–9292.

(29) Xie, Y.; Du, H.; Xia, C.; Porous poly(3,4-ethylenedioxythiophene) nanoarray used for flexible supercapacitor. *Microporous Mesoporous Mater.*, 2015, **204**, 163–172.

(30) Anothumakkool, B.; Soni, R.; Bhange, S. N.; Kurungot, S.; Novel scalable synthesis of highly conducting and robust PEDOT paper for a high performance flexible solid supercapacitor. *Energy Environ. Sci.*, 2015, **8**, 1339–1347.

(31) Hsu,Y.-K.; Chen, Y.-C.; Lin, Y.-G.; Chen, L.-C.; Chen, K.-H.; Direct-growth of poly(3,4-ethylenedioxythiophene) nanowires/carbon cloth as hierarchical supercapacitor electrode in neutral aqueous solution. *J. Power Sources*, 2013, **242**, 718–724.

(32) Zhao, Z.; Moussa, M.; Shi, G.; Meng, Q.; Wang, R.; Ma, J.; Compressible, electrically conductive, fibre-like, three-dimensional PEDOT-based composite aerogels towards energy storage applications. *Compos. Sci. Technol.*, 2016, **127**, 36–46.

(33) Memon, M. A.; Bai, W.; Sun, J.; Imran, M.; Phulpoto, S. N.; Yan, S.; Huang, Y.; Geng, J. Conjunction of Conducting Polymer Nanostructures with Macroporous Structured Graphene Thin Films for High-Performance Flexible Supercapacitors. *ACS Appl. Mater. Interfaces* **2016**, *8*, 11711–11719.

(34) Wang, Z.; Carlsson, D. O.; Tammela, P.; Hua, K.; Zhang, P.; Nyholm, L.; Strømme, M. Surface Modified Nanocellulose Fibers Yield Conducting Polymer-Based Flexible

Supercapacitors with Enhanced Capacitances. *ACS Nano* **2015**, *9*, 7563–7571.

(35) Du, P.; Liu, H. C.; Yi, C.; Wang, K.; Gong, X. Polyaniline-Modified Oriented Graphene Hydrogel Film as the Free-Standing Electrode for Flexible Solid-State Supercapacitors. *ACS Appl. Mater. Interfaces* **2015**, *7*, 23932–23940.

(36) Wu, Q.; Xu, Y.; Yao, Z.; Liu, A.; Shi, G. Supercapacitors Based on Flexible Graphene/Polyaniline Nanofiber Composite Films. *ACS Nano* **2010**, *4*, 1963–1970.

(37) Xie, Y.; Liu, Y.; Zhao, Y.; Tsang, Y. H. Stretchable All-Solid-State Supercapacitor with Wavy Shaped Polyaniline/graphene Electrode. *J. Mater. Chem. A* **2014**, *2*, 9142–9149.

(38) Huang, Y.; Zhu, M.; Pei, Z.; Huang, Y.; Geng, H.; Zhi, C. Extremely Stable Polypyrrole Achieved via Molecular Ordering for Highly Flexible Supercapacitors. *ACS Appl. Mater. Interfaces* **2016**, *8*, 2435–2440.

(39) Yuan, L.; Yao, B.; Hu, B.; Huo, K.; Chen, W.; Zhou, J. . Polypyrrole-Coated Paper for Flexible Solid-State Energy Storage. *Energy Environ. Sci.* **2013**, *6*, 470.

(40) Yu, C.; Ma, P.; Zhou, X.; Wang, A.; Qian, T.; Wu, S.; Chen, Q. All-Solid-State Flexible Supercapacitors Based on Highly Dispersed Polypyrrole Nanowire and Reduced Graphene Oxide Composites. *ACS Appl. Mater. Interfaces* **2014**, *6*, 17937–17943.

(41) Tang, P.; Han, L.; Zhang, L. Facile Synthesis of Graphite/PEDOT/MnO_2 Composites on Commercial Supercapacitor Separator Membranes as Flexible and High-Performance Supercapacitor Electrodes. *ACS Appl. Mater. Interfaces* **2014**, *6*, 10506–10515.

(42) Wang, K.; Zhao, P.; Zhou, X.; Wu, H.; Wei, Z. Flexible Supercapacitors Based on Cloth-Supported Electrodes of Conducting Polymer Nanowire array/SWCNT Composites. *J. Mater. Chem.* **2011**, *21*, 16373.

(43) Meng, Y.; Wang, K.; Zhang, Y.; Wei, Z. Hierarchical Porous Graphene/Polyaniline Composite Film with Superior Rate Performance for Flexible Supercapacitors. *Adv. Mater.* **2013**, *25*, 6985–6990.

(44) Zhao, Y.; Liu, J.; Hu, Y.; Cheng, H.; Hu, C.; Jiang, C.; Jiang, L.; Cao, A.; Qu, L. Highly Compression-Tolerant Supercapacitor Based on Polypyrrole-Mediated Graphene Foam Electrodes. *Adv. Mater.* **2013**, *25*, 591–595.

(45) Rajamanickam, R.; Kumari, S.; Kumar, D.; Ghosh, S.; Kim, J. C.; Tae, G.; Sen Gupta, S.; Kumaraswamy, G. Soft Colloidal Scaffolds Capable of Elastic Recovery after Large Compressive Strains. *Chem. Mater.* **2014**, *26*, 5161–5168.

(46) Chatterjee, S.; Sen Gupta, S.; Kumaraswamy, G. Omniphilic Polymeric Sponges by Ice Templating. *Chem. Mater.* **2016**, *28*, 1823–1831.

(47) Gutiérrez, M. C.; Ferrer, M. L.; del Monte, F. Ice-Templated Materials: Sophisticated Structures Exhibiting Enhanced Functionalities Obtained after Unidirectional Freezing and Ice-Segregation-Induced Self-Assembly. Chem. Mater. 2008, 20, 634–648.

(48) Leventis, N.; Chidambareswarapattar, C.; Bang, A.; Sotiriou-Leventis, C. Cocoon-in-Web-Like Superhydrophobic Aerogels from Hydrophilic Polyurea and Use in Environmental Remediation. *ACS Appl. Mater. Interfaces* **2014**, *6*, 6872–6882.

(49) Deville, S. Ice-templating, freeze casting: Beyond materials processing. *J. Mater. Res.* **2013**,28, 2202-2219.

(50) Sun, J.; Memon, M. A.; Bai, W.; Xiao, L.; Zhang, B.; Jin, Y.; Huang, Y.; Geng, J. Controllable Fabrication of Transparent Macroporous Graphene Thin Films and Versatile Applications as a Conducting Platform. *Adv. Funct. Mater.* **2015**, *25*, 4334–4343.

(51) Das, C.; Krishnamoorthy, K. Disassembly of Micelles in Nanoscopic Space to Prepare Concentric Nanotubes with Variable Hydrophobic Interiors. *Chem. Commun.* **2014**, *50* , 5905.

(52) Das, C.; Jain, B.; Krishnamoorthy, K. Phenols from Green Tea as a Dual Functional Coating to Prepare Devices for Energy Storage and Molecular Separation. *Chem. Commun.* **2015**, *51*, 11662–11664.

(53) Sileika, T. S.; Barrett, D. G.; Zhang, R.; Lau, K. H. A.; Messersmith, P. B. Colorless Multifunctional Coatings Inspired by Polyphenols Found in Tea, Chocolate, and Wine. *Angew. Chem. Int. Ed. Engl.* **2013**, *52*, 10766–10770.

(54) Huang, S.; Zhang, Y.; Shi, J.; Huang, W. Superhydrophobic Particles Derived from Nature-Inspired Polyphenol Chemistry for Liquid Marble Formation and Oil Spills Treatment. *ACS Sustain. Chem. Eng.* **2016**, *4*, 676–681.

(55) Sotzing, G. A.; Reynolds, J. R.; Steel, P. J. Poly(3,4-Ethylenedioxythiophene) (PEDOT) Prepared via Electrochemical Polymerization of EDOT, 2,2'-Bis(3,4-Ethylenedioxythiophene) (BiEDOT), and Their TMS Derivatives. *Adv. Mater.* **1997**, *9*, 795–798.

(56) Groenendaal, L.; Jonas, F.; Freitag, D.; Pielartzik, H.; Reynolds, J. R. Poly(3,4-Ethylenedioxythiophene) and Its Derivatives: Past, Present, and Future. *Adv. Mater.* **2000**, *12*, 481–494.

(57) Österholm, A. M.; Shen, D. E.; Dyer, A. L.; Reynolds, J. R. Optimization of PEDOT

Films in Ionic Liquid Supercapacitors: Demonstration As a Power Source for Polymer Electrochromic Devices. *ACS Appl. Mater. Interfaces* **2013**, *5*, 13432–13440.

(58) L. J. Gibson, M. F. Ashby, Cellular Solids: Structure and Properties, Cambridge University Press, New York, **1999**.

(59) Zhou, C.; Liu, Z.; Yan, Y.; Du, X.; Mai, Y. Electro-Synthesis of Novel Nanostructured PEDOT Films and Their Application as Catalyst Support. *Nanoscale Res. Lett.* **2011**. 6: 364.

Omniphilic Polymeric Sponges by Ice Templating

In this chapter, we report the preparation of macroporous polymer sponges by ice templating of polyethyleneimine aqueous solutions and their crosslinking in the frozen state. These sponges can absorb a large quantity of solvent relative to their weight, independent of the solvent polarity. Thus, they represent useful universal absorbents for laboratory and industrial spills. The as-prepared monolith is hydrophilic and absorbs over 30-fold its weight in water. Modification of this sponge using valeroyl chloride renders it omniphilic, viz. a modified sponge absorbs over 10-fold its dry weight of either water or hexane. Modification using palmitoyl chloride that has a longer chain length results in the preparation of a hydrophobic sponge with a water contact angle around 130^0, that retains its oleophilicity underwater. The solvent absorbed in these sponges can be simply squeezed out and the sponges are stable to several hundred compression/expansion cycles. The large pore sizes of these sponges allow rapid absorption of even high viscosity solvents such as pump oil. Finally, we demonstrate that these sponges are also able to separate apolar oils that are emulsified in water using surfactants. These high porosity sponges with controllable solvophilicity represent inexpensive, high performance universal absorbents for general solvent spills.

4.1 Introduction

In the case of a solvent spill, the general response is to control the spread of the liquid and to absorb it. The ACS Guide for Chemical Spill Response Planning[1] suggests that materials such as vermiculite or cat litter could be used to absorb a variety of solvents. Most laboratories and industries that use solvents have commercially available absorbents that can be used to mitigate solvent spills. For, example, activated carbon based materials such as Solusorb®, are used to respond to spills involving flammable liquids. There are also several commercial absorbent pillows and pads that are used as "universal" absorbents for liquids of different polarities, ranging from water to apolar oils. These are typically based on natural fibers such as cellulose or fine melt-blown synthetic fibers of polypropylene or polyesters. However, the absorption capacity of these materials is limited to ~O(100 ml/kg) for the activated carbon based materials and is about 10-fold higher for the synthetic fiber based pillows. There is a need to develop materials for management of solvent spills, that can rapidly absorb large quantities of solvent, independent of the solvent polarity and viscosity.

Recently, there has been intense research in the area of materials design and optimization for containment of oil spills and for efficient oil-water separation. Such materials are typically not universal absorbents. Rather, they are either superhydrophilic or superoleophilic to enable near complete separation of apolar fluids from water. A variety of porous materials have been employed[2] including mineral-based materials[3-5] such as aerogels,[6] modified clays[7-8] and metal-organic frameworks.[9] Recently, crosslinked mesoporous polymers have been reported[10] for rapid separation of organic micropollutants from water. High capacity, lightweight absorbents have also been derived from natural fibers,[11-14] including cotton, kapok and cellulose. The majority of recent reports have focused on polymeric sponges[15-25] or materials prepared using carbon fibers or carbon nanoparticles.[26-28] Recent reports have demonstrated that the microstructure of the porous materials plays an important role in determining their wetting and absorption. For example, oleophilic polyurethane aerogels that comprise micron sized polymer particles in a nanofiber mesh exhibit a "petal" effect[29]- water drops exhibit a large contact angle on their surface but remain pinned to it and do not roll off. In another example,[30] carbon-based aerogels with walls comprised of sheet-like graphene supported on CNT ribs are elastic and show high absorption of apolar oils. There has also been interest in understanding the role of surface engineering, including surface modification and creating textured surfaces, on wettability.[31-38] These advances have

allowed the fabrication of materials that are hydrophobic and that retain their oleophilicity underwater. However, very little attention has been focused on truly omniphilic sponges that are capable of absorbing large volumes of either polar or apolar solvents.

Here, we describe a macroporous monolith prepared by crosslinking polyethyleneimine,that affords sponges varying from hydrophilic to omniphilic to oleophilic underwater. Ice templating is employed to generate the macroporous structure. This is a facile process where an aqueous polymer solution is frozen and the ice crystals are used as pore templates. This is a well-established technique[39,40]and has been used to prepare porous monoliths from a variety of polymers.[39-45] We demonstrate that the surface of the crosslinked polyethyleneimine walls in our scaffolds can be readily modified by covalent grafting with alkyl chains and, that varying the chain length of these hydrophobic modifiers allows us to controllably vary the solvophilicity of the sponges.

4.2 Experimental

4.2.1 Materials:

Polyethylenimine (PEI , branched polymer with supplier specified molecular weight = 25kDa), 1,4-butanediol diglycidyl ether, Oil Red O were obtained from Sigma Aldrich and were used as received. Distilled deionized water (resistivity 18.2 MΩ.cm) from a Millipore MilliQ unit was used as solvent to prepare sponges. Valeroyl chloride (that we term as C4), nonanoyl chloride (termed C8), palmitoyl chloride (termed C17), sodium dodecyl sulfate (SDS), cetyltrimethylammonium bromide (CTAB), Oil Red O were obtained from Sigma Aldrich and were used as received. Triethylamine (TEA) was obtained from Merck (India) and was used without any further purification. Chloroform (HPLC grade), n-hexane (AR grade), tetrahydrofuran (THF) and dichloromethane (DCM) were obtained from Thomas-Baker and were dried with molecular sieves before use. Edward's Ultra grade 9 oil was used to examine the absorption kinetics of viscous oil.

4.2.2. Fabrication of self-standing cross-linked polymer sponges by ice templating:

Typically 480 µl water and 12 mg (120 µl of 100mg/ml stock solution) PEI were vortex mixed in a 2 ml plastic tube. To this polymer solution, 10 mg of 1, 4-butanediol diglycidyl ether (cross-linker) was added. This plastic tube was immediately frozen by placing in a

freezer at -15°C and then maintained at this temperature for 24 hours to allow crosslinking to proceed. After 24 hours of cross-linking, the sponge was carefully taken out from the refrigerator and thawed at room temperature. This "as prepared" sponge was washed multiple times with copious amounts of water to remove the sol fraction. This sponge was termed S_0.

4.2.3 Hydrophobization of S_0:

Hydrophobization of the as prepared sponge, S_0, was performed by reacting amine groups on the PEI with acyl chlorides using an amidation reaction. For this, S_0 was first incubated in THF (tetrahydrofuran) for 24 h and then dried in a vacuum oven at 55°C for 24 h. To ensure thorough drying, the sponge was taken into a 10 ml two neck RB and kept under vacuum with constant purging of argon. To the dry sponge 22 mg (corresponding to 0.28 mmol of ethylene imine monomer units) was added in 5 ml of dry chloroform. To this, 50 µl of TEA (triethylamine) and excess amount of acid chloride (0.6 mmol), was added and, the sponge was stirred at room temperature (25°C) for 12 hours under argon atmosphere. After 12 hours, the modified sponge was washed several times with chloroform and tetrahydrofuran to remove by-products. Sponges modified using treatment with different acid chlorides viz., valeroyl chloride (C4), nonanoyl chloride (C8) and palmitoyl chloride (C17) were named as S_{C4}, S_{C8} and S_{C17} , respectively.

4.2.4 Preparation of surfactant solutions:

200 mg surfactant, 500 µl hexane and 50 ml water were mixed together at 5000 rpm for 10 min using IKA Ultratrax mixture. The emulsion was then allowed to equilibrate for 12 hours before the absorption experiments. 10 ml of the aliquot was taken into 15 ml glass vials each, and stirred in presence of S_0, S_{C4} and S_{C17} sponges respectively for 24 hours. After 24 hours, hexane and the surfactant in the oil phase was extracted from the emulsion with 5 ml dichloromethane (DCM) in a 25 ml separatory funnel. The extracted mixture was then allowed to pass through a silica column with small amount of sodium sulphate to remove surfactant and trace amount of water. The purified solvent mixtures (hexane in DCM) were stored in sealed glass vials and stored at cold environment to ensure no loss of solvent due to evaporation. The amount of unabsorbed hexane was then calculated with the help of Gas Chromatography (GC).

4.3 Characterization

The morphology of the polymeric sponges was imaged using a Quanta 200 3D scanning electron microscope (SEM). FT-IR measurements were performed using a Bruker instrument in ATR mode, by averaging over 20 scans with a resolution of 4 cm^{-1}. Contact angle measurements were performed using home-built equipment at the University of Pune. Absorbance measurements were performed using a UV-spectrometer (Agilent89090A) in standard transmission mode. Mechanical properties of the sponges were measured using a strain controlled rheometer, TA-ARES G2, equipped with a normal force transducer. Tests were performed by placing sponges between 25 mm roughened parallel plates to prevent slippage of the sample. We performed "force gap" tests and measured the normal forces during cyclic compressional loading of the sponges. Data at loading and unloading rates of 0.05 mm/s are reported. We note that there was no change in the stress-strain data for 10-fold variation of the loading/unloading rates. Nominal compression stress calculated on the basis of the original diameter of the cylindrical samples (9.1 mm) is reported. Compression tests were performed for dry sponges as well as sponges that were soaked in solvent (water for S_0 and hexane for S_{C8} and S_{C17}). For tests on solvent-soaked sponges, we used excess solvent in a pool on the bottom plate of the rheometer to eliminate drying of the sample. All mechanical measurements were performed at room temperature (25 °C).

4.4 Results and Discussion

4.4.1 Preparation and Structural Characterization of Macroporous Sponges:

Macroporous sponges were prepared by ice-templating. An aqueous solution of polyethylenimine (PEI, M_w = 750 kDa) and diepoxide cross-linker were vortex mixed in an Eppendorf tube and were frozen by placing in a refrigerator at -15 °C. This protocol is similar to that reported by Kumari et.al. for the preparation of polymer-colloid hybrids.[46] The PEI and diepoxide are expelled by the ice and form a connected three-dimensional macroporous structure that is a negative replica of the ice crystals. Cross-linking proceeds in the frozen state such that, after a day the sample can be thawed to afford a self-standing macroporous monolith. This is schematically represented in Scheme 2.1 and Scheme 4.1 and a photograph of a centimeter-sized monolith thus produced is shown. SEM of the monolith reveals a foam-like interconnected porous structure (Figure 4.1) with an average pore

diameter of 50 μm, with pore walls comprised of crosslinked polymer (as depicted in the

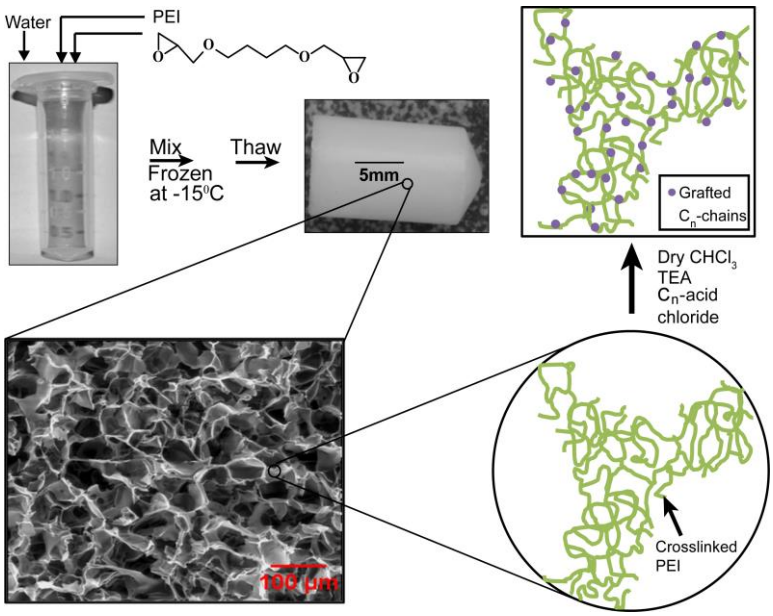

Scheme 4.1: Schematic representation of the ice templating process To prepare macroscopic sponges, followed by their chemical modification using alkyl acid chlorides.

cartoon schematic in Scheme 2.1). This monolith is subjected to hydrophobic modification by reacting residual amine groups on the PEI with an excess of acid chloride. The "as prepared" sponge is termed S_0 and sponges hydrophobized using valeroyl, nonanoyl and palmitoyl chloride are termed S_{C4}, S_{C8} and S_{C17}, respectively. The weight of the sponges is measured before and after modification and we note that there is, on average, a ≈40 %, ≈87 % and ≈122 % increase in weight respectively for S_{C4}, S_{C8} and S_{C17}, relative to the unmodified sponge. This data suggests that approximately 20-25 % of the amine groups in the PEI react with the modifiers, independent of the modifier chain length.

Modification of S_0 by reaction with acid chlorides was confirmed using IR-spectroscopy (Figure 4.2). An intense band peaked at 1626 cm^{-1} emerges for modified sponges, that is absent in S_0, corresponding to the amide carbonyl stretch. Further, the CH stretching bands at 2852 and 2919 cm^{-1} are progressively more intense for S_{C4}, S_{C8} and S_{C17} relative to S_0 (Figure 4.2). This attributes the presence of alkyl groups in the modified sponges. Thus, this data confirms that PEI amine groups in S_0 react with the acid chlorides to form covalent amide linkages.

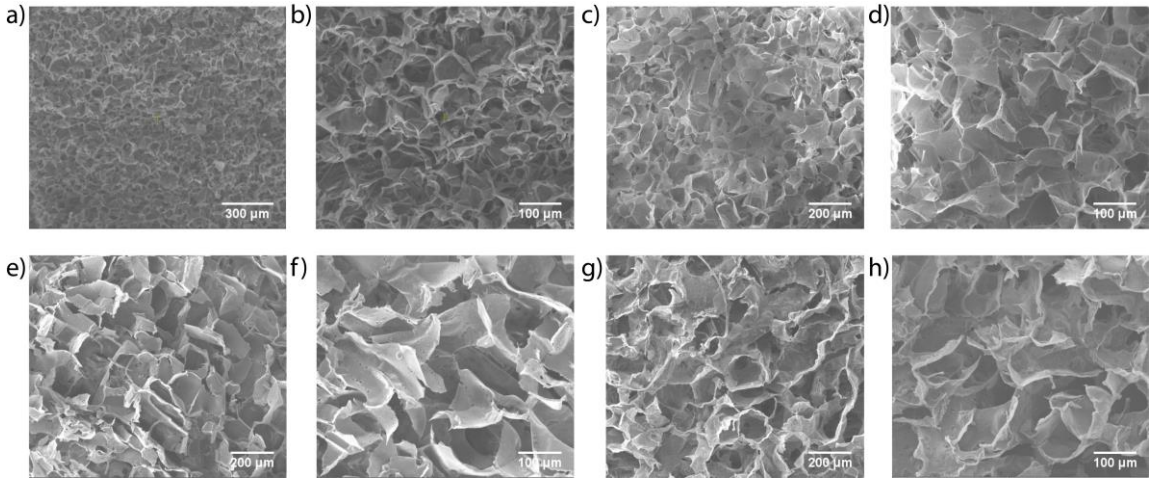

Figure 4.1: SEM images of S_0 (a,b); S_{C4} (c,d); S_{C8} (e,f) and S_{C17} (g,h) at different magnifications. Scale bars are as indicated in the images.

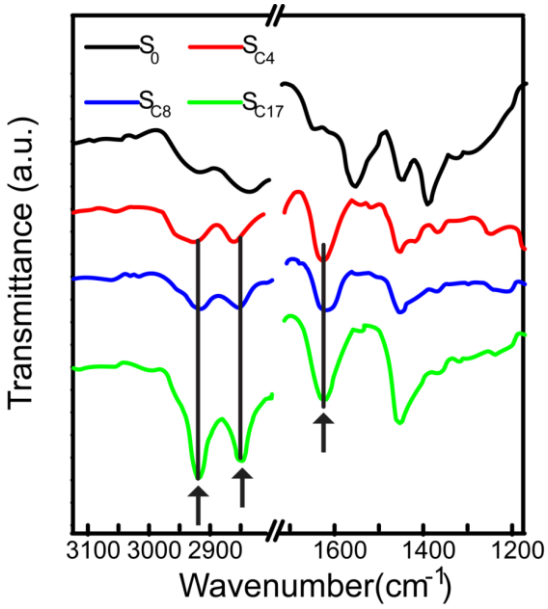

Figure 4.2: FTIR spectra of the sponges, S_0 to S_{C17}. Spectra are vertically offset for clarity. The characteristic bands that confirm covalent modification are indicated using arrows.

S_0 swells in water. With increase in the length of the grafted alkane chain from S_{C4} to S_{C8} to S_{C17}, there is decreased affinity for water and an increased affinity for apolar solvents, as evidenced by contact angle measurements. The water contact angle is measured for S_0 and the modified sponges to examine the effect of alkane chain grafting. To do that, a 5 µl water droplet is placed on the surface of thoroughly dried sponges and we measure the contact angle from a photograph of the drop (Figure 4.3, left). On S_0, the water droplet spread rapidly on the surface and was absorbed by the sponge. On S_{C4}, S_{C8} and S_{C17}, the apparent contact

angle immediately after depositing the drop of water was 106, 125 and 131°,respectively, indicating a systematic increase in the hydrophobicity of the sponge. However, for S_{C4}, there is a steady decrease in the water drop contact angle with time (Figure 4.3, right). The contact angle decreases below 90° after about a minute and to about 75° after 10 minutes. The contact angle continues to decrease as the sponge is wetted by the water. Eventually, the drop is absorbed by the sponge. In contrast, for S_{C8}, the contact angle initially decreases in the first few seconds and subsequently plateaus at about 116° (Figure 4.3). For the S_{C17}, the decrease in contact angle with time is minimal, less than 1° (Figure 4.3). The change in the contact angle exhibits discontinuities (see data for S_{C4} and S_{C8}, Figure 4.3). These discontinuities can be attributed to heterogeneities on the surface of the sponges. Here, we present data for experiments on one set of sponges in Figure 4.3 – however, such discontinuities were observed when these experiments were repeated on other samples. As might be expected, the time when these discontinuities were observed varied from experiment to experiment.

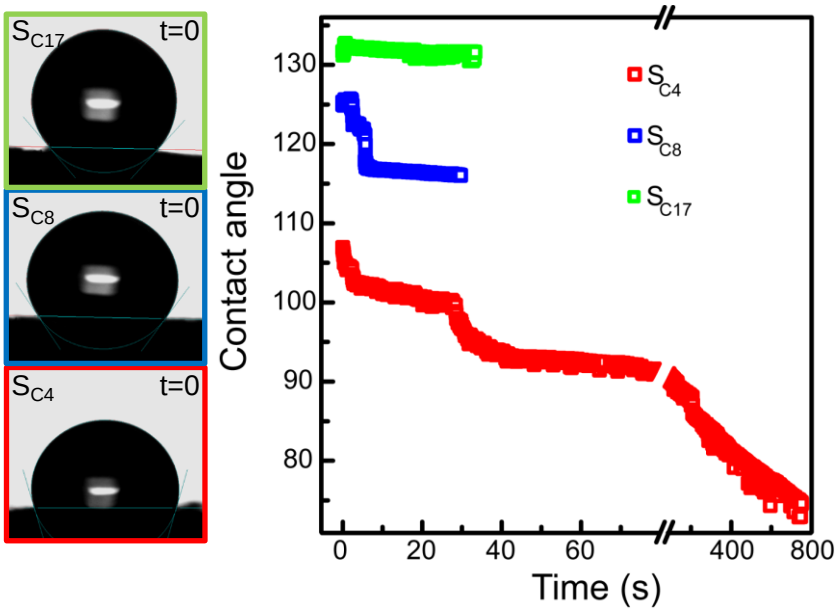

Figure 4.3: Photographs of water droplets immediately after deposition on S_{C17}, S_{C8}, and S_{C4} (left, top to bottom). Change in the water contact angle with time is shown on the right.

Further, we observe no significant difference in the water contact angle measured on sections cut from different parts of a dry S_{C17} sponge. This indicates that there is no significant spatial variation in the extent of modification between the inner and outer regions of the sponge.

4.4.2 Compression-Expansion of Sponges:

It is possible to reuse sponges if the solvent imbibed in them can be readily extracted by squeezing and, if the sponges readily recover from compression. Therefore, the response of the sponges to compression is characterized. Sponges are subjected to repeated compression/expansion cycles in the rheometer and nominal compressive stress (based on the initial cross-sectional area) is reported as a function of compressive strain (Figure 4.4). Stress-strain data are presented here for S_0 swollen in water (Figure 4.4a) and for S_{C4}, S_{C8} and S_{C17} swollen in hexane (Figures 4.4 b-d) respectively. The sponges exhibit behavior that is typical for macroporous foams. For all sponges, the stress-strain relationship is approximately linear at small strains. On increasing strain, the stress plateaus and then increases rapidly. The rapid increase in stress corresponds to a strain regime where the pore walls collapse and come into contact with each other.

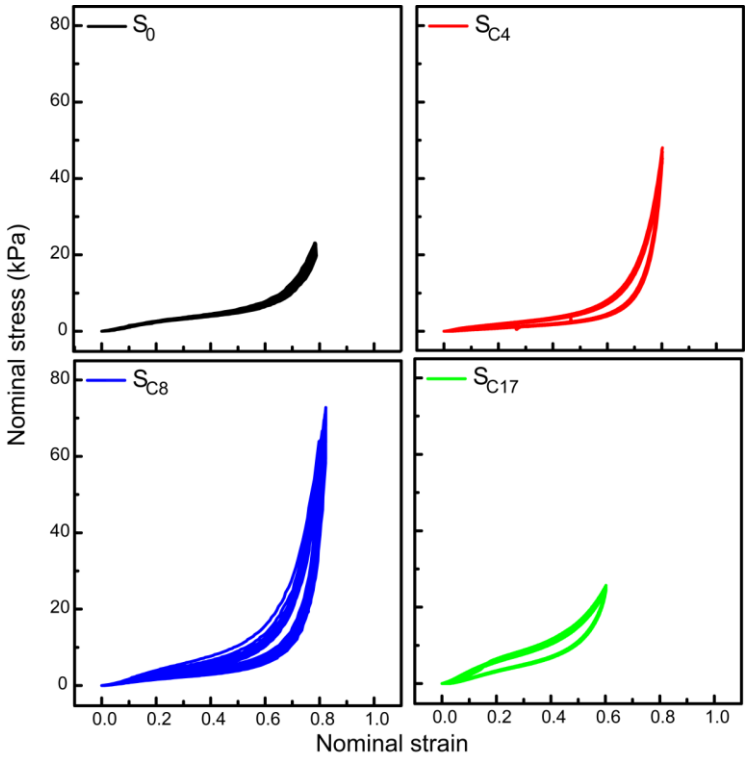

Figure 4.4: Nominal stress−strain plots for multiple compression−expansion cycles of S_0 (in water) and S_{C4}, S_{C8}, and S_{C17} (in hexane). There is no systematic change in the stress−strain plots over 400 cycles of compression−expansion.

The sponges are held in a pool of solvent during stress-strain measurements. As the sponges are compressed, the solvent inside them is expelled into the pool. When the compressive

strain is released, the sponges recover their original dimensions and the solvent appears to be simultaneously reabsorbed. It can be noted that S_0, S_{C4} and S_{C8} exhibit elastic recovery from 80% compressive strain. However, for S_{C17}, we observe that the sponge fails between 60% and 80% compressive strain (Figure 4.5). Therefore, repeated compression up to 60% compression of S_{C17} is reported here. Over 80% of the hexane contained in a saturated S_{C17} sponge can be squeezed out on compressing to a strain of 70%.All the sponges are subjected to repeated compression-reexpansion cycles. We observe that the sponges are stable and exhibit no change in mechanical response for up to 400 compression cycles. While the response of the sponges to compressive deformation is elastic, all the sponges exhibit hysteresis. The area in the hysteresis loop, relative to the area under the stress-strain curve during compression increases from ≈15% for S_0 to ≈35% for $S_{C4,}$ ≈40% for S_{C8} and ≈50% for S_{C17}. Thus, while a complete recovery is observed after compression, there is a systematic increase in the energy dissipation during the compression/expansions. This is correlated with the decrease in failure strain for S_{C17} relative to S_0.

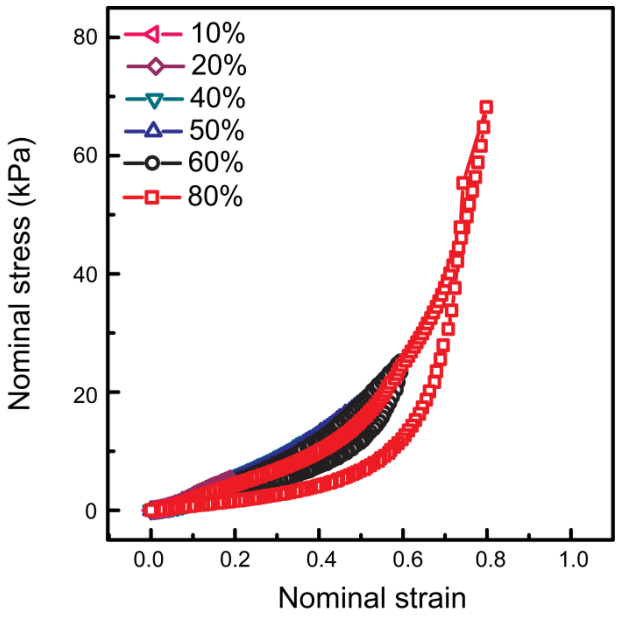

Figure 4.5: Compression-expansion of S_{C17} at different strain in hexane.

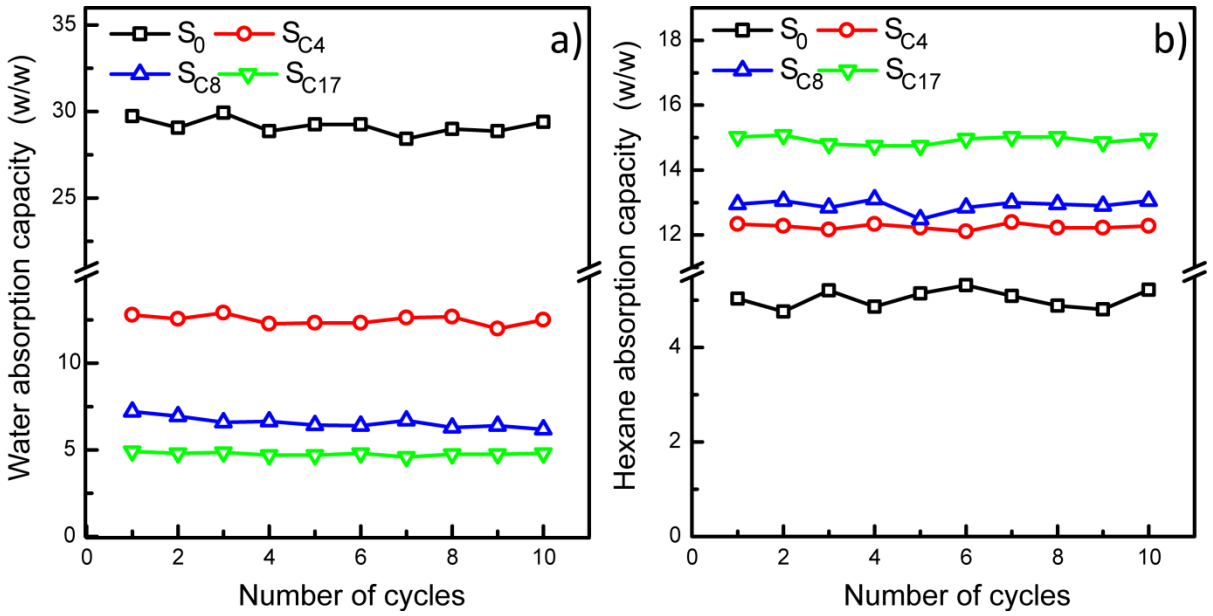

Figure 4.6: Absorption of (a) water and (b) hexane by the sponges after solvent immersion until saturation. The sponges are squeezed and allowed to reabsorb solvent. Data is presented over 10 cycles of absorption.

4.4.3 Solvent Absorption by Sponges:

The ability of these sponges to absorb water, a polar solvent as well as hexane, an apolar solvent is evaluated in Figure 4.6. Thoroughly vacuum dried sponges are soaked in solvent for 12 hours to ensure equilibrium absorption. The weight of the solvent-swollen sponge is measured after carefully wiping excess solvent off it. The absorption capacity (W_{abs}), was calculated as the ratio of the weights of absorbed solvent to the dry weight of the sponge as: $W_{abs}= (W_{sat}– W_{dry})/ W_{dry}$, where W_{dry} and W_{sat} are the weight of sponge before and after solvent absorption, respectively. Solvent-swollen sponges were compressed to expel solvent. Subsequently, the "squeezed-dry" sponge was placed in solvent and the uptake in the next cycle of absorption was measured. 10 such absorption-compression cycles were carried out. We observe there is no systematic change in solvent absorption over 10 experimental cycles.

The sponges are macroporous with ~O(100 μm) size pores. Capillary action draws wetting fluids into the pores and the polymeric pore walls can also absorb solvent as the crosslinked polymer solvates. The pore volume, solvophilicity and extent of polymer crosslinking in the walls of the sponge determine the solvent uptake. The "as prepared" sponge, S_0, is hydrophilic and, it is likely that the residual amine groups strongly hydrogen bond with water. Thus, a water droplet placed on its surface is rapidly absorbed by the sponge. On immersing S_0 in water for 12 hours, it is observed that it absorbs 29 – 30 times its

weight of water (Figure 4.6a). The absorption of hexane is also examined by immersing a dry S_0 sponge in hexane for 12 hours (Figure 4.6b). PEI is insoluble in hexane. However, hexane has a low surface tension and wetting of S_0 walls (possibly due to interaction of hexane with the PEI backbone) results in modest swelling (4 – 5 times the dry sponge weight). In contrast, S_{C17}, viz. the sponge modified with the longest alkane chain shows modest water absorption (4 – 5 times its dry weight) and hexane absorption of ~15 times its weight. The behaviour of S_{C4} and S_{C8} is intermediate to S_0 and S_{C17}, as expected (Figure 4.6). It can be noted that S_{C4} is remarkable, in that it is able to absorb ~12 fold its weight of either a polar solvent (water) or an apolar solvent (hexane).

Absorption of water by S_{C17} is unanticipated based on the water contact angle

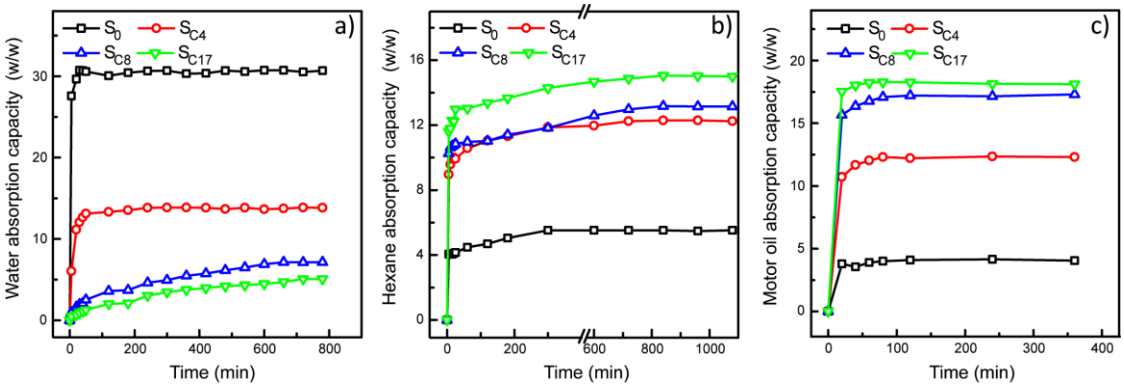

Figure 4.7: Absorption kinetics of dry sponges placed in (a) water, (b) hexane and (c) motor oil.

experiment. For S_{C17}, we have demonstrated that a water droplet placed on its surface has a large contact angle (131°) that does not change with time (Figure 4.3). However, modest water absorption is reported after immersion of the sponge for 12 hours. It is possible that the water uptake is a consequence of unreacted amine groups in the S_{C17}.

It has been observed that the absorption kinetics of water varies with hydrophobic modification (Figure 4.7). Absorption of water is extremely rapid for S_0: most of the water is absorbed within the first few minutes and absorption saturates within 20 minutes (Figure 4.7a). For S_{C4} too, water absorption is rapid and plateaus within 30 minutes (Figure 4.7a). For S_{C8} and S_{C17} however, the water absorption rises slowly with time and does not plateau even after 12 hours of immersion (Figure 4.7a). Thus, these data indicates that the pore surface of the sponge reorganizes slowly with time and allows uptake of water even in highly

hydrophobic sponges such as S_{C17}. However, the uptake in S_{C17}, even after 12 h of immersion is modest relative to S_0.

All sponges (S_0, S_{C4}, S_{C8} and S_{C17}) exhibit rapid absorption of hexane. There is an initial rapid uptake, with ~80% of the final hexane content absorbed within the first 20 minutes (Figure 4.7b). Subsequently, there is a slow increase in absorbed hexane until a plateau is observed after ~300 min (Figure 4.7b). Remarkably, even highly viscous motor oil is rapidly absorbed by the sponges, over similar time scales as low viscosity hexane (Figure 4.7c). The uptake increases rapidly within the first 20 minutes and saturates within 40 to 60 min. Again, we note that S_{C4} is omniphilic and rapidly absorbs either water or hexane or motor oil to about 12-fold the dry sponge weight (Figure 4.7). The total amount of solvent absorbed by the sponges after soaking for an extended period of time is summarized in Table 4.1.

Table 4.1: Absorption Capacity of sponges for a variety of solvents. Minimum and maximum capacity value is reported here.

Sponge	Absorption capacity (weight of solvent/weight of dry sponge)				
	Water	Hexane	Motor oil	Chloroform	Toluene
S_0	25; 30.4	4.4; 5.7	3.8; 4.1	29; 30.8	7.9; 10.3
S_{C4}	11.3; 13	11; 13.7	10.4; 13.4	37; 38.2	17.6; 18.2
S_{C8}	6.6; 9	12.8; 13.9	13.7; 17.4	36.8; 38.2	17.8; 18.2
S_{C17}	4.5; 5.2	12.8; 16.2	17.6; 18.4	38; 40	19.7; 21.3

4.4.4 Oleophilicity of sponges in the presence of water:

Figure 4.8 demonstrates the spreading and absorption of a drop of an apolar liquid, hexane, deposited on the surface of water-soaked sponges. The hexane red is coloured red for ease of visualization. We deposit a drop on the surface of a wet sponge and subsequently cut the sponge to examine the absorption of hexane by the sponge. Hexane spreads rapidly on wet S_0 due to its low surface tension (Figure 4.8a). However, when the sponge is cut, we observe that the hexane has not penetrated the interior of the wet sponge (Figure 4.8b). Thus, while low surface tension hexane can rapidly spread on the surface of S_0, there is no visible indication of solvent ingress into the hydrophilic sponge. In contrast, when a drop of hexane is deposited on water-soaked S_{C17} (Figure 4.8g), it is seen that the drop is absorbed into the sponge before it can spread substantially (Figure 4.8h). Intermediate behavior to these extremes is observed for S_{C4} and S_{C8} (Figure 4.8c-f). Thus, this data is consistent with expectation based on the relative wettibility[47,48] of the sponges by polar/apolar fluids.

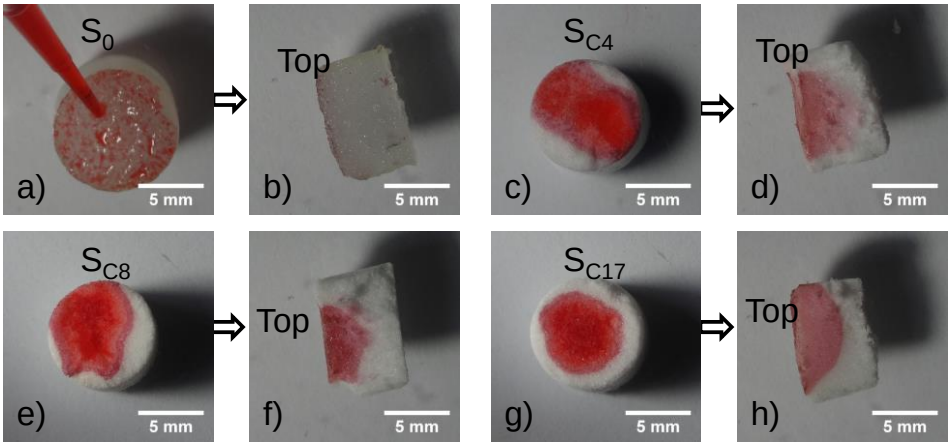

Figure 4.8: Images of a hexane droplet (dyed red) on the top surface of a water-saturated monolith. The monolith is cut vertically (viz. down the cylinder axis) to reveal the ingress of the hexane into the interior of the sponge. (a) and (b) S_0; (c) and (d) S_{C4}; (e) and (f) S_{C8}; (g) and (h) S_{C17}.

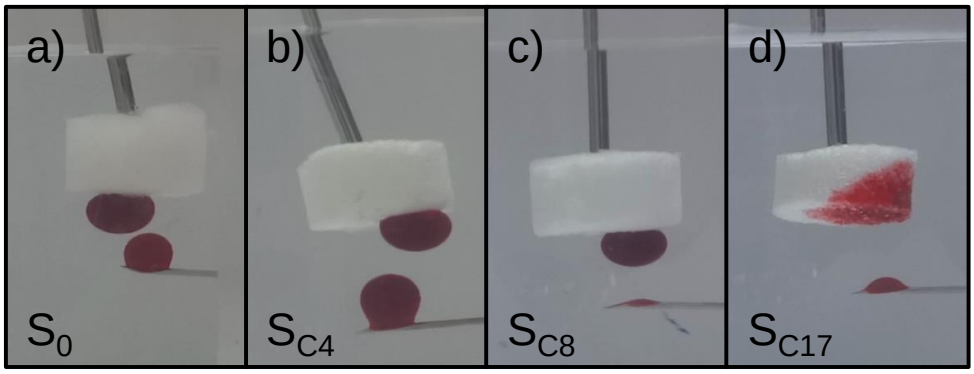

Figure 4.9: Hexane droplets (dyed red) are injected and rise in water to contact the bottom surface of (a) S_0; (b) S_{C4}; (c) S_{C8} and (d) S_{C17} held underwater. The droplets are absorbed only by S_{C17}.

We have also investigated the oleophilicity of sponges when they are held under water. Sponges were immersed in water and drops of hexane (containing red dye, for ease of visualization) were injected close to their surface. When the hexane droplets were released, they contacted the surface of the sponges as they moved up due to buoyant forces. There is a qualitative difference in the underwater oleophilicity of the modified sponges. Hexane droplets are not absorbed by S_0, S_{C4} or S_{C8} and move towards the air-water interface (Figure 4.9a-c). In contrast, hexane droplets contacting S_{C17} underwater are immediately absorbed by the sponge (Figure 4.9d). When sponges are held with a part under water and a part above the air/water interface, then their interaction with hexane droplets released underwater, near the

sponge surface, are in accord with the results of the hexane spreading experiments (Figure 4.10). Hexane is not absorbed by S_0, S_{C4} or S_{C8} underwater and rises to the air/water interface. There, it spreads on the surface of water. When this hexane contacts the part of the sponge that is in air, it spreads on the sponge surface (for S_0, S_{C4} and S_{C8}) and is partially absorbed by S_{C4} and S_{C8}. In contrast, S_{C17} retains its oleophilicity even underwater.

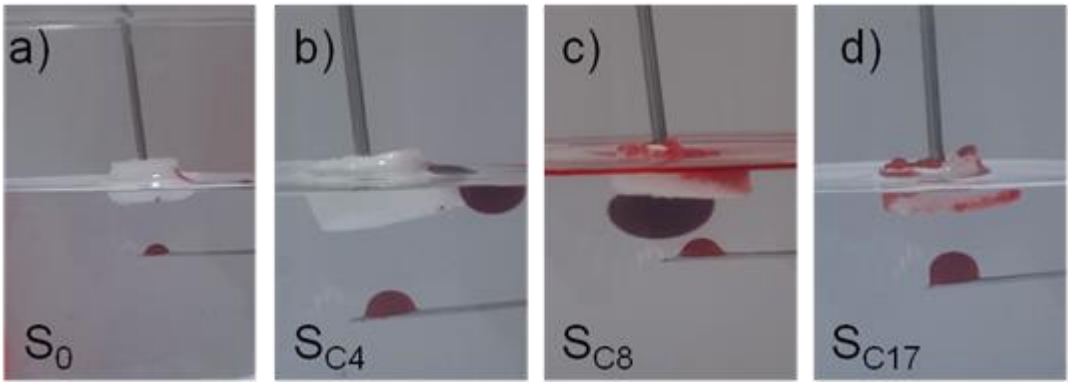

Figure 4.10: Interaction of hexane drop (red) released under water with sponges (a) S_0, (b) S_{C4}, (c) S_{C8} and (d) S_{C17} held, spanning the air-water interface. Hexane rises and spreads on the water surface. In (a) and (b), the sponge does not absorb the hexane drop. In (b), when the hexane contacts the sponge at the air-water interface, there is some absorption within the sponge. This is not readily visible in the photograph. In contrast, in (c), the hexane rises to the interface and is visibly partially absorbed by the sponge. In (d), the hexane is absorbed as it contacts the sponge underwater, before the hexane rises to the air-water interface.

In applications such as oil/water separation, for example in an oil spill, it is important that the ability to selectively absorb oil in the presence of water is retained. To investigate this, dry sponges are soaked in water and then added to an agitated water/hexane system. Here too, the hexane is dyed red using 0.06 mM Oil Red O dye for ease of visualization. It is observed that if the water/hexane system is not agitated, S_0 sinks into the water layer while S_{C4} stays at the hexane/water interface and S_{C8} and S_{C17} localize in the hexane layer (Figure 4.11). Here, we are specifically interested in the selective separation of hexane from water - therefore, we focus on the most hydrophobic sponge, S_{C17}. To quantitate hexane absorption by water-soaked S_{C17} on addition to the stirred water/hexane system, we periodically withdraw the sponge and thoroughly extract the absorbed solvent using an ethanol wash. Oil Red O dye is water insoluble. Assuming that the dye does not preferentially partition from hexane to the walls of the modified sponge, the area of the UV-Vis peaks corresponding to

Figure 4.11: Sponges (as indicated in the image) immersed in a hexane (red, top) – water (bottom) system.

the dye (at 350 and 520 nm) can be used to calculate the amount of hexane absorbed by the sponge (Figure 4.12, inset). It is observed that hexane rapidly displaces water from the water-soaked S_{C17}, and that hexane absorption in the sponge is nearly 10-fold the dry sponge weight within 0.5 minutes of stirring in the water/hexane system (Figure 4.12). There is an approximately 10% further increase in hexane uptake with time after 30 minutes of stirring in water/hexane. We note that absorption of hexane in S_{C17} within 0.5 minutes in this experiment corresponds to about 70% of the saturation absorption in a dry sponge (see Figure 4.6). This data attests to the ability of S_{C17} to selectively absorb hexane even when it is pre-soaked in water. This experiment was also repeated in a hexane/brine mixture and we observe that the ability of S_{C17} to selectively absorb hexane is similar to that reported for the hexane/water system.

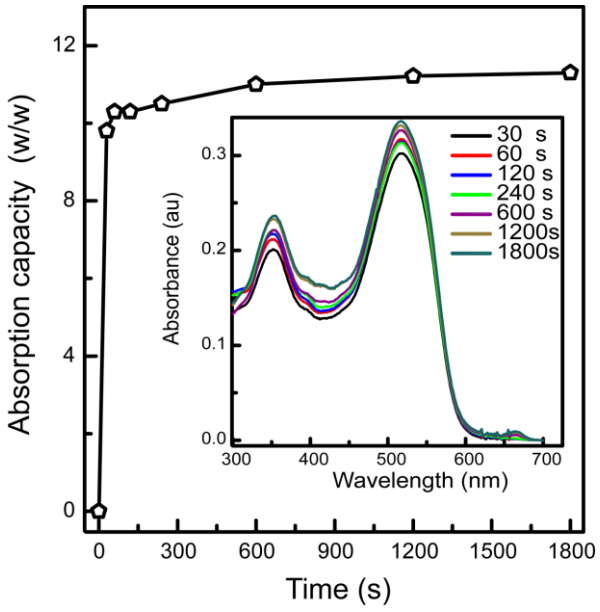

Figure 4.12: UV-vis absorbance is used to calculate the absorption of hexane when S_{C17} is agitated in an oil-water system. The UV-vis data is presented as an inset.

Finally, the ability of these sponges to separate hexane from a surfactant-stabilized emulsion of hexane in water is examined. Separation of surfactant-emulsified apolar solvents from water is very challenging and it is of great interest to evaluate the ability of these sponges to effect separations from such systems. Hexane-in-water emulsions containing 1.25 % (by weight) of hexane, using 0.5 % (by weight) of an anionic surfactant, SDS, is prepared by mixing at 5000 rpm for 10 min as described in the Section 2.2.4. The most commonly used industrial surfactants are anionic in nature – therefore, SDS is chosen as a model system. The emulsions were allowed to equilibrate for 12 h before the absorption experiment. We stirred the sponges (S_0, S_{C4} and S_{C17} weighing 20-27 mg) in the emulsions (500 µl of hexane emulsified using 200 mg SDS in 50 ml water) for 24 h. After 24 h, the sponge is removed and the hexane/surfactant in the solution is extracted by shaking with dichloromethane (DCM) in a separatory funnel. The DCM is subsequently passed through a silica column to separate the surfactant and is analyzed by injecting into a gas chromatograph to quantitatively estimate the hexane content. For GC measurement, 1 µl of the purified aliquot was injected in Gas-Chromatography instrument (Agilent Technologies, 7890B GC system). The oven temperature was set at 40°C with 2°C /min ramp and heated upto 100°C with 1 min initial hold time. It can be seen that the DCM peak is present at 3.7 min and, as expected, the hexane peak at 4.18 min disappears. The quantity of hexane is estimated the from the area under the curve at ~ 4.18 min with respect to the DCM peaks for S_0, S_{C4} and S_{C17} in CTAB and SDS stabilized emulsions (Figure 4.13a-f). We perform control experiments using an aliquot of hexane from the CTAB and SDS stabilized emulsions respectively, after 24 h stabilization (Figure 4.13 g and h). For calibration experiment, 25 µl hexane was mixed with 2.5 ml DCM and 1 µl of the aliquot was injected (Figure 4.13i). To ensure the exact peak position of hexane in a hexane/DCM mixture, an experiment with only hexane was also performed. It indicates that hexane peak appears at around 4.18 min in our experimental setup (Figure 4.13j). This data reveals that all the scaffolds are able to separate hexane from the surfactant emulsion. Remarkably, it can be noted that these sponges are also able to separate hexane from emulsions prepared using a cationic surfactant, CTAB. Thus, these data suggest that removal of emulsified hexane by the sponges might be driven by hydrophobic interactions with the omniphilic micellar tails.

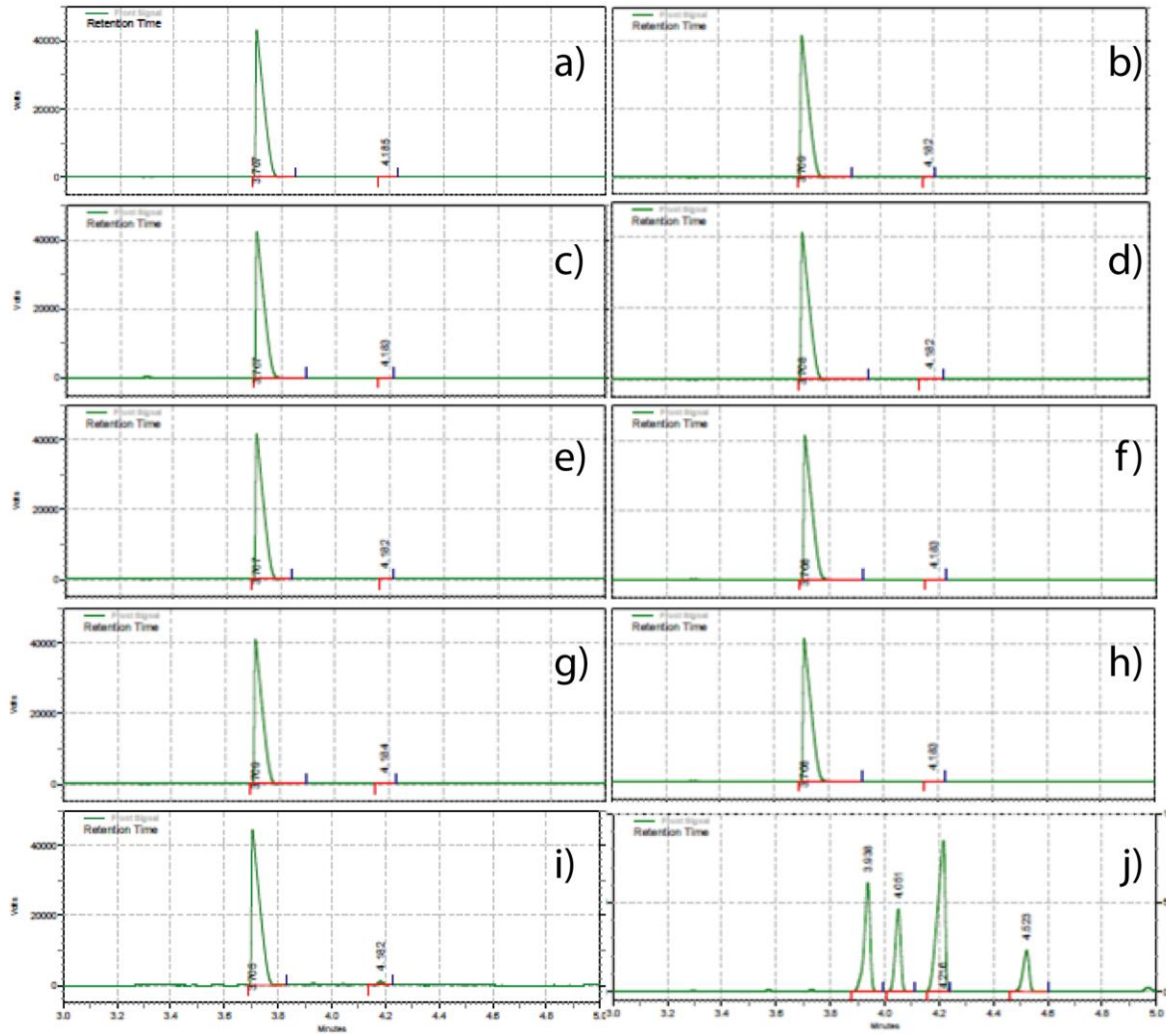

Figure 4.13: Estimation of hexane absorption from (a-c) CTAB and (d-f) SDS stabilized emulsions by S_0, S_{C4} and S_{C17} sponges respectively. Control experiments with CTAB (g) and SDS (h) Calibration plot for hexane/DCM mixture (i) and for only hexane (j).

4.5 Conclusions

Three dimensional macroporous sponges were obtained by ice-templating an aqueous polyethyleneimine solution and crosslinking the polymer in the frozen state. The as-prepared sponge is itself omniphilic: a dry sponge absorbs 30 times its weight in water or 5 times its weight in hexane. We ascribe this to the inherent omniphilicity of the PEI, that has a hydrophobic backbone bearing amine groups that interact strongly with water. Functionalization of the sponge with alkyl chains of variable chain length affords materials with controllable affinity for polar or apolar solvents. Modification with a C4 chain results in a remarkable material that can absorb 12 times its weight of either water or hexane. Modification with longer alkyl chains results in more hydrophobic sponges. Modification with a C17 chain results in a sponge that can absorb 15 times its weight in hexane or 5 times its weight in water. This sponge is hydrophobic in the dry state and retains its oleophilicity underwater. Even a water-saturated C17-modified sponge is able to absorb hexane from a hexane-water mixture. Modified and unmodified sponges are able to separate hexane from either anionic or cationic surfactant stabilized emulsions.

These sponges are stable to several hundred compression-expansion cycles. The unmodified sponge and sponges modified with C4 and C8 chains recover from up to 80% compressive strains. C17 modified sponges can repeatedly compressed to 60% strain without failing. Thus, the sponges can be compressed for easy recovery of absorbed solvent and can be subsequently reused.

These sponges are easy to prepare and use an inexpensive, commercially available starting polymer, polyethyleneimine, as the matrix. Ice templating, the process used to create the macroporous monoliths is versatile process and is amenable to process modifications to vary[49-51]the pore size and orientation. Facile chemical modification allows us to tailor-make sponges that are either hydrophilic, omniphilic or hydrophobic. Remarkably, the hydrophobic sponges retain their oleophilicity underwater. These materials have potential for use as absorbents for a wide variety of solvent spills.

4.6 References

(1)http://www.acs.org/content/acs/en/about/governance/committees/chemicalsafety/publications/guide-for-chemical-spill-response.html

(2) Adebajo, M. O.; Frost, R. L.; Kloprogge, J. T.; Carmody, O.; Kokot, S., Porous materials for oil spill cleanup: a review of synthesis and absorbing properties. *J. Porous Mater.* **2003**, 10, 159-170.

(3) Sakthivel, T.; Reid, D. L.; Goldstein, I.; Hench, L.; Seal, S., Hydrophobic High Surface Area Zeolites Derived from Fly Ash for Oil Spill Remediation. *Energy Environ. Sci.* **2013,** 47, 5843-5850.

(4) Shawky, H. A.; El-Sayed, M. H.; Ali, A. E.-H.; Abdel Mottaleb, M. S., Treatment of polluted water resources using reactive polymeric hydrogel. *J. Appl. Polym. Sci.* **2006,** 100, 3966-3973.

(5) Akhavan, B.; Jarvis, K.; Majewski, P., Hydrophobic Plasma Polymer Coated Silica Particles for Petroleum Hydrocarbon Removal. *ACS Appl. Mater. Interfaces* **2013,** 5, 8563-8571.

(6) Reynolds, J. G.; Coronado, P. R.; Hrubesh, L. W., Hydrophobic aerogels for oil-spill clean up-Synthesis and characterization. *J. Non-Cryst. Solids* **2001**, 292, 127-137.

(7) Mysore, D.; Viraraghavan,T.; Jin, Y. C., Treatment of oily waters usingvermiculite. *Water Res.* **2005,** 39, 2643-2653.

(8) Oikawa, Y.; Saito, T.; Yamada, S.; Sugiya, M.; Sawada, H., Preparation and Surface Property of Fluoroalkyl End-Capped Vinyltrimethoxysilane Oligomer/Talc Composite-Encapsulated Organic Compounds: Application for the Separation of Oil and Water. *ACS Appl. Mater* **2015,** 7, 13782-13793.

(9) Yang, C.; Kaipa, U.; Mather, Q. Z.; Wang, X.; Nesterov, V.; Venero, A. F.; Omary, M. A., Fluorous metal-organic frameworks with superior adsorption and hydrophobic properties toward oil spill cleanup and hydrocarbon storage. *J. Am. Chem. Soc.* **2011,** 133, 18094-18097.

(10) Alsbaiee, A.; Smith, B. J.;Xiao, L.; Ling, Y.; Helbling, D. E.; Dichtel, W. R., Rapid removal of organic micropollutants from water by a porous β-cyclodextrin polymer. *Nature* **2015,** 529, 190-194.

(11) Wang, S.; Peng, X.; Zhong, L.; Tan, J.; Jing, S.; Cao, X.; Chen, W.; Liu, C.; Sun, R., An ultralight, elastic, cost-effective, and highly recyclable superabsorbent from microfibrillated cellulose fibers for oil spillage cleanup. *J. Mater. Chem. A* **2015,** 3, 8772-8781.

(12) Wang, J.; Zheng, Y.; Wang, A., Effect of kapok fiber treated with various solvents on oil absorbency. *Industrial Crops and Products* **2012,** 40, 178-184.

(13) Zhang, Z.; Sèbe, G.; Rentsch, D.; Zimmermann, T.; Tingaut, P., Ultralightweight and Flexible Silylated Nanocellulose Sponges for the Selective Removal of Oil from Water.*Chem. Mater.* **2014,** 26, 2659-2668.

(14) Wang, G.; He, Y.; Wang, H.; Zhang, L.; Yu, Q.; Peng, S.; Wu, X.; Ren, T.; Zeng, Z.; Xue, Q., A cellulose sponge with robust superhydrophilicity and under-water superoleophobicity for highly effective oil/water separation. *Green Chem.* **2015,** 17, 3093-3099.

(15) Li, A.; Sun, H.-X.; Tan, D.-Z.; Fan, W.-J.; Wen, S.-H.; Qing, X.-J.; Li, G.-X.; Li, S.-Y.; Deng, W.-Q., Superhydrophobic conjugated microporous polymers for separation and adsorption. *Energy Environ. Sci.* **2011,** 4, 2062-2065.

(16) Wang, F.; Lei, S.; Li, C.; Ou, J.; Xue, M.; Li, W., Superhydrophobic Cu Mesh Combined with a Superoleophilic Polyurethane Sponge for Oil Spill Adsorption and Collection.*Ind. Eng. Chem. Res.* **2014,** 53, 7141-7148.

(17) Pan, Y.; Shi, K.; Peng, C.; Wang, W.; Liu, Z.; Ji, X., Evaluation of hydrophobic polyvinyl-alcohol formaldehyde sponges as absorbents for oil spill. *ACS Appl. Mater. Interfaces* **2014,** 6**,** 8651-8659.

(18) Ruan, C.; Ai, K.; Li, X.; Lu, L., A superhydrophobic sponge with excellent absorbency and flame retardancy. *Angew. Chem. Int. Ed.* **2014,** 53, 5556-5560.

(19) Zhu, Q.; Pan, Q.; Liu, F., Facile removal and collection of oils from water surfaces through superhydrophobic and superoleophilic sponges. *J. Phys. Chem. C* **2011,** 115, 17464-17470.

(20) Zhang, J.; Seeger, S., Polyester materials with superwetting silicone nanofilaments for oil/water separation and selective oil absorption. *Adv. Funct. Mater* **2011,** 21, 4699-4704.

(21) Bayat, A.; Aghamiri, S. F.; Moheb, A.; Vakili-Nezhaad, G. R., Oil spill cleanup from sea water by sorbent materials.*Chem. Eng. Technol.* **2005,** 28, 1525-1528.

(22) Choi, S.-J.; Kwon, T.-H.; Im, H.; Moon, D.-I.; Baek, D. J.; Seol, M.-L.; Duarte, J. P.; Choi, Y.-K., A polydimethylsiloxane (PDMS) sponge for the selective absorption of oil from water. *ACS Appl. Mater. Interfaces* **2011,** 3, 4552-4556.

(23) Zhang, A.; Chen, M.; Du, C.; Guo, H.; Bai, H.; Li, L., Poly (dimethylsiloxane) oil absorbent with a three-dimensionally interconnected porous structure and swellable skeleton. *ACS Appl. Mater. Interfaces* **2013,** 5,10201-10206.

(24) Hersey, J. S.; Yohe, S. T.; Grinstaff, M. W., Poly (ε-caprolactone) microfiber meshes for repeated oil retrieval.*Environ. Sci.: Water Res. Technol.* **2015,** 1, 779-786.

(25) Hayase, G.; Kanamori, K.; Fukuchi, M.; Kaji, H.; Nakanishi, K., Facile synthesis of marshmallow-like macroporous gels usable under harsh conditions for the separation of oil and water. *Angew. Chem. Int. Ed.* **2013,** 52, 1986-1989.

(26) Zhou, X.; Wang, F.; Ji, Y.; Wei, J., Fabrication of unidirectional diffusion layer onto polypropylene (PP) mat for oil spill cleanup. *Ind. Eng. Chem. Res.* **2015,** 54**,** 11772–11778.

(27) Gui, X.; Wei, J.; Wang, K.; Cao, A.; Zhu, H.; Jia, Y.; Shu, Q.; Wu, D., Carbon nanotube sponges. *Adv. Mater.* **2010,** 22, 617-621.

(28) Gao, Y.; Zhou, Y. S.; Xiong, W.; Wang, M.; Fan, L.; Rabiee-Golgir, H.; Jiang, L.; Hou, W.; Huang, X.; Jiang, L.; Silvain, J.-F.; Lu, Y. F., Highly Efficient and Recyclable Carbon Soot Sponge for Oil Cleanup. *ACS Appl. Mater. Interfaces* **2014,** 6, 5924-5929.

(29) Leventis, N.; Chidambareswarapattar, C.; Bang, A.; Sotiriou-Leventis,C., Cocoon-in-Web-Like Superhydrophobic Aerogels from Hydrophilic Polyurea and Use in Environmental Remediation. *ACS Appl. Mater. Interfaces* **2014**, 6, 6872-6882.

(30) Sun, H.; Xu, Z.; Gao, C., Multifunctional, ultra-flyweight, synergistically assembled carbon aerogels. *Adv. Mater.* **2013,** 25, 2554-2560.

(31) Xue, Z.; Cao, Y.; Liu, N.; Feng, L.; Jiang, L., Special wettable materials for oil/water separation. *J. Mater. Chem. A* **2014,** 2, 2445-2460.

(32) Sun, T.; Feng, L.; Gao, X.; Jiang, L., Bioinspired surfaces with special wettability. *Acc. Chem. Res.* **2005,** 38, 644-652.

(33) Kwon, G.; Kota, A.; Li, Y.; Sohani, A.; Mabry, J. M.; Tuteja, A., On-Demand Separation of Oil-Water Mixtures. *Adv. Mater.* **2012,** 24, 3666-3671.

(34) Yabu, H.; Takebayashi, M.; Tanaka, M.; Shimomura, M., Superhydrophobic and lipophobic properties of self-organized honeycomb and pincushion structures. *Langmuir* **2005,** 21, 3235-3237.

(35) Song, J.; Huang, S.; Lu, Y.; Bu, X.; Mates, J. E.; Ghosh, A.; Ganguly, R.; Carmalt, C. J.; Parkin, I. P.; Xu, W., Self-Driven One-Step Oil Removal from Oil Spill on Water via Selective-Wettability Steel Mesh. *ACS Appl. Mater. Interfaces* **2014,** 6, 19858-19865.

(36) Tuteja, A.; Choi, W.; Ma, M.; Mabry, J. M.; Mazzella, S. A.; Rutledge, G. C.; McKinley, G. H.; Cohen, R. E., Designing superoleophobic surfaces. *Science* **2007,** 318, 1618-1622.

(37) Tuteja, A.; Choi, W.; Mabry, J. M.; McKinley, G. H.; Cohen, R. E., Robust omniphobic surfaces. *Proc. Nat. Acad. Sc. U. S.A.* **2008,** 105, 18200-18205.

(38) Tao, M.; Xue, L.; Liu, F.; Jiang, L., An intelligent superwetting PVDF membrane showing switchable transport performance for oil/water separation. *Adv. Mater.* **2014,** 26, 2943-2948.

(39) Deville, S., Ice-templating, freeze casting: Beyond materials processing. *J. Mater. Res.* **2013,** 28, 2202-2219.

(40) Gutiérrez, M. a. C.; Ferrer, M. a. L.; del Monte, F., Ice-Templated Materials: Sophisticated Structures Exhibiting Enhanced Functionalities Obtained after Unidirectional Freezing and Ice-Segregation-Induced Self-Assembly. *Chem. Mater.* **2008,** 20, 634-648.

(41) Dagalakis, N.; Flink, J.; Stasikelis, P.; Burke, J. F.; Yannas, I. V., Design of an artificial skin. Part III. Control of pore structure. *J. Biomed. Mater. Res.* **1980,** 14, 511-528.

(42) Chen, G.; Ushida, T.; Tateishi, T., Preparation of poly (L-lactic acid) and poly (DL-lactic-co-glycolic acid) foams by use of ice microparticulates. *Biomaterials* **2001,** 22, 2563-2567.

(43) Ho, M.-H.; Kuo, P.-Y.; Hsieh, H.-J.; Hsien, T.-Y.; Hou, L.-T.; Lai, J.-Y.; Wang, D.-M., Preparation of porous scaffolds by using freeze-extraction and freeze-gelation methods. *Biomaterials* **2004,** 25, 129-138.

(44) Hsieh, C.-Y.; Tsai, S.-P.; Ho, M.-H.; Wang, D.-M.; Liu, C.-E.; Hsieh, C.-H.; Tseng, H.-C.; Hsieh, H.-J., Analysis of freeze-gelation and cross-linking processes for preparing porous chitosan scaffolds. *Carbohydr. Polym.* **2007,** 67, 124-132.

(45) Ricciardi, R.; Auriemma, F.; De Rosa, C. In *Structure and properties of poly (vinyl alcohol) hydrogels obtained by freeze/thaw techniques*, *Macromol.Symp.* **2005**, 222, 49-64.

(46) Rajamanickam, R.; Kumari, S.; Kumar, D.; Ghosh, S.; Kim, J. C.; Tae, G.; Sen Gupta, S.; Kumaraswamy, G., Soft colloidal scaffolds capable of elastic recovery after large compressive strains. *Chem. Mater.* **2014,** 26, 5161-5168.

(47) Kovscek, A. R.; Wong, H.; Radke, C. J., A pore-level scenario for the development of mixed wettability in oil reservoirs. *AIChE Journal* **1993,** 39, 1072-1085.

(48) Hui, M.-H.; Blunt, M. J., Effects of wettability on three-phase flow in porous media. *J. Phys. Chem. B* **2000,** 104, 3833-3845.

(49) Song, J. H.; Koh, Y. H.; Kim, H. E.; Li, L. H.; Bahn, H. J., Fabrication of a Porous Bioactive Glass-Ceramic Using Room-Temperature Freeze Casting. *J. Am. Ceram. Soc.* **2006,** 89, 2649-2653.

(50) Deville, S., Freeze-casting of porous biomaterials: structure, properties and opportunities. *Materials* **2010,** 3, 1913-1927.

(51) Munch, E.; Saiz, E.; Tomsia, A. P.; Deville, S., Architectural Control of Freeze-Cast Ceramics Through Additives and Templating. *J. Am. Ceram. Soc.* **2009,** 92, 1534-1539.

Capillary Uptake in Macroporous Compressible Sponges

In this chapter we studied capillarity driven uptake of liquid in swellable, highly porous sponges that have significant industrial importance. We report experiments that study capillary uptake in a variety of flexible, centimetre-sized macroporous cylindrical sponges. Ice-templating is used to prepare a series of model macroporous sponges where the porosity, modulus and composition are systematically varied. Two kinds of sponges are investigated: (a) those comprised purely of cross-linked polymer and (b) those prepared as composites of inorganic particles and polymer. Both kinds of sponges are flexible and exhibit elastic recovery after large compressive deformation. All sponges were characterized thoroughly with respect to their pore microstructure and elastic modulus. When one end of the sponge is plunged into a large reservoir, water rises through capillary action, against gravity. A transition from an inertial-capillary regime is observed where the liquid column height rises linearly with time, t, to a viscous-capillary regime where the liquid height rises with $t^{0.5}$. It is shown that these results can be rationalized using analyses developed for rigid sponges. Differential momentum balance equations for uptake in rigid capillaries are combined with the phenomenological Ergun-Forchheimer relations to account for the effect of sponge microstructure. This approach works remarkably well in the viscous capillary regime and shows that capillary uptake is governed primarily by the total porosity and pore dimensions of the soft sponges.

5.1 Introduction

Macroporous sponges have pore dimensions that are at least several tens of microns, and are typically characterized by large void volume and an interconnected pore structure. Macroporous sponges have been prepared using several techniques, including sol-gel chemistry,[1] by using fibrous elements,[2–5] by foaming polymers such as polyurethanes or by employing sacrificial templates.[6–9] Such sponges find use in a wide variety of applications. For example, ceramic foams are often used as low pressure drop catalyst supports[10] in catalytic combustion devices. An industrially important use for macroporous sponges (ranging from common kitchen sponges to carbon nanotube based sponges[11]) is in the absorption of liquids. Ideally, sponges used for solvent absorption should recover elastically from large compression so that the sponges can be reused after recovery of absorbed solvent by squeezing. Recently, significant advances in the materials chemistry of macroporous sponges have enabled the preparation of elastic, lightweight materials that are tuned to absorb apolar oils and that have extremely high solvent uptake capacities.[12,13] For example, carbon soot, carbon nanotube and graphene based aerogels[14,15] have been reported, some of which exhibit oil absorption capacities exceeding 900-fold on a weight/weight basis. Recyclable macroporous polymer sponges based on melamine-formaldhyde,[16] polyvinylalcohol,[17] polydimethylsiloxanes[18–20] etc. have also been reported. In the previous chapter, the preparation of a family of polyethyleneimine (PEI) based omniphilic sponges was described, that are capable of absorbing solvents of varying polarity (ranging from water to hexane) as well as oils emulsified using surfactants. These omniphilic sponges were prepared by freezing aqueous solutions of PEI and diepoxide cross-linker, using a process termed ice templating, where ice crystals act as templates for the porous structure. Ice templating is a versatile process and affords a convenient route to prepare sponges with variable wall composition, volume porosity as well as pore size and orientation.[21–23] Therefore, it offers the possibility of engineering sponge architecture to optimize the kinetics of solvent uptake. Here, we investigate the uptake of solvent into ice-templated macroporous sponges and examine the effect of systematic variation of sponge characteristics on the kinetics of solvent uptake.

The kinetics of solvent uptake into rigid, porous materials is a classic problem in fluid mechanics. One of the earliest descriptions is due to Washburn[24] who modelled these materials as comprising of parallel cylindrical tubes without interconnections. Capillary rise

through these tubes was modelled as Poiseuille flow, so that the rise height scales as the square root of the flow time ($h \sim t^{0.5}$). Delker et al.[25], Lago and Araujo[26]and Miller et al.[27]experimentally investigated the kinetics of capillary rise of water through a packed bed of glass beads. They observed an initial ($h \sim t^{0.5}$) Washburn region, followed by a distinctly different regime at later times. They observed that at longer times, the height of advancing liquid front scaled with $t^{0.25}$. Siebold et al.[28] investigated capillary rise through packed beds of solid particles in the Washburn regime and demonstrated that these experiments could be used to estimate the surface energy of particles comprising the packing. Fries et al.[29] discussed the initial stage of capillary rise and demonstrated that there is an initial inertial regime (where inertial losses determine the rise rate) that transitions through a visco-inertial regime to a final viscous regime, where viscous losses dominate. Marmur et al.[30] studied kinetics of liquid penetration in a filter paper strip and in a sand bed and demonstrated that this could be modeled as flow through parallel capillaries. Pezron et al.[31] investigated capillary rise in cotton fabric and have demonstrated that liquid uptake can be modeled using the Washburn formalism only if we assume a bimodal distribution of capillary sizes.

Ingress of liquids into deformable media has also received attention from researchers. For example, Preziosi et al.[32] investigated infiltration of initially dry media that is deformed by the forces due to imbibition of liquid. They assumed plug-like Darcy flow of the liquid through the porous media and assumed a variety of constitutive models for the response of the wet porous media. Roman and Bico[33] have reviewed elastocapillary flows where capillary interactions can elastically deform channels formed by slender hair-like structures. The dynamics of pressure driven capillary flow in planar nano-channels with one flexible wall was studied by van Honschoten et al.[34] Cambau et al.[35] studied capillary rise between two sheets and demonstrated continuous rise of a finger-like front of liquid. Aristoff et al. examined filling of a capillary gap between long, thin flexible sheets separated by a spacer at the point of liquid entry.[36,37] They demonstrated that negative pressure causes inward deflection of the sheets leading to a non-monotonic rise of the liquid. They reported classical Washburn-like capillary imbibition at early times when there is negligible deflection of the walls. However, at later times, they observed an acceleration of the flow due to inward deflection of the sheets, followed by a closure of the gap at the meniscus. Dreyer et al. presented capillary rise of a perfectly wetting liquid into circular cylindrical tubes under conditions of microgravity.[29,38,39] They proposed a mathematical model which predicts a variation in the time dependence of the rise height as the capillary driving force is opposed

first by inertial, then viscous, and finally convective losses. Recently, Siddiqui et al.[40] presented numerical solutions for a model of capillary rise in deformable media and demonstrated a transition from an initial $t^{0.5}$ scaling for the rise height to a $t^{0.22}$scaling, similar to the $t^{0.25}$scaling observed for rigid porous materials. They also presented experimental validation of their results using a kitchen sponge as a model system. However, it should be noted that the kitchen sponge did not exhibit large swelling.

While there are several reports of flow through rigid as well as deformable porous media, there are no reports that probe the effect of systematic variation in properties of the porous medium on the kinetics of solvent uptake. Given the large variety of sponges that are being developed for solvent absorption applications, it is important to develop a thorough understanding of how sponge characteristics influence the kinetics of solvent uptake. The ice templated macroporous sponges developed at NCL[41] afford systematic variation of sponge characteristics and represent model systems for such studies. Here, we investigate capillary imbibition of water in two series of macroporous sponges prepared by ice templating: (i) hybrid sponges comprised predominantly (~ 80% w/w) of inorganic silica colloids enmeshed in a cross-linked PEI matrix and (ii) sponges comprised only of cross-linked PEI. An experimental investigation including the preparation of the sponges, visualization of capillary rise and analysis of the video data of capillary rise in the hybrid and polymer sponges is reported in this chapter.

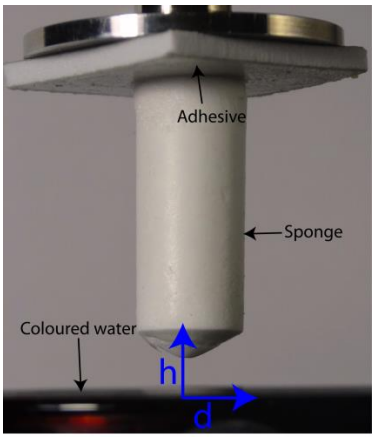

Figure 5.1: Experimental set up to investigate water imbibition. A lyophilized macroporous sponge is attached to a top plate with adhesive and is plunged into a bath containing dyed water along h-coordinate as defined in the set up.

5.2 Experimental

5.2.1 Materials:

Polyethylenimine (PEI) and 1,4-butanediol diglycidyl ether were obtained from Sigma Aldrich and were used as received. PEI has a molecular weight, M_w = 750 kDa, as specified by the supplier. PEI has a branched chain architecture that is previously characterized.[43]"Angstrom Sphere "silica particles with a diameter of 1 micron were obtained from Richen Industry Limited, Hong Kong. Distilled deionized water (resistivity ~ 18.2 MΩ.cm) was obtained from a Millipore MilliQ unit and was used to prepare sponges. Rhodamine B dye was obtained from Loba Chemicals.

5.2.2 Fabrication of composite sponges by ice templating:

Composite sponges are prepared using a previously reported protocol (Section 2.2.2). Typically, 120 mg of silica particles was dispersed in 1060 μL of water by sonication for 15 min (corresponding to a concentration of 10% w/v). To this aqueous particle dispersion, 24 mg (120 μL of 200 mg/ml stock solution) of PEI (750 kDa, a cationic polymer) was added, and the mixture was vortexed for 10 min. PEI adsorbs on the silica surface via electrostatic interactions. To this polymer-coated silica particle dispersion, 20 μL of 1,4-butanediol diglycidyl ether was added. Then the sample was immediately transferred to a freezer maintained at −15°C, and was stored in the freezer for 24 h, to allow reaction between the PEI amine groups and the 1,4-butanediol diglycidyl ether to proceed. After that, the sponge was removed from the freezer and lyophilized at -90°C for 12h to sublime the ice. This sponge was named S10 (corresponding to the 10% w/v concentration of silica particles in the ice-templated aqueous dispersion). The sponge is cylindrical in shape with a diameter of approximately 8 mm, and takes the shape of the centrifuge tube in which it is prepared. Similarly, we prepared composite sponges from aqueous dispersions containing 20% and 30% (w/v) silica particles, maintaining the same ratio of inorganic to organic, and with the same ratio of PEI to 1,4-butanediol diglycidyl ether. These monoliths are termed S20 and S30, respectively. All sponges are prepared in identical centrifuge tubes.

5.2.3 Preparation of cross-linked polymer sponges:

To prepare polymer sponges, the protocol reported in the previous chapter (Section 2.2.3) is followed. In one example, 1060 μL of water and 24 mg (120 μL of 200 mg/ml stock solution)

of PEI (750 kDa) were vortex mixed for 10 min (3% w/v of the PEI). To this polymer solution, 20 µL of 1,4-butanediol diglycidyl ether was added. The solution was transferred into a freezer at −15°C and kept for 24 h at this temperature for completion of reaction. After 24 h, the sponge was dried by lyophilization at -90°C for 12 h. We term this sponge Sp3. Similarly, we prepare monolith sponges from 7% and 10% (w/v) PEI aqueous solutions, maintaining the ratio of PEI to cross-linker. These are termed as Sp7 and Sp10, respectively.

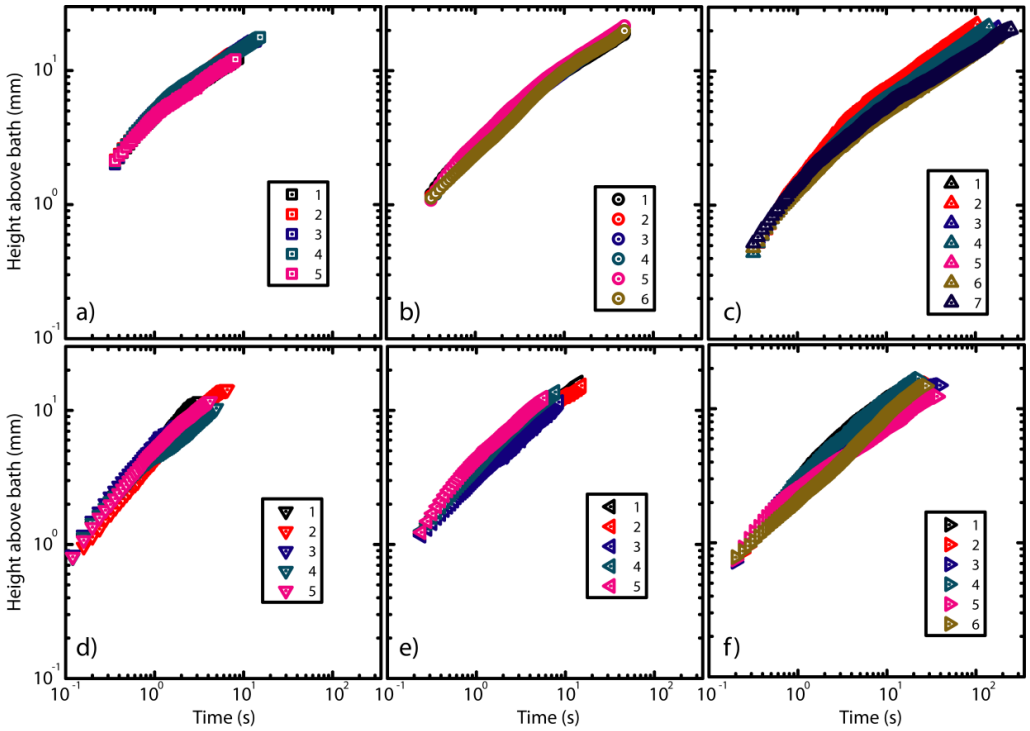

Figure 5.2: Plot of capillary rise height of water above the water bath for a) S10, b) S20, (c) S30, (d) Sp3, (e) Sp7 and (f) Sp10 sponges respectively with at least 5 repetition.

5.2.4 Capillary rise experiments:

The experimental set up for the study of water uptake kinetics is shown in Figure 5.1. We use double-sided adhesive tape to adhere the flat top face of a lyophilized cylindrical sponge to a plate. To initiate the experiment, the plate is moved downward at constant velocity (=5 mm/s) to carefully immerse the tip of the sponge into a fixed bath of Milli-Q water, to which a cationic dye, Rhodamine B is added to enhance the contrast of the flow front in capillary uptake experiments. Rhodamine B at a concentration = 9.6 mg/ml is added. This does not change the density or the viscosity of water substantially but reduces the surface tension to σ = 63.5±0.2 mN/m. The capillary length for the coloured water is $\lambda_c = \sqrt{\sigma/(\rho g)}$ = 2.5 mm,

where σ is surface tension and ρ is density of liquid. The walls of both composite and polymeric sponges contain an amine containing polymer, PEI. Therefore, there is no attractive interaction between the sponge walls and cationic Rhodamine B dye. Typically, the tip is plunged into the water bath to a depth of about 1 mm and capillary rise of water into the sponge is observed from the side using a video camera at 25 fps (Sony DSC-HX20V). All the experiments are carried out at room temperature (25°C). Experiments for each kind of sponge were repeated at least five times, on independent sponge samples, to ensure repeatability of data (Figure 5.2). Data presented here is from one representative experimental run.

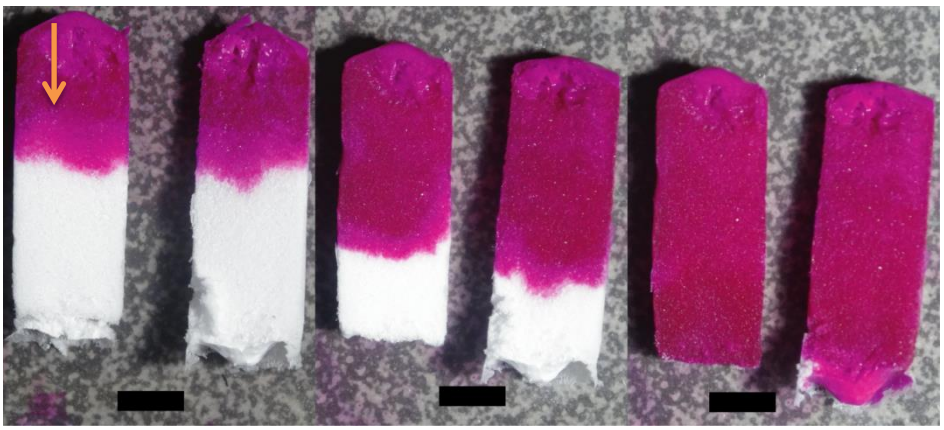

Figure 5.3: Images of sponges at various stage of capillary rise experiment. Arrow indicates flow direction. Scale bars in the photographs correspond to 5 mm.

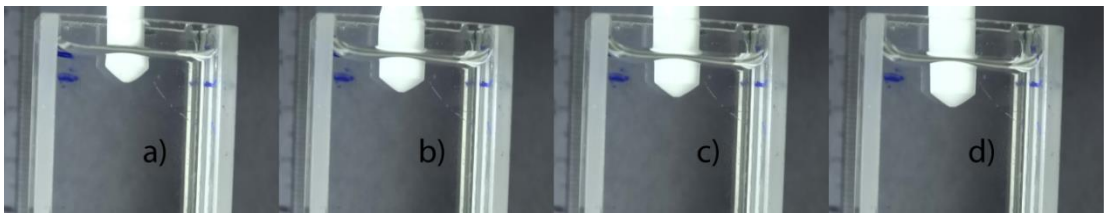

Figure 5.4: Images of axial growth of the sponge inside the reservoir of Sp10 with time, as the sponge swells when water is imbibed by it: a) t=0 s, b) t=4 s, c) t=8 s and d) t=12 s.

As the water rises, the sponge turns red and the height of the water can be readily observed. We use a large water bath; therefore, there is almost no change in the water level in the bath during the capillary uptake experiment. Sponges are examined at various stages of the capillary rise experiment. We cut the sponges and observe there is no radial variation (at length scales larger than the sponge pore size) as the dye front rises through the sponge (Figure 5.3). Thus, the water level rises approximately uniformly across the cross-section of the cylinder (along the h-co-ordinate defined in Figure 5.1). The sponges exhibit a volume

change on water absorption. There is an increase in both the diameter and the length of the sponges as they imbibe water. The increase in sponge diameter is readily estimated from videos of the capillary rise experiment. As the top of the cylindrical sponge is held fixed, there is an increase in the length of the sponge that is submerged within the water reservoir as the sponge imbibes water. This increase in length of the submerged sponge is measured by performing independent experiments to visualize this. The increase in axial length with time during the water imbibition experiment is shown in Figure 5.4. It can be noted that these experiments were performed using MilliQ water, since it is not possible to visualize the sponge once it is immersed in dyed water. The increase in submerged length inside the reservoir is significantly smaller when compared with the front height above the surface of the reservoir, at any point during the capillary uptake experiment. Therefore, it is anticipated that the error resulting from performing this measurement using MilliQ water (instead of dyed water) is small. Here, we report the height of the front as a sum of the front height above the reservoir and the change in length within the reservoir (Figure 5.5).

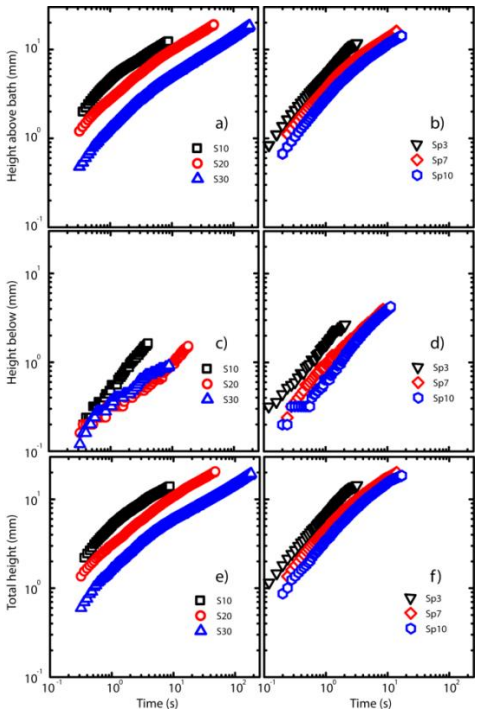

Figure 5.5: Plot of capillary rise height of water above the water bath for a) composite and b) polymeric sponges. Axial growth of composite and polymeric sponges inside the water reservoir are shown in the panel c) and d) respectively. e) and f) show the total length of the sponge that has imbibed water for composite and polymeric sponges respectively.

Capillary uptake experiments are performed using cylindrical sponges with a conical tip (Figure 5.1). The conical tip geometry is a replica of the bottom of the centrifuge tube in which the sponge is synthesized. We note that this shape helps minimize splashing as the bottom tip of the sponge is plunged into the water bath. However, water uptake is not influenced by the geometry. Comparative water uptake experiments for an "as prepared" S10 sponge with one where the conical section at the bottom of the sponge was cut to create a cylinder with a flat bottom surface showed no significant differences between the water uptake measurements for these two sponges (Figure 5.6).

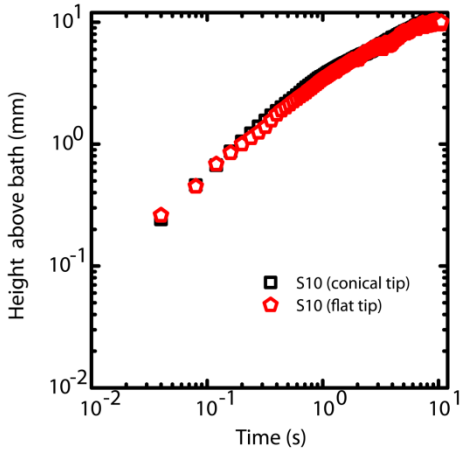

Figure 5.6: Comparison of capillary rise behaviour for S10 (conical tip) and S10 (flat tip)

As a control, water uptake is also studied with that in a rigid, relatively low porosity chalk. A cylindrical, colored chalk (Kores, India) is used for this experiment since it allows to readily observing the rise front as it imbibes water. Dyed water could not be used for the uptake experiments with chalk since the dye adsorbs on the chalk and does not track the rising water front. However, when a colored chalk is being used the water front wets the chalk as it propagates, and can be clearly observed.

5.2.5 Image Analysis

Image analysis is performed using code written in Python. A clear contrast between the red front (where the sponge has imbibed coloured water) and the white dry sponge can be observed as the dyed water rises up in the sponge. The edge of the red region of the sponge is tracked as a function of time to quantitate the dyed of water. The growth front for water ingress is typically jagged, but is approximately horizontal. The jagged growth front is

averaged and the height of this growth front from the water surface is determined as the height of water column in the sponge (Figure 5.7).

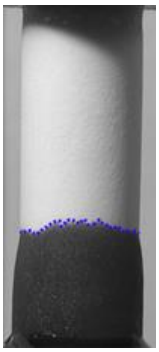

Figure 5.7: The jagged growth front of the colored water front, as it propagates, is averaged and the height of this growth front from the water surface is determined. Here, the front is shown as a blue dotted line.

5.3 Characterization

The morphology of the porous sponges was imaged using a Quanta 200 3D scanning electron microscope as discussed in section 2.4.1. The mechanical response of the sponges was characterized using a TA instruments DMA (RSA-III), equipped with a normal force transducer. Three-dimensional non-destructive imaging of macroporous sponges was performed at the SreeChithraTirunal Institute for Medical Sciences and Technology, Thiruvananthapuram (India) using a high-resolution X-ray microcomputed tomography (μ-CT, model μ-CT 40, Scanco Medical AG, Switzerland). Centimeter size large sponges were scanned using X-ray of energy 45 kV, at (12 μm^3) voxel resolution. Two-dimensional cross-sectional images of the sponges were thresholded to suppress background noise, and the region of interest was marked to discriminate between walls as well as pores in the sponges. The 2D images were compiled, and 3D images of respective sponges were generated using the software provided by the manufacturer. Micro-architectural parameters of the sponges such as pore size and wall thickness distribution were evaluated by applying the distance transformation methodology with the aid of the software supplied by the manufacturer.

5.4 Results and Discussion

5.4.1 Structural Characterization of Macroporous Sponges:

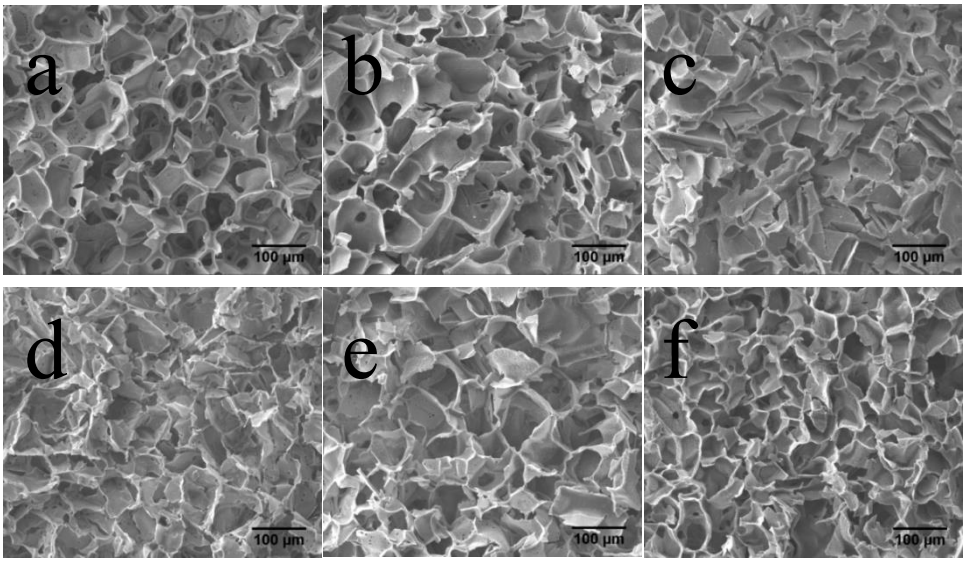

Figure 5.8: SEM micrograph of sponges. (a-c) composite sponges S10, S20 and S30 respectively. (d-f) polymer crosslinked sponges Sp3, Sp7 and Sp10 respectively. Images indicate macro porosity.

SEM images of lyophilized sponges reveal an interconnected macroporous structure (Figure 5.8 a-f). A typical three dimensional rendering using the µ-CT data is shown in Figure 5.9. X-ray micro-tomography provides details of the pore size distribution and peak wall thickness of the sponges in the lyophilized, dry state (Figure 5.10). With increase in concentration of the ice-templated dispersion, the mean pore size decreases and the width of the pore size distribution narrows. The mean pore size decreases from 108 µm for S10 to 72 µm and 48 µm for S20 and S30, respectively and from 84 µm to 72 µm and 48 µm for Sp3, Sp7 and Sp10 respectively. We estimate porosity of the sponges with in the completely wet state by saturating them in water for 6h. The porosity is obtained from measuring the weight of the water present in the wet sponge (and using density of water at 25°C = 997 kg/m3) and the measured volume of the wet cylindrical sponge. The cross-linked polymer sponges show higher porosity relative to the composite sponges. Sp3 shows the highest porosity ≈ 98%. While the peak pore size of Sp3 from the X-ray tomography data is less than that for S10, the cross-linked polymer sponges exhibit greater swelling in water and, therefore, exhibit higher volume porosity in the wet state. The porosity of Sp7 and Sp10 is estimated as 83 and 77%

respectively. Composite sponges have a lower porosity and we measure porosities of 86, 78

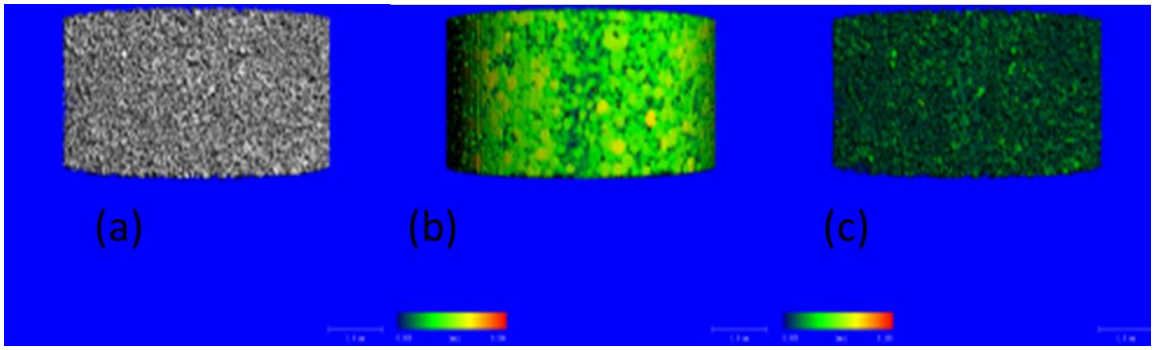

Figure 5.9: Typical X-ray µ-CT images use to estimate pore size distribution, wall thickness and porosity of sponges. False color is used to render (a) the sponge; (b) the pores and (c) the walls. Colour coding represents length scale of pores and wall thickness for (b) and (c) respectively.

and 66%, respectively, for S10, S20 and S30.

The elastic modulus (E') of the sponges is measured in compression, to quantify their mechanical response. In all samples – including polymeric and composite sponges, the ratio of polymer (PEI) to cross-linker (diepoxy) is maintained constant. Both polymeric and hybrid

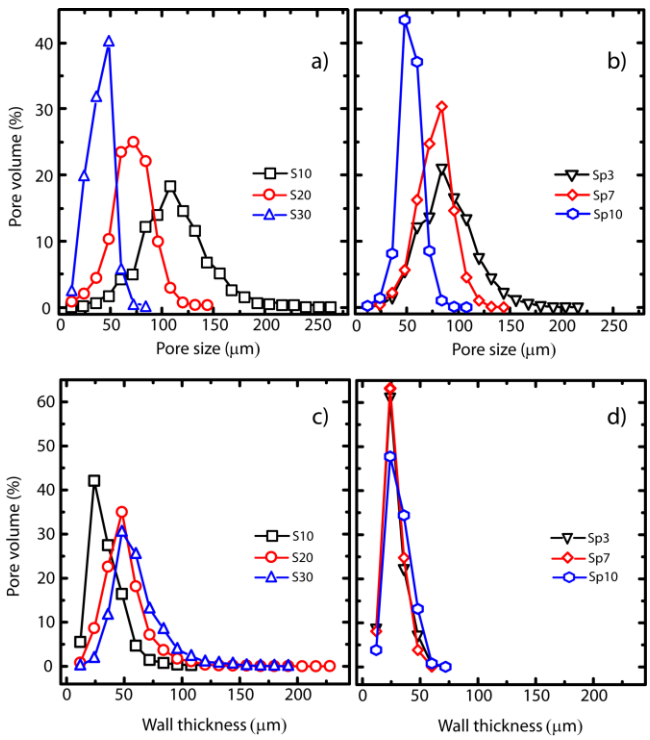

Figure 5.10: Pore size distribution (a-b) and peak pore wall thickness (c-d) for composite and polymeric sponges.

sponges exhibit an initial linear response, followed by a large, nonlinear increase in stress for large compressive strains. Data is presented here for the elastic modulus of sponges saturated with water as a slope of the linear stress-strain region (Figure 5.11). We noticed that elastic modulus of the sponges increases monotonically with decreasing porosity for both polymeric and hybrid sponges (Figure 5.11). The modulus values observed are relatively low, of the order of 10^4 to 10^5 Pa, indicating that these sponges are soft. Even for the composite sponges, where the particle content is of the order of 80%, the elastic modulus in the linear response regime is governed largely by the cross-linked polymer mesh surrounding the colloidal particles.[41] However, remarkable differences (that are not evident from the variation in E') can be observed between polymeric and composite sponges during drying. When polymeric sponges saturated with water are dried, the capillary forces experienced result in dramatic shrinkage and change in shape of the sponges (Photographs Figure 5.12). In contrast, composite sponges are able to better withstand the compressive force generated due to drying and there is relatively lower volume shrinkage between the wet and dry states.

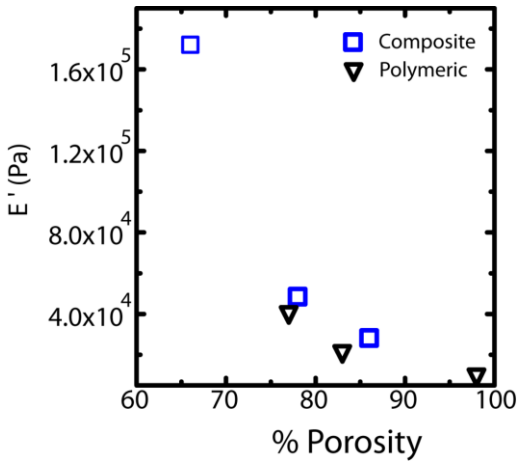

Figure 5.11: Elastic modulus of composite and crosslinked sponges is plotted against porosity. Modulus increases with decrease in porosity for a class of sponges.

5.4.2 Analysis of swelling behaviour:

On immersion in water, the sponges swell. Both composite and polymeric sponges comprise cross-linked polymer PEI. PEI is water soluble and cross-linked PEI swells in the presence of water. Therefore, when the sponges are immersed, there is water ingress into the pores and this water also swells the cross-linked polymer in the walls of the sponge. This results in macroscopic swelling of the sponge. To estimate the extent of swelling, the diameter and length of the sponges are measured using a Vernier scale in dry and completely water soaked states. Change in diameter (Δd) and length ($\Delta \ell$), is measured and normalized with their

respective dry diameter (d) and dry length (ℓ) to estimate swelling (Table 5.1). In the water uptake experiments, when one end of the sponge is dipped in the water reservoir, the swelling of the sponges can be estimated using image analysis. While there are some differences between these two estimates of swelling of the sponges, these differences are not systematic (Table 5.1). The approximate agreement between these estimates indicates that swelling of the sponges due to water imbibition is similar for isotropic swelling and for capillary uptake. Thus, the extent of swelling is a material property of the sponge and is independent of the mode of water imbibition. Composite sponges swell only ≈10% compare to polymeric sponges, that shows ≈20% swelling. Thus, the presence of the colloidal particles in the walls of the composite sponge prevents excessive swelling of the sponges and prevents the collapse of the sponge walls due to capillary forces during drying, Figure 5.12.

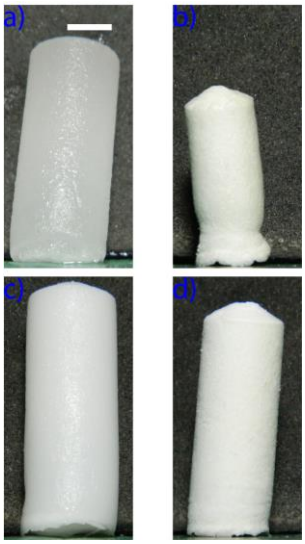

Figure 5.12: Photographs of polymeric sponge, Sp3 in (a) water swollen wet state and (b) in the dry state, after air drying. The polymer sponge shows large shrinkage after air drying. In contrast, there is significantly lesser shrinkage of composite sponges as they are air dried from the (c) water swollen wet state to (d) a dry state. The scale bar in (a) represents 5 mm and applies to all photographs.

5.4.3 Absorption kinetics of sponges:

Typically when a liquid is driven into a porous medium due to capillarity, a complex flow field develops within its pores. The wicking flow depends on geometrical and physical properties of the deformable porous medium and the physical properties of the liquid. Previous investigations have shown distinct regimes of capillary-driven flow in circular cylindrical tubes based on simple momentum balance equations.[39,43] Three regimes are

observed in experiments with dry chalk (a rigid, relatively low porosity material) viz. an initial $h \sim t$, that results from a balance between capillarity driven inertial flow and is referred to as inertial capillary (IC) regime (Figure 3.13). Subsequently, this linear regime transitions to the well-known Lucas-Washburn regime $h \sim t^{0.5}$ in which capillary force balances viscous dissipation (VC regime). Finally, at later times in the capillary flow

Table 5.1: Change in dimensions on swelling of sponges. Δd is the change in diameter from the initial dry diameter, d. Δ ℓ is the change in length where ℓ is the dry length.

Sponge	Change in sponge size when it is fully immersed in water		Water imbibition through capillary rise	
	Vernier scale		Image analysis	
	Δd/d	Δℓ /ℓ	Δd/d	Δℓ /ℓ
S10	0.09	0.05	0.12	0.08
S20	0.10	0.07	0.10	0.11
S30	0.11	0.03	0.10	0.09
Sp3	0.17	0.18	0.20	0.24
Sp7	0.18	0.16	0.22	0.22
Sp10	0.17	0.17	0.23	0.25

experiment, recent analysis and experiments have demonstrated the existence of slower uptake, where $h \sim t^{0.25}$. Recent work [40] using a compressible, porous kitchen sponge has shown evidence for the VC ($h \sim t^{0.5}$) and post VC, $h \sim t^{0.25}$regimes.

Photographs of water imbibition during capillary rise are shown in Figure 3.14 for S20 (as an example). The time t = 0 is set when the sponge contacts the water surface, and h = 0 mm as the position of the unperturbed water surface in the reservoir (Figure 3.14). When the dry sponge contacts water, there is ingress of water into the sponge. The water rises along the axis of the cylindrical sponge and fills the pore volume. Simultaneously, there is a swelling of the

sponge diameter, driven by the solvation and swelling of the cross-linked polymer, PEI in the sponge walls. There is a ≈10% increase in the diameter of the composite sponges and a larger, ≈17-18% increase in the diameter of the polymeric sponges on swelling in water. The lateral swelling of the sponges depends on the rate of water imbibition and happens over time scales that characterize uptake. Therefore, the kinetics of axial rise and lateral swelling cannot

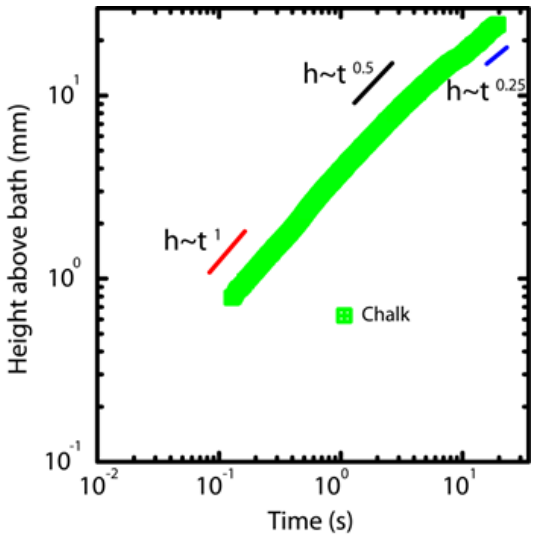

Figure 5.13: Capillary rise experiment using chalk, a rigid porous material. We observe inertial-capillary ($h \sim t$) and Washburn ($h \sim t^{0.5}$) regimes and observe the transition to the post- Washburn regime ($h \sim t^{0.25}$).

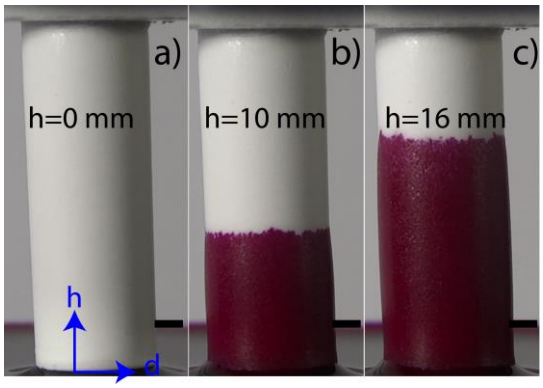

Figure 5.14: Increase in the height of water wicked up by capillary rise in S20 at a) 0 s, b) 10 s and c) 32 s. Scale bar in the pictures corresponds to 2 mm.

be decoupled, unlike in previous studies in the literature.[44]

Figure 5.15 shows the variation of the front height with time for both composite and cross-linked polymer sponges. As shown in Figure 5.15, these profiles show two distinct capillary rise regimes: initially, in the inertial-capillary regime, $h \sim t$, and at later times, the Lucas-

Washburn VC regime is observed where $h \sim t^{0.5}$. No post VC regime transition is observed in the experimental time scales accessed in this work. To further understand the flow behavior in the IC regime, the liquid front velocity (V) is calculated from the slope of h vs t plot. A straight line is fitted to the data in the IC regime, and we tabulate these results in Table 5.2. From this data, it is clear that for both types of sponges, the velocity of liquid front decreases with decreasing porosity. The scaling exponent, $n1$, obtained by fitting the experimental data to $h \sim t^{n1}$, is close to 1, as expected in the IC regime. In the VC regime, the front height as a function of time is plotted and the data is fitted as $h \sim t^{n2}$. The values of power law exponent, $n2$, and prefactor, c, are listed in Table 5.2. It is clear from this table that the liquid front velocity at any given time is higher for polymeric sponges as compared to corresponding composite sponges. The transition time and height are termed as $t_{transition}$ and $h_{transition}$, respectively, and are also shown in Table 5.2. When the front height is normalized by $h_{transition}$ and plot this as a function of time normalized by $t_{transition}$, it is observed that the data for all the polymeric and composite sponges collapse onto a master curve (Figure 5.16). This suggests that capillary driven flow follows a universal trend independent of sponge elasticity and porosity.

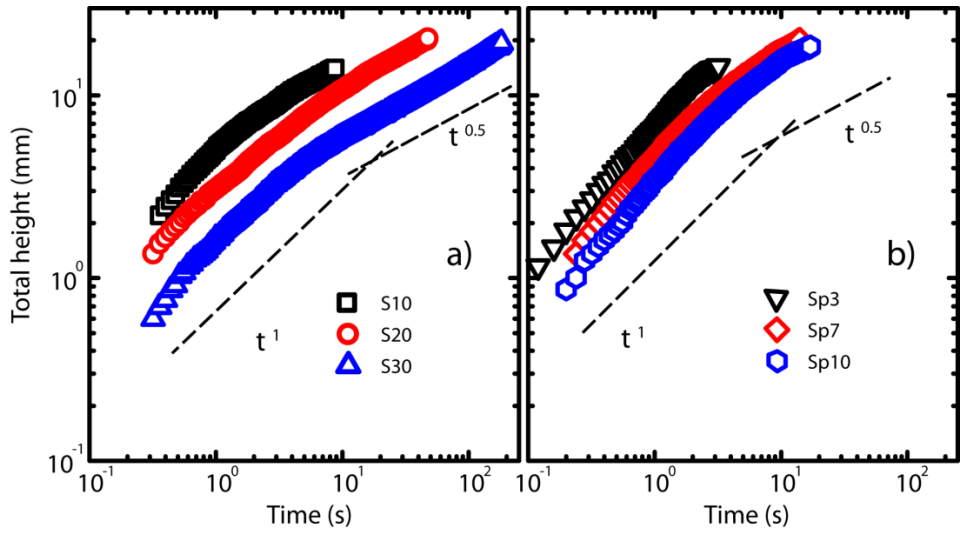

Figure 5.15: Height of water imbibed as a function of time for (a) composite, (b) cross-linked polymer sponges. The dotted lines indicate the scaling expected for inertial-capillary (IC) and viscous capillary (VC) regimes.

A simplified equation that describes flow in capillaries can be written as:

$$-\rho\frac{d(h\dot{h})}{dt} = -\frac{4\sigma}{D} + \frac{\varepsilon\mu h\dot{h}}{K} \qquad (1)$$

where $\dot{h}$ is the time derivative of the front height, h; $\rho$and μ are the liquid density and viscosity; σ is the surface tension; D is the capillary pore size; ε is the sponge porosity and K is the sponge permeability.

Table 5.2: The scaling exponent, $n1$, ($h \sim t^{n1}$); IC regime velocity; VC regime slope ($n2$); prefactor (c); transition time, $t_{transition}$; height, $h_{transition}$for transition from inertial-capillary (IC) regime to viscous-capillary (VC) regime for polymeric and composite sponges obtained from fitting the experimental data .

Sponge	$n1$	IC velocity (V, mm/s)	$n2$	c (mm.s$^{-0.5}$)	$t_{transition}$(s)	$h_{transition}$(mm)
S10	0.92±0.09	5.2±0.5	0.50±0.07	4.7±0.7	1.04	4.61±0.17
S20	0.81±0.13	2.7±0.5	0.51±0.07	3.2±0.5	1.32	3.30±0.06
S30	1.04±0.09	1.6±0.1	0.49±0.05	1.8±0.2	2.20	2.36±0.15
Sp3	0.92±0.08	6.0±0.9	0.60±0.08	5.1±1.0	1.05	5.24±0.51
Sp7	0.85±0.12	4.1±0.8	0.53±0.05	4.2±0.7	1.56	5.07±0.46
Sp10	0.81±0.12	2.8±0.7	0.53±0.09	3.2±0.8	1.64	3.66±0.33

In the IC regime, flow is set by a balance between the capillary pressure driving force ($4\sigma/D$) and the inertial term ($\rho\frac{d(h\dot{h})}{dt} = \frac{\rho}{2}\frac{d^2(h^2)}{dt^2}$). This results in the scaling: $h \sim t$. In the VC regime, a balance between the capillary pressure driving force ($4\sigma/D$) and the viscous dissipation ($\varepsilon\mu h\dot{h})/K = \frac{\varepsilon\mu}{2K}(\frac{d(h^2)}{dt}$) results in a Lucas-Washburn scaling for the front height ($h \sim t^{0.5}$). Thus, equation (1) allows to rationalize the scalings for front height with time observed experimentally in the IC and VC regimes. However, equation (1) models flow in capillaries and does not account for the effect of sponge microstructure. In a porous sponge, advancement of the liquid front is influenced by pore size, geometry and total porosity. In the case of these ice-templated sponges the mean pore size and the volume porosity are not independent and, there is a decrease in both mean pore size and porosity with increase in

concentration of the ice-templated dispersion. Equation (1) does not account for the complexity of porous media. We introduce the influence of the sponge microstructure in an ad hoc manner by making a comparison with the Ergun/ Forchheimer equations[10,45–47] that are used to describe pressure driven flow in rigid porous beds.

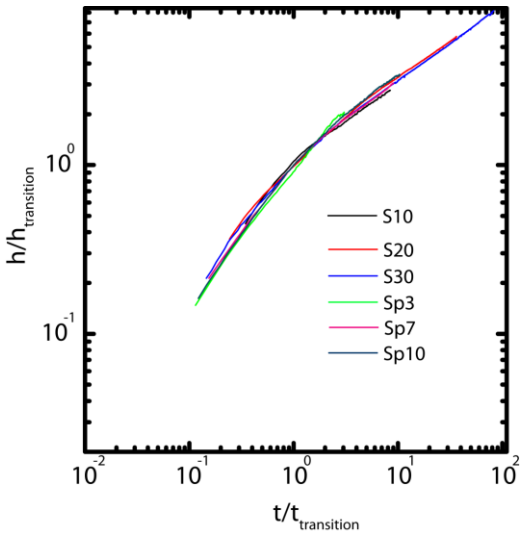

Figure 5.16: Height of sponge imbibed with water (h) as a function of time, t, during the capillary rise experiment. Data is presented for the polymeric sponges and composite sponges by normalizing using $\boldsymbol{h_{transition}}$ and $\boldsymbol{t_{transition}}$ to obtain a master curve for all sponges.

$$\frac{\Delta P}{L} = a_0 V + a_1 V^2 \qquad (2)$$

where $\Delta P/L$ is the pressure drop that drives flow, V is the front velocity and a_0 and a_1 are constants relating to flow resistance in the viscous and inertial regimes, respectively. The pressure drop that drives flow in the Ergun/Forchheimer equations with the capillary pressure ($4\sigma/D$) is equated, where we take D as the pore size in the sponge. It can be noted that the pores in these ice-templated sponges are connected through openings that are smaller than the pore size (Figure 5.8). These smaller openings are likely to set the capillary pressure. However, we anticipate that the size of these openings will scale with the sponge pore size. Since it is difficult to estimate the size of the inter-pore openings, we use the sponge pore size to estimate the capillary pressure. Thus, $\Delta P/L = \frac{4\sigma}{hD}$ and $V = dh/dt$ where h is the front height. Handy[48] had suggested combining the differential equation for capillary flow with Darcy's

law. In a similar vein, we consider the VC regime where $(4\sigma/L)$ is dominated by the term that is linear in V. Thus,

$$\boldsymbol{a_0 V = \frac{4\sigma}{hD}} \qquad (3)$$

Following Ergun, one can write:

$$\boldsymbol{a_0 = \frac{\alpha S_v^2 \mu (1-\varepsilon)^2}{\varepsilon^3}} \qquad (4)$$

where α is a constant that depends on the porous microstructure and, the specific surface area, $S_v = 4\varepsilon/D\ (1-\varepsilon)$. Thus, from equations (3) and (4), we obtain:

$$\boldsymbol{\frac{16\alpha\mu}{\varepsilon D} V = \frac{4\sigma}{h}} \qquad (5)$$

Since the front velocity, $V = dh/dt$, one can obtain:

$$\boldsymbol{h = \sqrt{\frac{\sigma\varepsilon D}{2\alpha\mu}}\, t^{0.5}} \qquad (6)$$

This analysis indicates the relationship of the experimentally obtained prefactor, c (see Table 5.2), to the sponge microstructure. To verify this, c is plotted as a function of $\sqrt{\varepsilon D}$ (Figure 5.17). It is observed that c is linear in $\sqrt{\varepsilon D}$ as anticipated by equation (6). Slopes of 1.41 $(m/s)^{0.5}$ and 1.58 $(m/s)^{0.5}$ are obtained for the polymeric and composite sponges, respectively. For the dyed water, we calculate $\sqrt{\sigma/2\mu} \approx 6\ (m/s)^{0.5}$. Thus, this suggests that α has values of 18.11 and 14.42 for polymeric and composite sponges, respectively. Remarkably for such a simplified analysis, these values are in the range observed by Ergun and Orning.[45]

Our analysis makes several simplifications. First, we make an ad hoc relationship between equation (1), valid for capillary rise in cylindrical capillaries, with the Ergun/Forchheimer relation to account for the pore microstructure. We note that the Ergun/Forchheimer equations are relevant for pressure driven flow through rigid porous media and are not typically applied to such highly porous systems as in this work. Therefore, it is remarkable that the data for capillary uptake in these swellable, relatively low modulus highly porous polymeric and composite sponges are consistent with this analysis. Given the simplifications in our approach, the agreement between the experimental data and the analysis is reasonable.

Continuing in this spirit, we anticipate that the transition between the IC and VC regimes would correspond to a situation where the contribution to the pressure drop from the Darcy law term is comparable to that from the inertial term. Thus, at the transition, we set:

$$a_0 V = a_1 V^2 \qquad (7)$$

In IC regime, the front velocity is constant. Therefore, we set $V = h_{transition}/t_{transition}$.

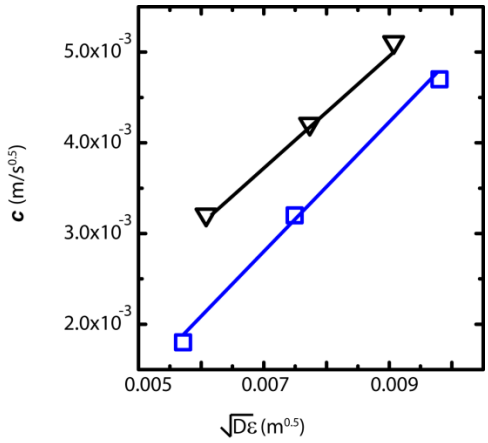

Figure 5.17: Prefactor,(c), obtained by fitting experimental data in VC regime as a function of $\sqrt{D\varepsilon}$, for both polymeric and composite sponges.

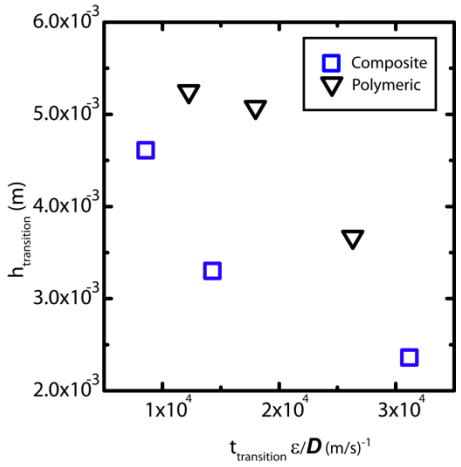

Figure 5.18: Transition height ($h_{transition}$) is plotted as a function of ($t_{transition}$)*ε/D for sponges at VC regime.

Now, we write:

$$a_1 = \frac{\beta S_v \rho(1-\varepsilon)}{\varepsilon^3} \qquad (8)$$

Where β depends on pore size and pore microstructure

From equations (7) and (8), we obtain:

$$h_{transition} = \frac{4\alpha}{\beta}\frac{\mu}{\rho}\frac{\varepsilon}{D}t_{transition} \qquad (9)$$

A plot of $h_{transition}$ as a function of $\frac{\varepsilon}{D}t_{transition}$ is shown in Figure 5.18 and we obtain $|\frac{4\alpha}{\beta}| = 1.16\text{x}10^2$ for polymeric and composite sponges, respectively. For $\alpha \approx 15$, $\beta \approx 0.13$ is obtained. This value is in the range that has been observed in the literature for flow through porous materials.[10]

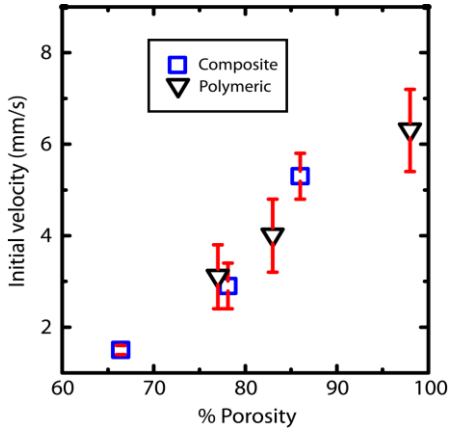

Figure 5.19: Front velocity in the IC regime during capillary imbibition as a function of sponge porosity for composite and polymeric sponges.

Finally, the IC regime is examined. Here, the pressure drop is dominated by the inertial term and we set $\frac{\Delta P}{L} = \frac{4\sigma}{hD} = a_1 V^2$. Using (8), we obtain:

$$V^2 = \frac{\sigma\varepsilon^2}{\beta\rho h} \qquad (10)$$

In the IC regime, it is experimentally observed that the front height increases linearly in time and the front velocity, V is constant, independent of h. This is consistent with the theoretical expectation that $h \sim t$ in the IC regime. However, relating the capillary pressure to the pressure drop from the Ergun-Forchheimer equation yields results that are inconsistent with theoretical expectations and with our experiments. Experimentally, it is observed that $V \propto \varepsilon$ (Figure 5.19). Therefore, setting $\frac{\Delta P}{L} = \frac{4\sigma}{LD}$ where L is a constant yields $V^2 = \frac{\sigma\varepsilon^2}{\beta\rho L}$ allowing us to reconcile with theory and experiments. From the slope of V versus ε (Figure 5.19), $\beta L \approx 10^{-1}$

is obtained. Thus, L ~O(1 m). There is no physically meaningful length scale of the order of 1 m in this experiment. Therefore, while this approach allows us to obtain the correct scaling of rise height with time, and correctly predicts the experimentally obtained dependence of rise velocity on sponge porosity, the origin of the length scale necessary to connect the differential equitation for flow through capillaries with inertial term in the Ergun-Forchheimer equation is not clear.

5.5 Conclusions

Water uptake in a series of ice-templated sponges is investigated with a random porous structure, and with a wide variation in properties (porosity varying from 66 to 98%; modulus varying by over an order of magnitude and wall composition varying from polymeric to polymer-inorganic composite). The sponges investigated in this work are highly swellable (with volume change varying from about 25 to 62% on water imbibition), in contrast to previous reports that describe either rigid porous media[10,24–31,39] or relatively less swellable media.[33,41,44,45]A remarkable universality is observed in capillary uptake in porous sponges, over the entire range of sponge porosity and deformability. Initially, the height of the liquid in the sponge increases linearly in time, indicative of the inertial-capillary regime. Beyond a transition threshold, it is observed that the uptake is dominated by viscosity and that the liquid height in the sponge rises with the square root of time, indicative of the viscous-capillary regime. Thus, the kinetics of water uptake for all sponges studied can be collapsed onto a universal curve. Interestingly, capillary rise is governed only by total porosity, and is independent of the sponge modulus and swellability. A simplified analysis that combines the effect of sponge microstructure (adapted from the macroscopic Ergun/Forchheimer treatment) with the differential equation that describes capillary flow in tubes is presented here. This analysis is successful in modelling the viscous capillary regime and the transition from inertially dominated to viscous dominated flow. However, ad hoc introduction of an additional length scale is necessary to describe the inertial capillary regime. These results have direct implications for the design of novel reusable sponges being developed for environmental remediation.[2,15,16,20]

5.6 References

(1) Feinle, A.; Elsaesser, M. S.; Hüsing, N. Sol–gel Synthesis of Monolithic Materials with Hierarchical Porosity. *Chem. Soc. Rev.* **2016**, *45*, 3377–3399.

(2) Wang, G.; He, Y.; Wang, H.; Zhang, L.; Yu, Q.; Peng, S.; Wu, X.; Ren, T.; Zeng, Z.; Xue, Q.; Cellulose Sponge with Robust Superhydrophilicity and under-Water Superoleophobicity for Highly Effective Oil/water Separation. *Green Chem.* **2015**, *17*, 3093–3099.

(3) Wang, J.; Zheng, Y.; Wang, A. Effect of Kapok Fiber Treated with Various Solvents on Oil Absorbency. *Ind. Crops Prod.* **2012**, *40*, 178–184.

(4) Wang, S.; Peng, X.; Zhong, L.; Tan, J.; Jing, S.; Cao, X.; Chen, W.; Liu, C.; Sun, R. An Ultralight, Elastic, Cost-Effective, and Highly Recyclable Superabsorbent from Microfibrillated Cellulose Fibers for Oil Spillage Cleanup. *J. Mater. Chem. A* **2015**, *3*, 8772–8781.

(5) Zhang, Z.; Sèbe, G.; Rentsch, D.; Zimmermann, T.; Tingaut, P. Ultralightweight and Flexible Silylated Nanocellulose Sponges for the Selective Removal of Oil from Water. *Chem. Mater.* **2014**, *26*, 2659–2668.

(6) Breulmann, M.; Davis, S. A.; Mann, S.; Hentze, H.-P.; Antonietti, M. Polymer-Gel Templating of Porous Inorganic Macro-Structures Using Nanoparticle Building Blocks. *Adv. Mater.* **2000**, *12*, 502–507.

(7) Rhodes, K; Davis, S; Caruso, F; Zhang, B; Mann, S. Hierarchical Assembly of Zeolite Nanoparticles into Ordered Macroporous Monoliths Using Core−Shell Building Blocks. **2000,** *12*, 2832–2834.

(8) Stein, A.; Li, F.; Denny, N. R. Morphological Control in Colloidal Crystal Templating of Inverse Opals, Hierarchical Structures, and Shaped Particles . *Chem. Mater.* **2008**, *20* , 649–666.

(9) Sharma, K. P.; Ganai, A. K.; Gupta, S. Sen; Kumaraswamy, G. Self-Standing Three-Dimensional Networks of Nanoparticles With Controllable Morphology by Dynamic Templating of Surfactant Hexagonal Domains. *Chem. Mater.* **2011**, *23*, 1448–1455.

(10) Richardson, J. .; Peng, Y.; Remue, D. Properties of Ceramic Foam Catalyst Supports: Pressure Drop. *Appl. Catal. A Gen.* **2000**, *204*, 19–32.

(11) Gui, X.; Wei, J.; Wang, K.; Cao, A.; Zhu, H.; Jia, Y.; Shu, Q.; Wu, D. Carbon

Nanotube Sponges. *Adv. Mater.* **2010**, *22*, 617–621.

(12) Venkateswara Rao, A.; Hegde, N. D.; Hirashima, H. Absorption and Desorption of Organic Liquids in Elastic Superhydrophobic Silica Aerogels. *J. Colloid Interface Sci.* **2007**, *305*, 124–132.

(13) Mallepally, R. R.; Bernard, I.; Marin, M. A.; Ward, K. R.; McHugh, M. A. Superabsorbent Alginate Aerogels. *J. Supercrit. Fluids.* **2013**, *79*, 202–208.

(14) Liu, T.; Huang, M.; Li, X.; Wang, C.; Gui, C.-X.; Yu, Z.-Z. Highly Compressible Anisotropic Graphene Aerogels Fabricated by Directional Freezing for Efficient Absorption of Organic Liquids. *Carbon N. Y.* **2016**, *100*, 456–464.

(15) Sun, H.; Xu, Z.; Gao, C. Multifunctional, Ultra-Flyweight, Synergistically Assembled Carbon Aerogels. *Adv. Mater.* **2013**, *25*, 2554–2560.

(16) Ruan, C.; Ai, K.; Li, X.; Lu, L. A Superhydrophobic Sponge with Excellent Absorbency and Flame Retardancy. *Angew. Chemie Int. Ed.* **2014**, *53*, 5556–5560.

(17) Sun, H.; Schiraldi, D. A.; Chen, D.; Wang, D.; Sánchez-Soto, M. Tough Polymer Aerogels Incorporating a Conformal Inorganic Coating for Low Flammability and Durable Hydrophobicity. *ACS Appl. Mater. Interfaces.* **2016**, *8*, 13051–13057.

(18) Choi, S.-J.; Kwon, T.-H.; Im, H.; Moon, D.-I.; Baek, D. J.; Seol, M.-L.; Duarte, J. P.; Choi, Y.-K. A Polydimethylsiloxane (PDMS) Sponge for the Selective Absorption of Oil from Water. *ACS Appl. Mater. Interfaces* **2011**, *3*, 4552–4556.

(19) Tran, D. N. H.; Kabiri, S.; Sim, T. R.; Losic, D. Selective Adsorption of Oil–water Mixtures Using Polydimethylsiloxane (PDMS)–graphene Sponges. *Environ. Sci. Water Res. Technol.* **2015**, *1*, 298–305.

(20) Zhang, A.; Chen, M.; Du, C.; Guo, H.; Bai, H.; Li, L. Poly(dimethylsiloxane) Oil Absorbent with a Three-Dimensionally Interconnected Porous Structure and Swellable Skeleton. *ACS Appl. Mater. Interfaces.* **2013**, *5*, 10201–10206.

(21) Deville, S. Ice-templating, freeze casting: Beyond materials processing. *J. Mater. Res.* **2013**,28, 2202-2219.

(22) Gutiérrez, M. C.; Ferrer, M. L.; del Monte, F. Ice-Templated Materials: Sophisticated Structures Exhibiting Enhanced Functionalities Obtained after Unidirectional Freezing and Ice-Segregation-Induced Self-Assembly . *Chem. Mater.* **2008**, *20*, 634–648.

(23) Dagalakis, N.; Flink, J.; Stasikelis, P.; Burke, J. F.; Yannas, I. V. Design of an Artificial Skin. Part III. Control of Pore Structure. *J. Biomed. Mater. Res.* **1980**, *14*, 511–528.

(24) Washburn, E. W. The Dynamics of Capillary Flow. *Phys. Rev.* **1921**, *17*, 273–283.

(25) Delker, T.; Pengra, D. B.; Wong, P. Interface Pinning and the Dynamics of Capillary Rise in Porous Media. *Phys. Rev. Lett.* **1996**, *76* , 2902–2905.

(26) Lago, M.; Araujo, M. Capillary Rise in Porous Media. *Phys. A Stat. Mech. its Appl.* **2001**, *289*, 1–17.

(27) Yang, Y.-W.; Zografi, G.; Miller, E. E. Capillary Flow Phenomena and Wettability in Porous Media: II. Dynamic Flow Studies. *J. Colloid Interface Sci.* **1988**, *122*, 35–46.

(28) Siebold, A.; Walliser, A.; Nardin, M.; Oppliger, M.; Schultz, J. Capillary Rise for Thermodynamic Characterization of Solid Particle Surface. *J. Colloid Interface Sci.* **1997**, *186*, 60–70.

(29) Fries, N.; Dreyer, M. The Transition from Inertial to Viscous Flow in Capillary Rise. *J. Colloid Interface Sci.* **2008**, *327*, 125–128.

(30) Marmur, A.; Cohen, R. D. Characterization of Porous Media by the Kinetics of Liquid Penetration: The Vertical Capillaries Model. *J. Colloid Interface Sci.* **1997**, *189*, 299–304.

(31) Pezron, I.; Bourgain, G.; Quéré, D. Imbibition of a Fabric. *J. Colloid Interface Sci.* **1995**, *173*, 319–327.

(32) Preziosi, L.; Joseph, D. D.; Beavers, G. S. Infiltration of Initially Dry, Deformable Porous Media. *Int. J. Multiph. Flow* **1996**, *22*, 1205–1222.

(33) Bico, J.; Roman, B.; Moulin, L.; Boudaoud, A. Adhesion: Elastocapillary Coalescence in Wet Hair. *Nature* **2004**, *432*, 690–690.

(34) van Honschoten, J. W.; Brunets, N.; Tas, N. R. Capillarity at the Nanoscale. *Chem. Soc. Rev.* **2010**, *39*, 1096.

(35) Cambau, T.; Bico, J.; Reyssat, E. Capillary Rise between Flexible Walls. *EPL (Europhysics Lett.)***2011**, *96*, 24001.

(36) Aristoff, J. M.; Duprat, C.; Stone, H. A. Elastocapillary Imbibition. *Int. J. Non. Linear. Mech.* **2011**, *46*, 648–656.

(37) Duprat, C.; Aristoff, J. M.; Stone, H. A. Dynamics of Elastocapillary Rise. *J. Fluid Mech.* **2011**, *679*, 641–654.

(38) Dreyer, M.; Delgado, A.; Path, H.-J. Capillary Rise of Liquid between Parallel Plates

under Microgravity. *J. Colloid Interface Sci.* **1994**, *163*, 158–168.

(39) Stange, M.; Dreyer, M. E.; Rath, H. J. Capillary Driven Flow in Circular Cylindrical Tubes. *Phys. Fluids* **2003**, *15*, 2587–2601.

(40) Siddique, J. I.; Anderson, D. M.; Bondarev, A. Capillary Rise of a Liquid into a Deformable Porous Material. *Phys. Fluids* **2009**, *21*, 13106.

(41) Rajamanickam, R.; Kumari, S.; Kumar, D.; Ghosh, S.; Kim, J. C.; Tae, G.; Sen Gupta, S.; Kumaraswamy, G. Soft Colloidal Scaffolds Capable of Elastic Recovery after Large Compressive Strains. *Chem. Mater.* **2014**, *26*, 5161–5168.

(42) Sharma, K. P.; Choudhury, C. K.; Srivastava, S.; Davis, H.; Rajamohanan, P. R.; Roy, S.; Kumaraswamy, G. Assembly of Polyethyleneimine in the Hexagonal Mesophase of Nonionic Surfactant: Effect of pH and Temperature. *J. Phys. Chem. B* **2011**, *115*, 9059–9069.

(43) Silva, J. E.; Geryak, R.; Loney, D. A.; Kottke, P. A.; Naik, R. R.; Tsukruk, V. V.; Fedorov, A. G.; Szleifer, I.; Tsukruk, V. V.; Urban, M. Stick–slip Water Penetration into Capillaries Coated with Swelling Hydrogel. *Soft Matter* **2015**, *11*, 5933–5939.

(44) Andersson, J.; Ström, A.; Gebäck, T.; Larsson, A.; Kim, J.; Je, J. H.; Ström, A.; Hermansson, A.-M.; Paik, K.; Nimpf, J.; Rajadas, J.; Longaker, M. T.; Gurtner, G. C. Dynamics of Capillary Transport in Semi-Solid Channels. *Soft Matter* **2017**, *13*, 2562–2570.

(45) Ergun, S.; Orning, A. A. Fluid Flow through Randomly Packed Columns and Fluidized Beds. *Ind. Eng. Chem.* **1949**, *41*, 1179–1184.

(46) Geertsma, J. Estimating the Coefficient of Inertial Resistance in Fluid Flow Through Porous Media. *Soc. Pet. Eng. J.* **1974**, *14*, 445–450.

(47) Dukhan, N.; Bağcı, Ö.; Özdemir, M. Experimental Flow in Various Porous Media and Reconciliation of Forchheimer and Ergun Relations. *Exp. Therm. Fluid Sci.* **2014**, *57*, 425–433.

(48) Handy, L. L. Determination of Effective Capillary Pressures for Porous Media from Imbibition Data. **1960,** 219, 75-80.

Role of Acetonitrile on the Morphology of Macroporous Composite Scaffolds Prepared by Ice-templating and their Application

In this chapter, we report for the first time, the preparation of inorganic/polymer macroporous hybrid scaffolds with perforations in the walls. This unusual morphology is obtained by the addition of acetonitrile (ACN) as non-freezing organic phase in the ice templated dispersion. ACN allows control of the mean pore size as well. Scaffold with perforated walls, obtained using this method retain the elasticity and mechanical integrity of scaffolds prepared without ACN. However, perforation in the walls results in lower pressure drops for flow of water flow through the scaffolds.

6.1 Introduction

The flow of liquids through porous beds is of relevance to a variety of applications. For example, porous materials are often used as supports in catalysis. Mounting a catalytic moiety on a porous support allows us to heterogenize the catalyst while providing a large specific surface area for the substrate reactants to access the catalyst. The specific surface area is inversely proportional to the pore size of the support. However, there is a significant increase in pumping costs when reactants are pumped through small pore size supports in continuous flow synthesis. Therefore, it is necessary to optimize the pore size distribution when designing monolithic catalyst supports for flow reactors. One strategy that has been described in the past[1-5] is to use hierarchically porous structures that combine macroporous monoliths, associated with low pressure drops for flow, with microporous structures that afford a high specific surface area for catalyst immobilization. However, detailed studies of the residence time distribution for flow through such hierarchically micro/macroporous monoliths have not been reported.

Researchers have demonstrated that the structure of the macroporous monolith obtained by ice templating can be manipulated by varying the conditions for ice templating. For example, directional ice templating has been employed to produce oriented pore morphologies.[6–15] Ice templating of suspensions of microporous particles has been used to prepare monoliths that combine micro and macroporosity.[16,17] However, there have been relatively limited reports of ice-templated monoliths that combine different levels of porosity. Thus, creative strategies to introduce porosity at different length scales in ice templating offer the chance to harness the advantages of ice templating (such as the use of green solvent, and the ability to prepare materials using a diverse library of functional colloids and polymers) in applications where liquid needs to be pumped through monoliths.

Here, we demonstrate a novel route to the preparation of dual macroporous polymer/particle hybrid scaffolds that affords mechanically resilient monolithic structures. We show that perforated pore walls can be generated by adding a suitable organic solvent during ice-templating process. To the best of our knowledge, this is the first report that creates such a micro structure using this simple technique. These novel scaffolds do not require any post processing steps such as freeze drying and sintering/calcination. This unusual perforated wall microstructure does not significantly change the scaffold bulk porosity and compression

modulus. We observe a significant reduction in pressure drop in the scaffolds with increasing population of smaller holes in the pore walls.

6.2 Experimental

6.2.1 Materials:

Polyethylenimine (PEI, branched polymer with supplier specified molecular weight Mw= 750 kDa); 1,4-butanediol diglycidyl ether, acetonitrile (HPLC grade), Rhodamine B were obtained from Sigma Aldrich and were used as received. Distilled deionized water (resistivity ~18.2 MΩ.cm) from a Millipore MilliQ unit was used as solvent to prepare scaffolds. Glass tubes (inner diameter 3 mm; length 30 mm) were obtained from Katholieke University, Belgium and cleaned using an acidic piranha etch before use.

6.2.2 Fabrication of hybrid scaffolds with different acetonitrile concentration:

Monolithic scaffolds were prepared in glass tubes, using a modification of protocols described in previous chapters. Piranha etched glass tubes were dipped in an aqueous solution of PEI, to allow the polymer to adsorb on the walls of the tube. Subsequently, the tubes were removed and one end of the tube was blocked using Teflon tape. Ice templating is performed in this tube. In a typical synthesis, 120 mg of silica particles was taken in a plastic container and dispersed in 1064 µl water by sonication for 15 minutes. To this aqueous particle dispersion, 10 mg PEI (100 µl of 100 mg/ml stock solution), 16 mg 1,4-butanediol diglycidyl ether as cross-linker and 20 µl acetonitrile (corresponding to 1.6% v/v) was thoroughly mixed. This dispersion is then transferred to a glass tube, prepared as described earlier.

When water freezes to form ice, the silica particles and organic molecules in the dispersion are concentrated in the regions between ice crystals. We have demonstrated that this enhancement in concentration results in cross-linking of the PEI, and a composite structure forms with silica particles held together in a cross-linked PEI mesh. Here, the composite monolith forms in the glass tube surface adsorbed with PEI. PEI adsorbed on the walls of the glass tube is cross-linked with that in the monolith, resulting in strong adhesion of the monolith with the tube. After cross-linking proceeds for 24 h, the monolith formed is thoroughly washed with copious amounts of water.

Monoliths prepared with 1.6% acetonitrile added to the ice-templated aqueous dispersion are termed $S_{1.6}$. Similarly, we also prepare hybrid scaffolds with varying acetonitrile (ACN)

concentration (3.2 and 6.4%), and with same quantity of particle, polymer and cross-linker as earlier. These scaffolds are termed $S_{3.2}$ and $S_{6.4}$, respectively. Hybrid scaffolds prepared without the addition of ACN are termed S_0. Scaffolds synthesized in the glass tubes were used for pressure drop and residence time determination (RTD) measurements, while identical scaffolds are prepared in plastic vials for structural and mechanical characterization.

6.2.3 Pressure drop and RTD study:

We use a home-built experimental set up to examine the pressure drop to pump water through the scaffolds. Initially, we manually fill the glass tube containing the scaffold with water. In all our experiments, we used scaffolds of length = 4 cm. The glass tube is then connected to a syringe pump (Harvard Apparatus PHD 2000) through a soft silicone connector tube. A digital manometer (HTC PM 6205) is used to record the pressure drop across the length of the scaffold as water is pumped through it using the syringe pump. The manometer is connected across the scaffold through T-joints in the silicone tubes by-products.

6.3 Instruments and Characterization:

The microstructure of the scaffolds was characterized using a Quanta 200 3D scanning electron microscope (SEM). Thermogravimetric analysis (TGA) was performed using a TA Instruments SDT Q6000 analyzer between 120 and 700 °C at a heating rate of 10 °Cmin^{-1} in N_2 atmosphere. Mechanical properties of the scaffolds were characterized using a strain controlled rheometer, TA-ARES G2, equipped with a normal force transducer.

6.4 Results and Discussion

6.4.1 Characterization of ice-templated scaffolds:

Ice-templating results in the formation of macroporous scaffolds, with hybrid walls templating the shape of the ice crystals. The walls of the scaffold are comprised of silica particles held in a mesh of cross-linked polymer. We obtain centimetre-sized macroporous scaffolds following the preparation protocol outlined in Figure 6.1. Addition of small quantities of ACN, a water-miscible organic solvent, has a significant effect on the microstructure of the ice-templated scaffolds.

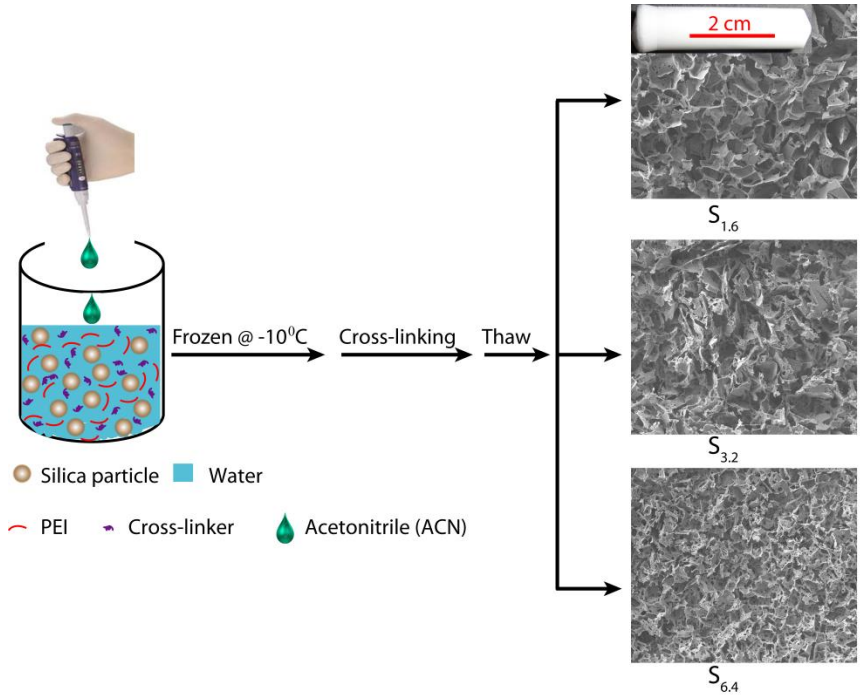

Figure 6.1: Schematic representation of the preparation protocol for hierarchically porous ice-templated hybrid monoliths.

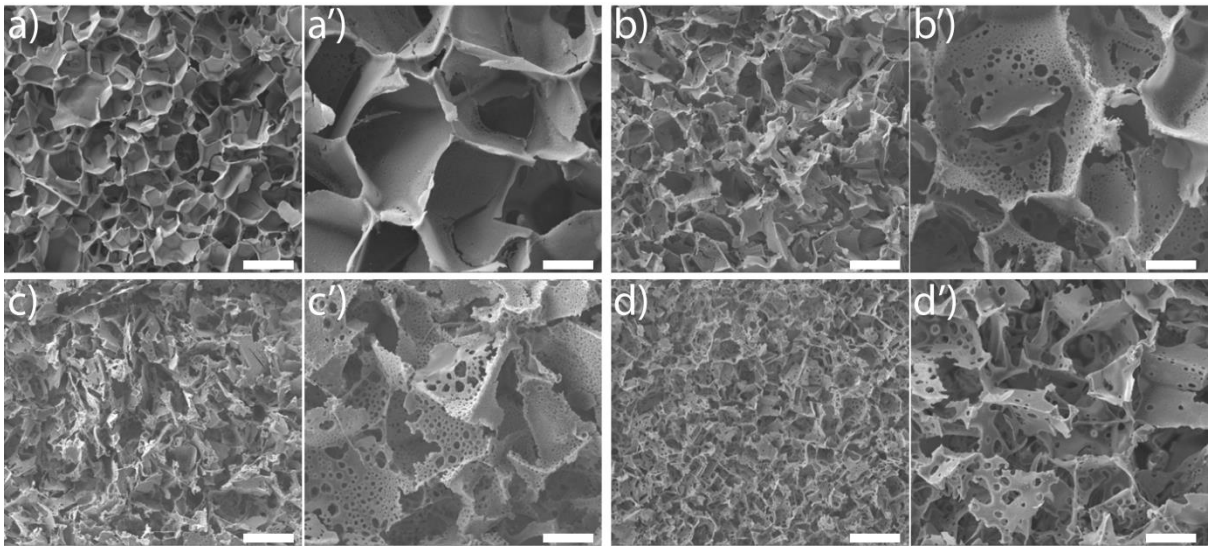

Figure 6.2: SEM micrographs of S_0 (a and a´); $S_{1.6}$ (b, b´); $S_{3.2}$ (c, c´) and $S_{6.4}$ (d, d´). a, b, c and d are low resolution micrographs (scale bar corresponds to 200 microns). a´, b´, c´ and d´ are higher resolution images, where the scale bar corresponds to 50 microns.

SEM images reveal that ice-templating results in the formation of an interconnected network structure in all scaffolds (Figure 6.2). The particles/cross-linked polymer hybrid structure form walls that enclose the pores formed by ice crystals, that act as porogens. Qualitatively,

addition of acetonitrile to the dispersion that undergoes ice templating results in the appearance of holes that perforate the walls formed by the particle/cross-linked polymer hybrid. Additionally, there appears to be a decrease in pore size. We quantitate the SEM images by performing image analysis using Image J. We define "pores" as the large voids created by cross-linking the particle/polymer hybrid around the ice crystal porogens, and "holes" as the perforations in the hybrid walls. From the SEM micrographs, it is evident that pores are characterized by larger length scales (> 10 microns), compared with holes (3 – 10 microns). For each material, we use multiple SEM micrographs taken at different locations of the sample and measure at least 500 pores and 2000 holes to obtain the size distribution.

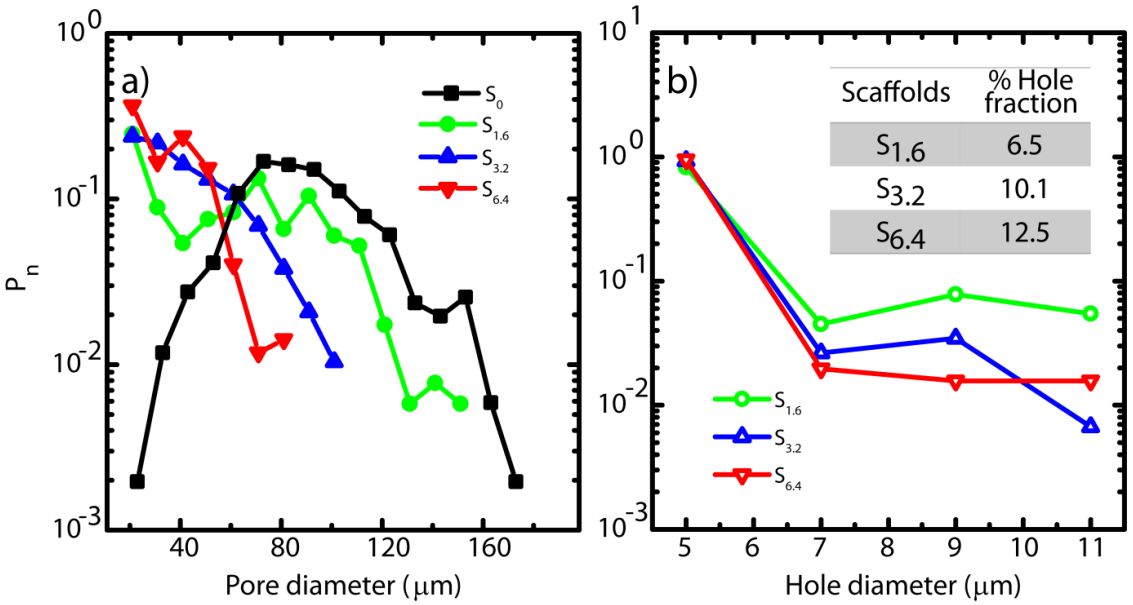

Figure 6.3: (a) Pore and (b) hole size distributions obtained from SEM micrographs. Inset (b) indicates the fraction of the wall surface area that is covered by holes in the scaffolds.

In Figure 6.3, we plot the normalized size distribution for pores and holes, obtained by binning the size data from image analysis. We neglect the interconnections between pores in this analysis. We observe that S_0 has a peak in the pore size distribution, at about 50-70 μm (Figure 6.3a). This is consistent with our previous image analysis,[18] that indicated a most probable pore size of 65 microns, and with previous X-ray tomography analysis in Chapter 5. Interestingly, on addition of ACN, there is no longer a clear maximum in the pore size distribution. Rather, there is a qualitative change in the shape of the pore size distribution due to a dramatic increase in the frequency of small size pores (Figure 6.3 a). Increase in ACN concentration leads to a decrease in the average pore size.

The ACN-water binary solvent system is extensively used in chromatography and is therefore, well studied.[19–21] At the concentrations used in this work, water and ACN remain miscible. Addition of miscible organic solvents such as ACN, results in a decrease in the freezing point of the solution.[22] There is greater decrease in freezing point for higher ACN concentrations – however, even at 6.4% the decrease in freezing point is only about 3 °C .[23] The size of the ice crystals formed by freezing of water-organic solvent mixtures is governed by a wide variety of factors including solvent-induced changes in nucleation and growth rates, temperature equilibration in the sample (that depends on sample size and cooling rate), Ostwald ripening, etc. While models have been described that predict ice crystal size obtained by freezing water-solvent mixtures, these models still require significant inputs from experimental measurements and therefore cannot be used in a predictive manner.[24] In our experiments, the aqueous dispersion has silica particles, polymer and diepoxy cross-linker, in addition to ACN. Therefore, physical rationalization of our experimental observations on the effect of ACN on the pore size distribution is challenging. We simply note that we observe a decrease in average pore size, and a qualitative change in the shape of the pore size distribution on ice templating dispersions with increasing ACN concentration.

SEM reveals another interesting consequence of the addition of ACN. We observe that ice-templated samples from water-ACN mixtures are characterized by walls that are perforated, with small holes that are 3-10 μm in size (Figure 6.3 b). With increase in ACN concentration, there is an increase in the fraction of the wall area with holes increasing from 6.5% to 10.1% to 12.5% for 1.6%, 3.2% and 6.4% ACN, respectively. In all scaffolds, the frequency of holes decreases with increasing hole size (Figure 6.3 b). The data also suggests that increasing ACN concentration strongly increases the fraction of small (3 to 5 micron) holes at the expense of the larger (5 to 12 micron) holes. This is the first report of the formation of such perforated walls during ice templating, and the appearance of small holes in the pore walls is very unusual. The mechanism of formation of holes during ice templating is not fully understood at this time. We believe that ACN plays a key role in hole formation. It is possible that as the water freezes, there is an increase in ACN concentration in the liquid phase that results in phase separation into water rich and ACN rich phases. Colloids, polymer and cross-linker partition between these phases. Since the ACN rich phase does not freeze, polymer and cross-linker do not get concentrated in this phase and, consequently, there is no cross-linking. Therefore, after the sample is thawed, the regions where the phase separated ACN droplets remain uncross-linked and form holes in the composite walls.

The addition of ACN does not significantly vary the organic content (viz. fraction of polymer and cross-linker, relative to the silica) across the scaffolds during ice-templating, as evidenced by TGA data (Figure 6.4). Thus, TGA data reveals that the unusual perforated wall morphology observed in SEM is not a consequence of ACN-induced changes in polymer coating and/or cross-linking. Rather, it is a consequence of the influence of ACN on the freezing of the suspension and subsequent consolidation of the hybrid walls as the polymer cross-links around the silica particles.

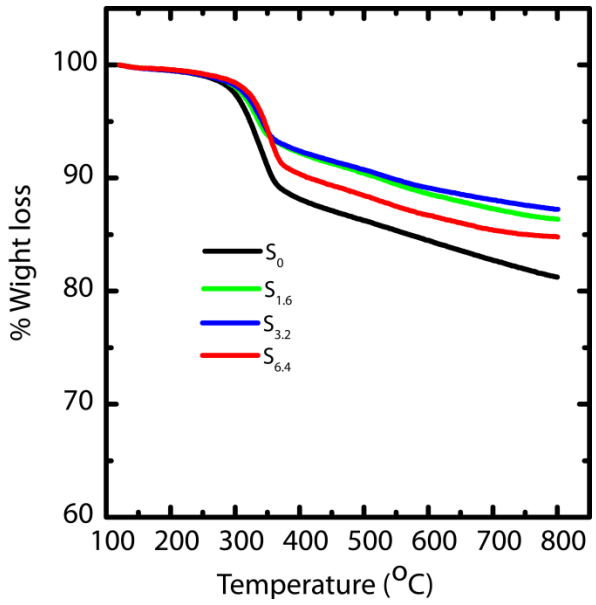

Figure 6.4: TGA of the scaffolds under N_2 atmosphere.

In chapter 5, we demonstrated that fluid transport through macroporous scaffolds during uptake of a wetting liquid is strongly dependent on the overall volume porosity of the scaffold. We estimate the porosity, as before, by taking a known volume of the scaffold and swelling it with water. Weighing the swollen scaffold yields the weight of the water absorbed (and therefore, the volume of the water can be calculated). The scaffold porosity is estimated as the volume of water absorbed normalized by the scaffold volume. We observe a small increase in the scaffold porosity from S_0 to the scaffolds prepared by ice-templating dispersions with water-ACN as solvent (Table 6.1). However, we observe no systematic variation in the porosity from $S_{1.6}$ to $S_{3.2}$ to $S_{6.4}$. We also subject water saturated scaffolds to compressive strain in a rheometer and measure the stress generated on imposition of strain. We observe that ice-templated scaffolds formed by freezing colloidal dispersions and cross-linking the polymer in the frozen state are elastic and recover completely from compressive strains as large as 85% (Figure 6.5). The stress-strain data from compression/expansion

measurements are similar for S_0, $S_{1.6}$, $S_{3.2}$ and $S_{6.4}$. All scaffolds show a slow initial linear increase in stress on compression, followed by a rapid increase at higher strain and exhibit hysteresis during expansion from the compressed state. We measure the modulus of the scaffolds as the slope of the linear stress-strain relationship, at low strains during the unloading cycle (Table 6.1). We observe that the compression modulus is not significantly affected by the presence of ACN in the ice-templated suspension and that ACN concentration has no systematic effect on E*.

Table 6.1: Porosity and compressive modulus of the scaffolds. The error bars for the modulus are obtained based on the fit to stress-strain data on one scaffold and do not represent sample-to-sample variations.

Scaffolds	% Porosity	E* (kPa)
S_0	85	26 ± 0.8
$S_{1.6}$	95	25 ± 0.6
$S_{3.2}$	91	27 ± 0.7
$S_{6.4}$	93	23 ± 0.6

6.4.2 Pressure drop study:

Capillary pressure measurements are performed in a home-built experimental setup. This setup is described in experimental section and is shown in Figure 6.6. We measure pressure drop across scaffolds when water is pumped through them at different flow rates viz. 0.2, 0.4, 0.6, 0.8 and 1.0 ml/min (Figure 6.7). At higher flow rates, the scaffolds debond from the walls of the glass capillary. Scaffolds are bonded to the glass tube through cross-linking between the PEI in the scaffold walls to that adsorbed on the walls of the glass tube. These bonds fail at the high stresses associated with flow rates in excess of 1 ml/min.

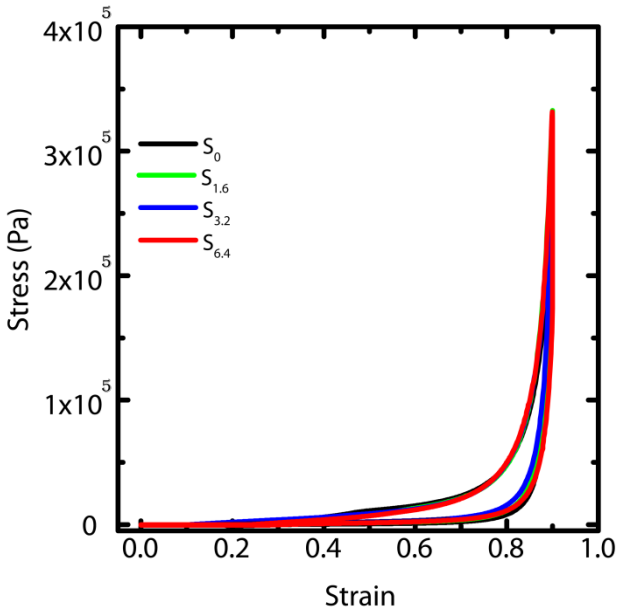

Figure 6.5: Compression and recovery of the scaffolds at 85 % strain at a rate of 3 mm min^{-1}.

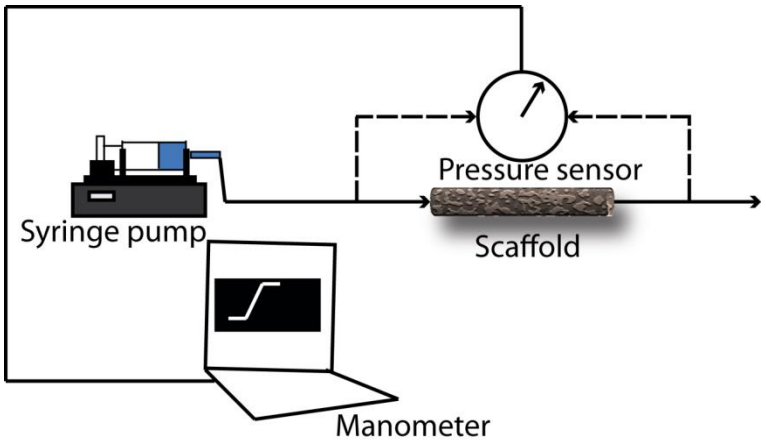

Figure 6.6: Schematic representation of a typical pressure drop measurement set up.

When flow is initiated by pumping water, we observe an initial build up of pressure after which flow proceeds at a steady state value of the pressure drop across the scaffold (Figure 6.7). Here we report the steady state pressure drop as a function of the flow rate. In all scaffolds, the steady state pressure drop increases monotonically with flow rate, as expected. We observe a remarkable decrease in the steady state pressure drop required to sustain a flow rate from S_0 to the scaffolds prepared using ACN (Figure 6.8). The decrease in pressure drop is already very significant from S_0 to $S_{1.6}$, and we observe a further drop in pressure drop for $S_{6.4}$ (Figure 6.8).

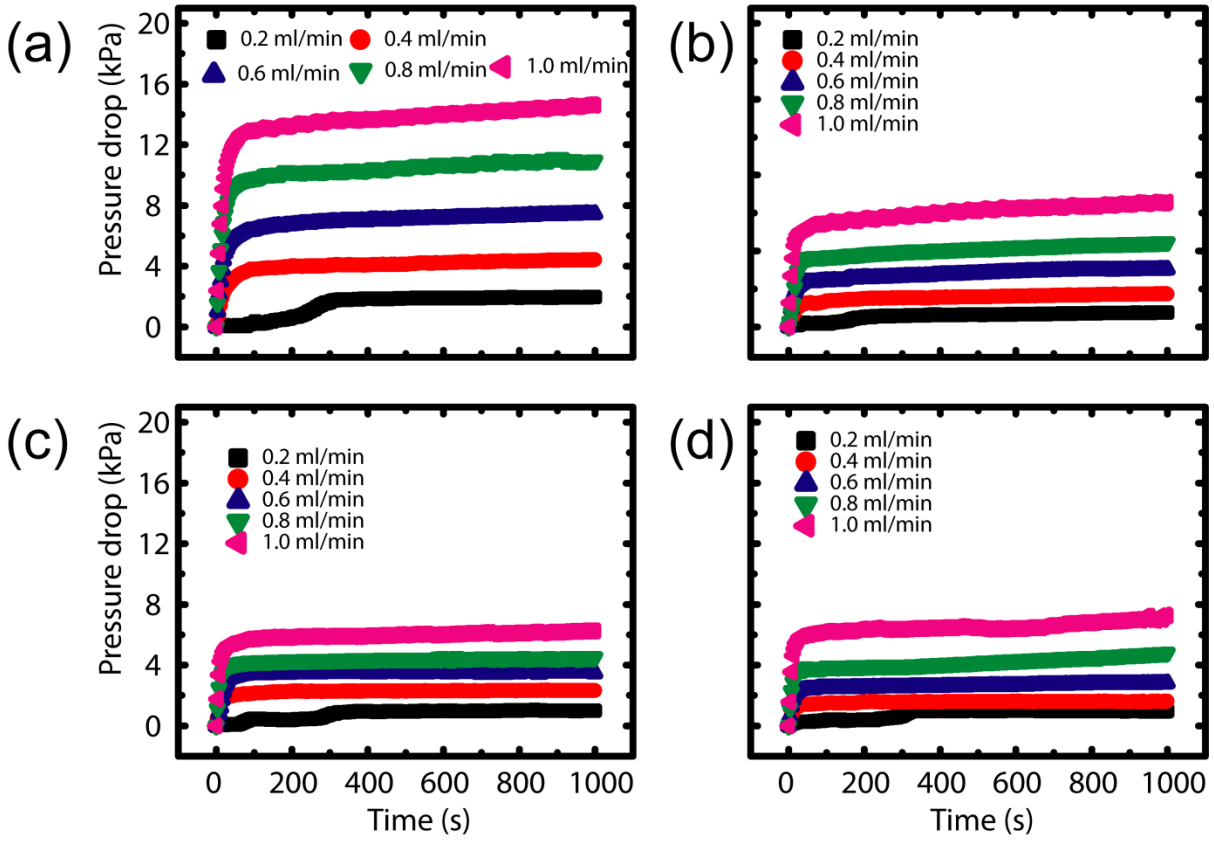

Figure 6.7: Pressure drop measurement at different flow rates with time (a) S_0; (b) $S_{1.6}$; (c) $S_{3.2}$; and (d) $S_{6.4}$.

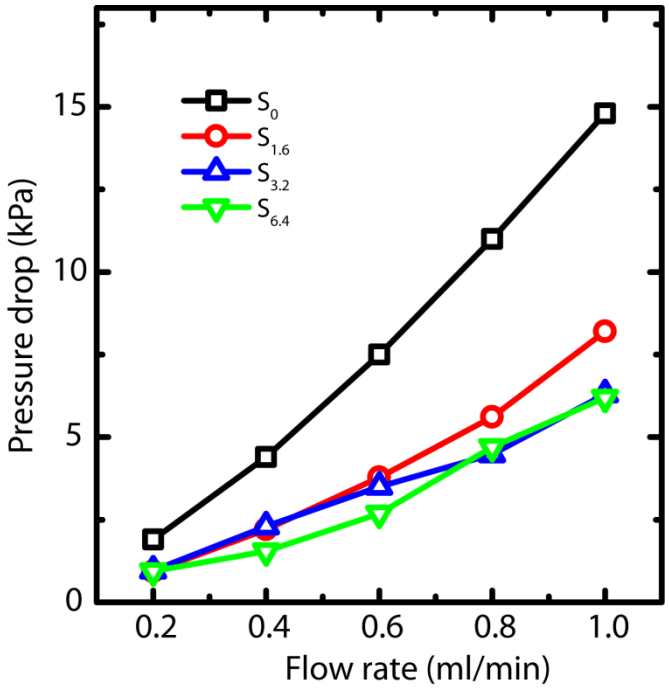

Figure 6.8: Pressure drop across the scaffold at different flow rates of water.

6.5 Conclusions

In this chapter, we have demonstrated for the first time, that holes can be introduced in the pore walls of ice-templated monoliths. Freezing of ice-templated dispersions contaning ACN introduces perforation in the pore walls. We demonstrate that perforation of the composite wall is significantly influenced by concentration. Remarkably, addition of the miscible organic solvent does not affect the overall porosity and mechanical response of the ice-templated monoliths. We observe a decrease in average pore size with increasing ACN content, and an increase in the fraction of the wall surface containing holes. We also demonstarte that perforated walls significantly reduce the pressure drop for flow of water through the monoliths. Thus, these monoliths with additional perforation in their pore walls are good candidates for low pressure drop mixing units.

6.6 References

(1) Ganai, A. K.; Kumari, S.; Sharma, K. P.; Panda, C.; Kumaraswamy, G.; Gupta, S. Sen. Synthesis of Functional Hybrid Silica Scaffolds with Controllable Hierarchical Porosity by Dynamic Templating. *Chem. Commun.* **2012**, *48*, 5292.

(2) Tan, Q.; Bao, X.; Song, T.; Fan, Y.; Shi, G.; Shen, B.; Liu, C.; Gao, X. Synthesis, Characterization, and Catalytic Properties of Hydrothermally Stable Macro–meso–micro-Porous Composite Materials Synthesized via in Situ Assembly of Preformed Zeolite Y Nanoclusters on Kaolin. *J. Catal.* **2007**, *251*, 69–79.

(3) Yuan, Z.-Y.; Su, B.-L. Insights into Hierarchically Meso–macroporous Structured Materials. *J. Mater. Chem.* **2006**, *16*, 663–677.

(4) Yu, J. G.; Su, Y. R.; Cheng, B. Template-Free Fabrication and Enhanced Photocatalytic Activity of Hierarchical Macro-/Mesoporous Titania. *Adv. Funct. Mater.* **2007**, *17*, 1984–1990.

(5) Rhodes, K; Davis, S; Caruso, F; Zhang, B; Mann, S. Hierarchical Assembly of Zeolite Nanoparticles into Ordered Macroporous Monoliths Using Core−Shell Building Blocks. **2000,** *12*, 2832–2834.

(6) Munch, E.; Saiz, E.; Tomsia, A. P.; Deville, S. Architectural Control of Freeze-Cast

Ceramics Through Additives and Templating. *J. Am. Ceram. Soc.* **2009**, *92*, 1534–1539.

(7) Fukushima, M.; Yoshizawa, Y. Fabrication of Highly Porous Nickel with Oriented Micrometer-Sized Cylindrical Pores by Gelation Freezing Method. *Mater. Lett.* **2015**, *153*, 99–101.

(8) Ouyang, A.; Wang, C.; Wu, S.; Shi, E.; Zhao, W.; Cao, A.; Wu, D. Highly Porous Core–Shell Structured Graphene-Chitosan Beads. *ACS Appl. Mater. Interfaces* **2015**, *7*, 14439–14445.

(9) Wang, J.; Gong, Q.; Zhuang, D.; Liang, J. Correction: Chemical Vapor Infiltration Tailored Hierarchical Porous CNTs/C Composite Spheres Fabricated by Freeze Casting and Their Adsorption Properties. *RSC Adv.* **2015**, *5*, 24749–24749.

(10) Ouyang, A.; Liang, J. Tailoring the Adsorption Rate of Porous Chitosan and Chitosan–carbon Nanotube Core–shell Beads. *RSC Adv.* **2014**, *4*, 25835–25842.

(11) Zhang, H.; Hussain, I.; Brust, M.; Butler, M. F.; Rannard, S. P.; Cooper, A. I. Aligned Two- and Three-Dimensional Structures by Directional Freezing of Polymers and Nanoparticles. *Nat. Mater.* **2005**, *4*, 787–793.

(12) Fukasawa, T.; Deng, Z.-Y.; Ando, M.; Ohji, T.; Kanzaki, S. Synthesis of Porous Silicon Nitride with Unidirectionally Aligned Channels Using Freeze-Drying Process. *J. Am. Ceram. Soc.* **2002**, *85*, 2151–2155.

(13) Fukasawa, T.; Ando, M.; Ohji, T.; Kanzaki, S. Synthesis of Porous Ceramics with Complex Pore Structure by Freeze-Dry Processing. *J. Am. Ceram. Soc.* **2001**, *84*, 230–232.

(14) Mukai, S. R.; Nishihara, H.; Tamon, H. Formation of Monolithic Silica Gel Microhoneycombs (SMHs) Using Pseudosteady State Growth of Microstructural Ice Crystals. *Chem. Commun.* **2004**, *0* , 874.

(15) Deville, S. Freeze-Casting of Porous Ceramics: A Review of Current Achievements and Issues. *Adv. Eng. Mater.* **2008**, *10*, 155–169.

(16) Kim, J.-W.; Tazumi, K.; Okaji, R.; Ohshima, M. Honeycomb Monolith-Structured Silica with Highly Ordered, Three-Dimensionally Interconnected Macroporous Walls. *Chem. Mater.* **2009**, *21*, 3476–3478.

(17) Zhang, H.; D'Angelo Nunes, P.; Wilhelm, M.; Rezwan, K. Hierarchically Ordered Micro/meso/macroporous Polymer-Derived Ceramic Monoliths Fabricated by Freeze-Casting. *J. Eur. Ceram. Soc.* **2016**, *36*, 51–58.

(18) Rajamanickam, R.; Kumari, S.; Kumar, D.; Ghosh, S.; Kim, J. C.; Tae, G.; Sen Gupta,

S.; Kumaraswamy, G. Soft Colloidal Scaffolds Capable of Elastic Recovery after Large Compressive Strains. *Chem. Mater.* **2014**, *26*, 5161–5168.

(19) Gu, T.; Gu, Y.; Zheng, Y.; Wiehl, P. E.; Kopchick, J. J. Phase Separation of Acetonitrile-Water Mixture in Protein Purification. *Sep. Technol.* **1994**, *4*, 258–260.

(20) Cunningham, G. P.; Vidulich, G. A.; Kay, R. L. Several Properties of Acetonitrile-Water, Acetonitrile-Methanol, and Ethylene Carbonate-Water Systems. *J. Chem. Eng. Data* **1967**, *12*, 336–337.

(21) Gu, Y.; Shih, P.-H. Salt-Induced Phase Separation Can Effectively Remove the Acetonitrile from the Protein Sample after the Preparative RP-HPLC. *Enzyme Microb. Technol.* **2004**, *35*, 592–597.

(22) Oence, D. N.; Gu, T. Liquid-Liquid Equilibrium of the Acetonitrile-Water System for Protein Purification. *Sep. Technol.* **1996**, *6*, 261–264.

(23) Zarzycki, P. K.; Wlodarczyk, E.; Lou, D.-W.; Jinno, K. Evaluation of Methanol-Water and Acetonitrile-Water Binary Mixtures as Eluents for Temperature-Dependent Inclusion Chromatography. *Anal. Sci.* **2006**, *22*, 453–456.

(24) Arsiccio, A.; Barresi, A. A.; Pisano, R. Prediction of Ice Crystal Size Distribution after Freezing of Pharmaceutical Solutions. *Cryst. Growth Des.* **2017**, *17*, 4573–4581.

Summary

This thesis is focused on the applications of macroporous sponges prepared via ice-templating. We prepare ice-templated hybrid scaffolds by freezing an aqueous dispersion of inorganic colloids, cross-linkable polymer (polyethyleneimine, PEI) and diepoxy cross-linker, and by allowing the polymer to cross-link around the inorganic colloids, in the frozen state. This protocol results in foams that are elastic, swellable and that can recover their shape after compression, despite being comprised largely of inorganic particles (in some cases, >85% by weight). Flexible particle-based sponges represent platform materials that have potential for a wide variety of applications., We also demonstrate 100-fold scale up of foam synthesis, by shaking the dispersion during the freezing process to ensure uniform heat transfer. There is no compromise in mechanical properties and fire retardant characteristics of the scaled-up sponges. We demonstrate the use of these sponges as fire retardant memory foams, as flexible supercapacitors and as omniphilic absorbents. We examine the kinetics of capillarity driven solvent uptake in macroporous scaffolds. Finally, we describe a modified synthetic protocol that allows us to prepare macroporous monoliths with holes in the pore walls. Such monoliths present significantly lower pressure drop for flow of liquid pumped through them.

Hybrid scaffolds exhibit exceptional fire retardant properties since they are predominantly comprised of inorganic. These hybrid foams are synthesized from environmentally benign constituents and do not contain any fire retardant additive. We demonstrated that when hybrid scaffolds are subjected to a torch burn test, the flame does not spread and is self-extinguished. The foam structure does not collapse due to the underlying inorganic framework. We believe that such remarkable fire retardant property of the hybrid foam could have implications for foam applications in furniture, upholstery and automotive, airline or auditorium seating applications.

We also prepare pure polymer sponge by ice templating solutions of poly(ethylene imine) and diepoxide and by crosslinking the polymer in the frozen state. The crosslinked polymer sponges are electrically insulating. We prepare porous polymer sponges containing polyphenols from green tea, and use these to reduce silver salts that form silver nanoparticles, embedded in the monolith walls. We impart electrical conductivity to polymer scaffolds by electroless deposition of gold, promoted by the silver nanoparticle seeds. The sponge retains its mechanical performance after large number of cycles of loading and unloading, even after deposition of metal. PEDOT coated sponge exhibits moderate capacitance that is retained after several cycles of charge discharge. We prepare capacitors using both liquid and gel

electrolytes and observe that in both cases, the capacitance is intact after compressing the device. Therefore this robust device could be useful as an energy source for flexible electronics.

Omniphilic ice-templated sponges can be used to absorb solvents independent of their polarity. Functionalization of the sponge walls of ice-templated crosslinked polymer sponges with alkyl chains of variable chain length from C4 to C17 affords materials with controllable affinity for polar or apolar solvents. Modification with a C4 chain results in a material that can absorb 12 times its weight of either water or hexane. Such an omniphilic sponge is unprecedented. Chemical modification with a C17 chain results in a sponge that can absorb 15 times its weight in hexane. Remarkably, the dry C17 sponge retains its oleophilicity underwater. Even a water-saturated C17-modified sponge is able to absorb hexane from a hexane-water mixture. Such sponges are also capable of separating hexane from surfactant stabilized emulsions. These sponges are elastic. Therefore, absorbed solvent can simply be extracted by compressing the sponge, and the sponge can be reused subsequently.

We also demonstrate kinetics of water uptake in a series of sponges with a wide variation in properties (porosity varying from 66 to 98%; modulus varying by over an order of magnitude and wall composition varying from pure polymeric to polymer-inorganic composite). We showed a remarkable universality in capillary uptake in porous sponges, over the entire range of sponge porosity and deformability. The kinetics of water uptake for all these sponges could be collapsed onto a universal curve. Interestingly, we observed that capillary rise is not influenced by the elasticity of the sponge. We adapted the Ergun/Forchheimer model, that are traditionally used to describe flow through rigid porous materials, and demonstrate that these describe capillary driven flow in these elastic scaffolds as well.

We also demonstrated the preparation of composite scaffolds that exhibit perforations in their walls. We demonstrated that ice-templating dispersions from water/acetonitrile mixtures result in macroporous monoliths with walls containing holes. The monolith morphology, viz. pore size and hole formation could be controlled by simply varying the acetonitrile concentration. Scaffolds with perforated walls present reduced pressure drops for flow of water through them, in comparison to those with solid walls.

List of Research Credential, Awards and Conferences

Publications and Patent:

1. **S. Chatterjee**, S. Sen Gupta, and G. Kumaraswamy, "Omniphilic Polymeric Sponges by Ice Templating", ***Chem. Mater.,*** vol. 28, pp 2823-1831, 2016.

2. C. Das**,** [#] **S. Chatterjee**, [#] G. Kumaraswamy, and K. Krishnamoorthy "Elastic Compressible Energy Storage Devices from Ice Templated Polymer Gels treated with Polyphenols", ***J. Phys. Chem. C*** , vol. 121, pp. 3270-3278, 2017.
   [#] Equal contribution
3. **S. Chatterjee**, P. Doshi, and G. Kumaraswamy, "Capillary uptake in macroporous compressible sponges", **Soft Matter,** vol. 13, pp 5731-5740, 2017.

4. **S. Chatterjee**, *K.* Shanmuganathan and G. Kumaraswamy, "Fire-Retardant, Self-Extinguishing Inorganic/Polymer Composite Memory Foams" **ACS Appl. Mater. Interfaces,** vol. 9, pp 44864-44872, 2017.

5. **S. Chatterjee**, A. Potdar, S. Kuhn and G. Kumaraswamy, *"Preparation of Macroporous Scaffolds with Holes in Pore Walls and Pressure Driven Flows through them" (Manuscript Submitted in RSC Advances)*

6. G. Kumaraswamy, S. Sen Gupta, and **S. Chattrejee**, "Omniphilic Sponge", **Patent IN** 3830/DEL/2015; **(US)**14/953811.

Awards:

1. "**Best oral presentation award**" (JNCASR-Bangalore, 2014).

2. "**Best poster award in NCL science day"** (February, 2015).

3. **Awarded Junior Research Fellowship(JRF)** by University Grant Commission (UGC).

Conferences:

1. Attended "SERC school on Rheology of Complex fluids: Advanced computational Methods & Symposium on Rheology of Complex Fluids-2012", organised by IIT Guwahati, January 2012.

2. Poster Presentation in "Complex Fluids-2014", organised by JNCASR-Bangalore, 2014.

3. Poster presentation in "International Complex Fluids Conference-CompFlu-2016", organised by IISER Pune, January 2016.

4. Poster presentation in "Complex Fluids- CompFlu-2016" organised by IIIT Hyderabad, December 2016.